THE UNIVERSITY OF CHICAGO

GLIMPSES OF FAR AWAY PLACES: INTENSIVE ATMOSPHERE CHARACTERIZATION OF EXTRASOLAR PLANETS

A DISSERTATION SUBMITTED TO
THE FACULTY OF THE DIVISION OF THE PHYSICAL SCIENCES
IN CANDIDACY FOR THE DEGREE OF
DOCTOR OF PHILOSOPHY

DEPARTMENT OF ASTRONOMY AND ASTROPHYSICS

BY

LAURA KREIDBERG

CHICAGO, ILLINOIS

AUGUST 2016

Far away places with strange sounding names

Far away over the sea

Those far away places with strange sounding names

Are calling, calling me.

– Joan Whitney & Alex Kramer

TABLE OF CONTENTS

LIST OF FIGURES

LIST OF TABLES

ACKNOWLEDGMENTS

It is with great pleasure that I thank the many people who contributed to the writing of this thesis. You believed in me, laughed with me (and at me), dinner partied, danced, sang, and made merry with me, and I never could have done it without you. Here are a few parting words.

First to Jacob: you told me once that there are many opportunities in the field of exoplanets, and so there are. Thank you for helping me find them. Thanks also to the entire Bean group: Andreas, Kevin, Megan, Hannah, Lily, Julian, Diana, and Adam. You have been supportive in too many ways to count, from cookies to advice about color palettes, debugging my code, celebrating, commiserating, talking through ideas, and even putting up with my loud typing.

To the astronomy department as a whole: thanks for letting in some exoplanet folks. Cosmology is okay, but we all know planets are the future (no, really!). Rocky and Don, your patience was astounding when I marched in as a first year student with a lot of opinions. Thank you for listening. Wendy – my science mom! You inspire me to do big things. May your MCMCs always converge and your Python code be free of bugs. I hope I'll have another student like you someday.

To the breakfast cabal: thank you for continuously reminding me why I love what I do. I never imagined that I would willingly get out of bed to make it downtown by 7:30 on Friday mornings, but you made it worth it every time. When I finally find some aliens I'll come back to breakfast so we can figure out what it all means.

Thanks to the Chicago tango community for helping me find my balance, and to Golosa for crunchy dissonance and endless folk wisdom.

To Karl and Huston: I can't even begin to express my gratitude for all that you have done, so I will simply say thanks for making Chicago home.

Finally, to my family: I am ever grateful for your over-the-top support. I love you all.

ABSTRACT

Exoplanet atmosphere characterization has the potential to reveal the origins, nature, and even habitability of distant worlds. This thesis represents a step towards realizing that potential for a diverse group of four extrasolar planets. Here, I present the results of intensive observational campaigns with the Hubble and Spitzer Space Telescopes to study the atmospheres of the super-Earth GJ 1214b and the hot Jupiters WASP-43b, WASP-12b, and WASP-103b.

I measured an unprecedentedly precise near-infrared transmission spectrum for GJ 1214b that definitively reveals the presence of clouds in the planets atmosphere. For WASP-43b and WASP-12b, I also measured very precise spectra that exhibit water features at high confidence ($> 7\,\sigma$). The retrieved water abundance for WASP-43b extends the well-known Solar System trend of decreasing atmospheric metallicity with increasing planet mass. The detection of water for WASP-12b marks the first spectroscopic identification of a molecule in the planet's atmosphere and implies that it has solar composition, ruling out carbon-to-oxygen ratios greater than unity. For WASP-103b, I present preliminary results from the new technique of phase-resolved spectroscopy to determine the planet's temperature structure, dynamics, and energy budget. In addition to these observations, I also describe the BATMAN code, an open-source Python package for fast and flexible modeling of transit light curves.

Taken together, these results provide a foundation for comparative planetology beyond the Solar System and the investigation of Earth-like, potentially habitable planets with future observing facilities.

CHAPTER 1

INTRODUCTION

1.1 Exoplanets' Greatest Hits, 1995 - present

Exoplanet science has made stunning progress during the twenty short years since the first planet orbiting a star other than the Sun was discovered (Mayor & Queloz, 1995). To name just a few recent highlights, we now have mass measurements for terrestrial planets (e.g., Howard et al., 2013; Pepe et al., 2013; Dressing et al., 2015), direct images of a young Jupiter-like planet within 15 AU of its host star (Macintosh et al., 2015), and the discovery of over 2000 confirmed transiting planets from NASA's *Kepler* mission (Borucki et al., 2010) and ground-based surveys (from the Exoplanet Orbit Database; Han et al., 2014).

Exoplanets are far more diverse in their properties than the planets of the Solar System. We have found ultra-short period planets (e.g., Sanchis-Ojeda et al., 2014), highly inflated planets (e.g., Hebb et al., 2009), a new class of planet known as super-Earths, which are between the Earth and Neptune in size (e.g., Santos et al., 2004), circumbinary planets (e.g., Doyle et al., 2011), and even a disintegrating planet orbiting a white dwarf (Vanderburg et al., 2015).

But this wealth of discovery is perhaps best summarized with demographic information. We know now that planets are common, with at least 20% of stars hosting one or more (Howard et al., 2012; Fressin et al., 2013; Dressing & Charbonneau, 2015). Note that this occurrence rate is a lower bound because it does not include long-period planets ($P > 1$ year), and will likely increase with longer survey duration. Small planets are more abundant than large ones, with a plateau in occurrence near $2\,R_\oplus$ (Petigura et al., 2013). Remarkably, occurrence measurements have even extended to Earth analogs (terrestrial planets in the habitable zones of their host stars), with the best current estimate of their abundance at roughly 10% (Petigura et al., 2013; Dressing & Charbonneau, 2015).

1.2 Moving from Discovery to Characterization

There are two questions that immediately arise for these new-found exoplanets:

1. How did they form and evolve?

2. What are they like?

One approach to answering these questions is to compare the observed planet masses, radii, and orbital architectures to theoretical models of planet formation and interior structure. There has been extensive work on this topic, but it is a challenging proposition because there are often multiple models that can reproduce the properties of a planetary system (e.g., Rogers & Seager, 2010a; Chiang & Laughlin, 2013; Hansen & Murray, 2013; Dawson, 2014; Dawson et al., 2016; Chatterjee & Tan, 2014; Schlichting, 2014; Batygin et al., 2015; Lee & Chiang, 2016). Morever, none of this work can address a planet's climate or habitability.

Fortunately, we can reveal the nature of exoplanets in much greater detail by characterizing their atmospheres. The atmosphere is a fossil record of formation conditions, and it is also responsible for regulating planetary climate.

1.2.1 Clues from Planetary Atmospheres I: How Do Planets Form?

To give a conceptual example of how atmospheres are sensitive to planet formation conditions, consider the case of atmospheric water abundance. For a typical protoplanetary disk around a Sun-like star, water ice freezes out a radial distance of 2 AU (Öberg et al., 2011). Water is the dominant carrier of oxygen, so beyond the water frost-line the remaining gas is oxygen-poor whereas solids are oxygen-rich.

Consequently, giant planets that form by core accretion beyond the water frost-line are expected to sweep up the majority of their mass in oxygen-poor gas and have low water abundances (Madhusudhan et al., 2011a). Small planets, on the other hand, have a larger bulk fraction of their mass coming from planetesimals. Super-Earths formed exterior to

the water frost-line will therefore be enriched in water compared to those formed at shorter orbital distances from the star (Chiang & Laughlin, 2013).

This qualitive model of water enrichment/depletion has been made quantitative by planet population synthesis models that track the planets' composition in detail (Fortney et al., 2013; Madhusudhan et al., 2014a; Marboeuf et al., 2014). These simulations show how composition is sensitive not only to formation location, but also the size and composition of planetesimals, the surface density of solids in the protoplanetary disk, and the total mass of the disk.

By measuring the atmospheric composition of a large sample of exoplanets and comparing the results to the output of planet population synthesis models, we have the potential to constrain these important facets of the formation process.

1.2.2 Clues from Planetary Atmospheres II: What are Planets Like?

Planetary atmospheres are also responsible for planetary climate in two key ways. First, the atmosphere sets a planet's energy budget. The atmospheric chemical composition (including cloud and haze properties) controls the fraction of incident stellar flux reflected by the planet (the Bond albedo). In addition, greenhouse gases such as water and carbon dioxide absorb outgoing long-wave radiation from the planet's surface and heat the atmosphere. Some of this energy is re-radiated toward the surface, heating it in a feedback loop that increases the equilibrium temperature of the planet. The other major role of the atmosphere is energy transport. Atmospheric dynamics tend to even out temperature differences on the planet caused by variations in insolation (from equator to pole, or day- to nightside). This energy circulation from hot to cold regions is particularly important for tidally locked planets, which have a highly irradiated dayside and no incident flux on the nightside (Pierrehumbert, 2010).

The atmosphere is also essential for planetary habitability. Consider the example of the inner planets of the Solar System: Venus, Earth, and Mars. All three are near the so-called habitable zone, where surface temperatures could be appropriate for liquid water (Koppa-

rapu, 2013). However, only Earth has retained its water. Venus lost most of its water through evaporation caused by a runaway greenhouse effect and subsequent photoevaporation, leaving a remnant atmosphere composed mainly of CO_2. This composition results in an uninhabitable surface with a temperature above 700 K, despite the planet's relatively modest insolation. By contrast, Mars has almost no atmosphere. Due to its low mass (only one tenth that of Earth), Mars is vulnerable to atmospheric escape. It may have also experienced atmospheric erosion due to large impacts early in its history (Pierrehumbert, 2010). The end result is a low-pressure CO_2 atmosphere and a surface that is cold, dessicated, and unfit for life.

1.2.3 Goals for This Work

The goal of my thesis is detailed characterization of the atmospheres of a select group of exoplanets. This work is designed to make the first steps in understanding their origins and climates, based on the principles discussed in this section. More broadly, a second goal is to push the limits of achievable precision with current facilities to prepare for even more precise investigations with the *James Webb Space Telescope* (*JWST*), and lay the foundation for the eventual study of potentially habitable worlds to separate the Earths from the Marses and the Venuses.

1.3 Overview of Atmosphere Characterization Techniques

As described in §,1.2, atmosphere characterization has the potential to yield great insight into the nature and origins of extrasolar planets. However, these planets are small, faint, and distant, so how can one go about studying their atmospheres?

The focus of this work is on transiting planets, which periodically pass in front of their host stars along our line of sight. These systems provide an unmatched opportunity for atmosphere characterization because it is possible to tease out the spectrum of the planet by

making differential measurements with respect to the host star. Using the star as a reference point skirts the challenge of blocking out its light, and enables the study of cool planets with short orbital periods (which are currently inaccessible via direct imaging). Transiting systems therefore offer the best near-future prospects for characterizing planets similar to those in our Solar System. In this section, I summarize the two primary techniques for atmosphere characterization of transiting planets: transmission spectroscopy and thermal emission spectroscopy.

1.3.1 Transmission Spectroscopy

The transmission spectroscopy method, illustrated in Figure 1.1, measures the planet's transit depth as a function of wavelength. During transit, a small fraction of the stellar flux filters through the planetary atmosphere along our line of sight. Absorbing species in the atmosphere (molecules, atoms) block the transmission of stellar flux, resulting in an increase in transit depth at wavelengths with larger opacity. The change in transit depth with wavelength due to this effect scales as:

$$\Delta \sim 2HR_p/R_s^2 \tag{1.1}$$

where R_p is the planet radius, R_s is the stellar radius, and $H = kT/\mu g$ is the atmospheric scale height (Seager, 2010). The atmospheric mean molecular mass and planetary surface gravity are denoted by μ and g. Measurements of the transmission spectrum are primarily sensitive to the atmospheric composition (relative molecular abundances) and the presence of clouds and haze.

1.3.2 Emission Spectroscopy

A complementary approach to studying the atmospheres of transiting planets is the emission spectroscopy technique, which measures the thermal emission from the planet. Figure 1.2

Figure 1.1: Transmission Spectroscopy Schematic

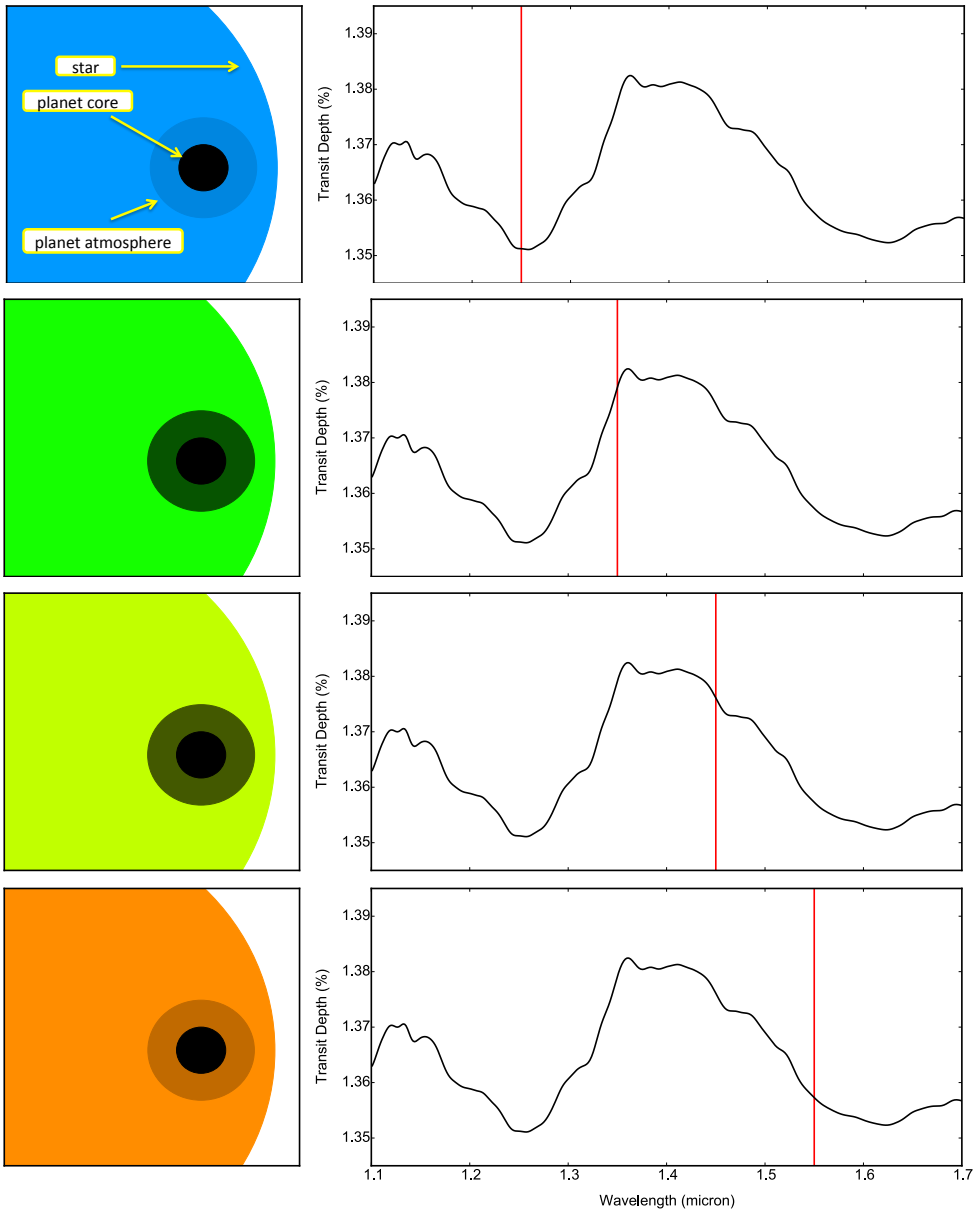

Illustration of the geometry of transmission spectroscopy. The left panels show a cartoon star (large colored circle), with a transiting planet (core indicated by the black circle; atmosphere by the partially opaque annulus). The rendered opacity of the atmosphere is proportional to the fraction of transmitted stellar flux. The right-hand panels show the predicted transmission spectrum for a 100% water vapor model atmosphere for a planet like GJ 1214b; the transit depth increases at wavelengths where a larger fraction of stellar flux is absorbed by water molecules in the atmosphere. The vertical red line indicates the wavelength of light chosen to compute the atmospheric opacity (1.25, 1.35, 1.45, and 1.55 μm from top to bottom).

illustrates this approach. The eclipse depth is the ratio of planet to stellar flux, and is given by:

$$f_p = \frac{R_p^2 I(\lambda, T_p)}{R_s^2 I(\lambda, T_s)} \tag{1.2}$$

where $I(\lambda, T)$ is the blackbody intensity at a wavelength λ and temperature T. The emission spectrum is sensitive to both the planet's atmospheric composition and its thermal structure. At wavelengths where the atmosphere has higher opacity, thermal emission measurements probe higher layers of the planetary atmosphere and thus constrain changes in temperature with altitude.

Emission spectroscopy can also be used to characterize the atmosphere as a function of longitude. A short-period, tidally-locked planet completes a full revolution on its spin axis every orbital period. Phase curve observations, which measure thermal emission as a function of time over an entire revolution, can therefore determine *global* atmospheric composition and temperature structure.

1.4 Technical Breakthroughs Enabling Atmospheric Studies

It is worth noting the technical challenges associated with making the measurements described in the previous section. For the best-case scenario, a large, high-temperature planet (Jupiter radius, equilibrium temperature $> 1000\,K$), the amplitude of features in transmission and emission spectra is of order 100 parts per million. This level of precision is challenging to achieve with ground-based observations due to turbulence in the Earth's atmosphere (e.g., Bean et al., 2010). Even from space with photon-noise limited precision, stacking multiple transit and eclipse observations is necessary to reach sub-100 ppm precision (e.g., Kreidberg et al., 2014b).

There have been two major breakthroughs that enable measurements precise enough to reveal spectral features in exoplanet atmospheres. The first is the development of the spatial

Figure 1.2: Thermal Emission Schematic

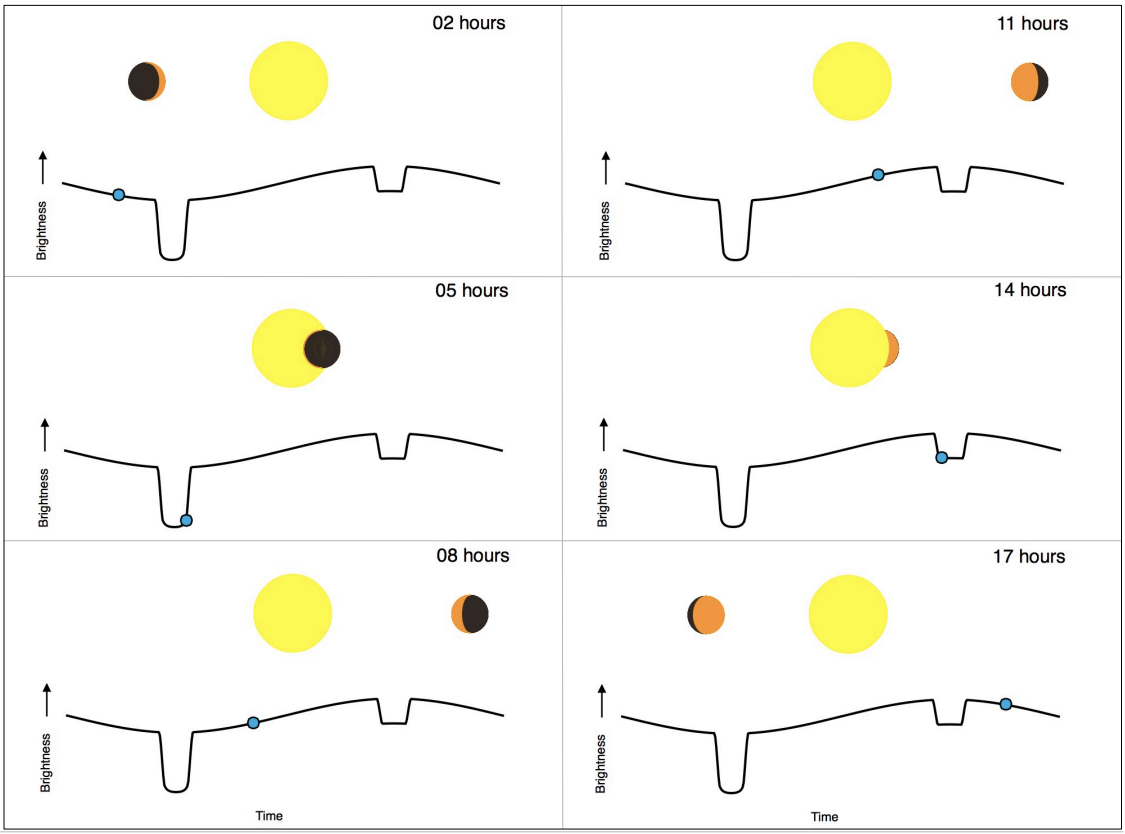

Time lapse cartoon illustrating planet thermal emission as a function of time over its 20-hour orbital period. The star is shown with a yellow circle. The planet is depicted as a disk with orange shading indicating the hot dayside and gray shading for the nightside, with the planet-to-star radius ratio enlarged for display purposes. The black line shows the total planet + star flux as a function of time, with the blue circle marking the time corresponding to each panel. This cartoon neglects reflected light from the planet, which can contribute significant flux at visible wavelengths.

scanning technique for the Wide Field Camera 3 instrument on the *Hubble Space Telescope* (*HST*/WFC3). WFC3 is the newest instrument available on *HST* (installed in 2009) and it provides low-resolution ($R \sim 100$) near-infrared spectroscopy between 0.8 and 1.7 μm. Since 2012, the Space Telescope Science Institute has supported an observing mode called "spatial scanning", which slews the telescope over the course of an exposure to spread out the spectrum in the spatial direction on the detector. This instrument mode is a crucial advance because it enables longer exposures without saturating the detector, improving the duty cycle for observations of bright targets by an order of magnitude. Spatial scanning also diminishes instrument systematic noise caused by variation in sensitivity of individual pixels on the detectors, because a scanned spectrum is spread over $10 - 100\times$ more pixels than a traditional staring mode spectrum. WFC3 has been used extensively by the atmosphere characterization community and has consistently provided repeatable, photon-noise-limited measurements of planet spectra (e.g. Deming et al., 2013; Kreidberg et al., 2014b; Knutson et al., 2014a; Stevenson et al., 2014a; Wakeford et al., 2016).

The second breakthrough for atmosphere characterization has been the discovery of many transiting planets orbiting bright stars. WFC3 observations are photon-noise limited, so bright targets are essential for successful measurements with a reasonable amount of observing time. While NASA's space-based *Kepler* mission takes the lead in the total number of transiting planet detections, the best candidates for atmosphere characterization come from ground-based surveys that are focused specifically on bright stars. These include the WASP, HAT, KELT, MEarth, and TRAPPIST surveys (Pollacco et al., 2006; Bakos et al., 2007; Pepper et al., 2007; Charbonneau et al., 2009; Gillon et al., 2016). According to the Exoplanet Orbit Database (Han et al., 2014), over one hundred planets have been found to transit stars with H magnitude less than 10 . Noteable among these discoveries are planets transiting the smallest stars (M-dwarfs), which are favorable targets for atmosphere studies due to their large transit depths.

1.5 Chapter Summaries

Thanks to the technical advances described in the previous section, high precision atmosphere characterization is now possible for transiting planets. In the remainder of this document, I describe my work on intensive atmosphere characterization for a selection of exoplanet archetypes.

Chapter 2 reports the measurement of a precise near-infrared transmission spectrum for the super-Earth GJ 1214b. This planet lies directly between the Earth and Neptune in size ($R = 2.7\,R_\oplus$, $M = 6.5\,M_\oplus$), so its composition cannot be deduced from mass and radius measurements alone due to degeneracies between the core mass fraction and the atmosphere. I made the first measurement of its spectrum that is precise enough to detect features for cloud-free, high mean molecular weight compositions. However, the despite the unprecedented precision of this measurement, the spectrum is flat – devoid of spectral features. The best explanation for this result is that clouds or haze are present in the atmosphere, blocking transmission of stellar flux up to high altitudes. This chapter is adapted from Kreidberg et al. (2014b).

In **Chapter 3**, I investigate the atmospheric water abundance for the hot Jupiter WASP-43b. In contrast to the Solar System gas giants, this planet is hot enough that water is in the gas phase in its atmosphere, enabling a robust estimate of its abundance. I measured precise transmisssion and emission spectra for WASP-43b and detected water absorption features at high confidence in both. I used these data to retrieve the atmospheric properties and find a water abundance that is consistent with expectations for a solar composition gas ($0.4 - 3.5\times$ solar at $1\,\sigma$ confidence). This measurement agrees with the Solar System trend of decreasing atmospheric metallicity with increasing planet mass. It also illustrates the potential exoplanets hold for precise composition measurements: such measurements can be made for a much larger and more diverse sample of planets than the Solar System provides, to put new constraints on theories of planet formation. This chapter is based on Kreidberg et al. (2014a).

Chapter 4 describes the measurement of the atmospheric composition of a second hot Jupiter, WASP-12b. This planet has been held up as the canonical example of a carbon-rich planetary atmosphere, implying an unusual formation history for the planet (Madhusudhan et al., 2011c,a; Stevenson et al., 2014b). I measured a near-infrared transmission spectrum for the planet that exhibits a strong water absorption feature. This is the first unambiguous identification of a molecular absorber in the planet's atmosphere. Suprisingly, the measurement is inconsistent with the carbon-rich hypothesis: water is expected to be depleted in carbon-rich chemistry, because all the oxygen atoms are bound up in CO and CO_2. Further work is needed to reconcile the measured water abundance with previous analyses of the atmospheric composition. This chapter is adapted from Kreidberg et al. (2015).

Chapter 5 presents the `batman` code, an open-source Python package for modeling exoplanet transit light curves. The package implements a new integration algorithm I developed to calculate the light curves for any radially symmetric stellar limb darkening law. This chapter, based on Kreidberg (2015), describes the new algorithm and investigates the performance of the code.

In **Chapter 5**, I discuss preliminary results from a spectroscopic phase curve observation of the hot Jupiter WASP-103b. This result combines the new technique of phase-resolved *HST*/WFC3 spectroscopy and traditional *Spitzer* photometry to the planet's thermal emission over its entire orbital period. Compared to WASP-43b (the first planet studied with this approach, Stevenson et al., 2014d), WASP-103b has similar rotation rate and surface gravity, but a much higher equilibrium temperature, making it an excellent target for comparative planetology. The preliminary results show a qualitatively different thermal structure for WASP-103b: the spectra are consistent with expectations for a blackbody, most likely indicating that the dayside temperature pressure profile is isothermal.

Chapter 6 concludes.

CHAPTER 2

CLOUDS IN THE ATMOSPHERE OF THE SUPER-EARTH EXOPLANET GJ 1214b

2.1 Introduction

Recent surveys have revealed that planets intermediate in size between Earth and Neptune ("super-Earths") are among the most common planets in the Galaxy (Cassan et al., 2012; Fressin et al., 2013; Petigura et al., 2013). Atmospheric studies are the next step toward developing a comprehensive understanding of this new class of object (Adams et al., 2008; Miller-Ricci et al., 2009a; Rogers & Seager, 2010b). Much effort has been focused on using transmission spectroscopy to characterize the atmosphere of the super-Earth archetype GJ 1214b (Bean et al., 2010; Désert et al., 2011; Bean et al., 2011; Berta et al., 2012; Fraine et al., 2013; Miller-Ricci & Fortney, 2010; Nettelmann et al., 2011; Miller-Ricci Kempton et al., 2012; Howe & Burrows, 2012; Morley et al., 2013; Benneke & Seager, 2013), but previous observations did not have sufficient precision to distinguish between two interpretations for the atmosphere. The planet's atmosphere could be dominated by relatively heavy molecules, such as water (e.g., a 100% water vapor composition), or it could contain high-altitude clouds that obscure its lower layers. Here we report a measurement of the transmission spectrum of GJ 1214b at near-infrared wavelengths that definitively resolves this ambiguity. These data, obtained with the Hubble Space Telescope, are sufficiently precise to detect absorption features from a high mean molecular mass atmosphere. The observed spectrum, however, is featureless. We rule out cloud-free atmospheric models with water-, methane-, carbon monoxide-, nitrogen-, or carbon dioxide-dominated compositions at greater than $5\,\sigma$ confidence. The planet's atmosphere must contain clouds to be consistent with the data.

2.2 Observations and Data Reduction

We observed 15 transits of the planet GJ 1214b with the Wide Field Camera 3 (WFC3) instrument on the Hubble Space Telescope (HST) between UT 27 September 2012 and 22 August 2013. Each transit observation consisted of four orbits of the telescope, with 45-minute gaps in phase coverage between target visibility periods due to Earth occultation. We obtained time-series spectroscopy from 1.1 to 1.7 μm during each observation. The data were taken in spatial scan mode, which slews the telescope during the exposure and moves the spectrum perpendicular to the dispersion direction on the detector. This mode reduces the instrumental overhead time by a factor of five compared to staring mode observations. We achieved an integration efficiency of 60 – 70%. We extracted the spectra and divided each exposure into five-pixel-wide bins, obtaining spectro-photometric time series in 22 channels (resolution $R \equiv \lambda/\Delta\lambda \sim 70$). The typical signal-to-noise per 88.4 s exposure per channel was 1,400. We also created a "white" light curve summed over the entire wavelength range. Our analysis incorporates data from 12 of the 15 transits observed, because one observation was compromised due to a telescope guiding error and two showed evidence of a starspot crossing.

The raw transit light curves for GJ 1214b exhibit ramp-like systematics comparable to those seen in previous WFC3 data (Berta et al., 2012; Deming et al., 2013; Swain et al., 2013). The ramp in the first orbit of each visit consistently has the largest amplitude and a different shape from ramps in the subsequent orbits. Following standard procedure for HST transit light curves, we did not include data from the first orbit in our analysis, leaving 654 exposures. We corrected for systematics in the remaining three orbits using two techniques that have been successfully applied in prior analyses (Berta et al., 2012; Deming et al., 2013; Stevenson et al., 2013). The first approach models the systematics as an analytic function of time. The function includes an exponential ramp term fit to each orbit, a visit-long slope, and a normalization factor. The second approach assumes the morphology of the systematics is independent of wavelength, and models each channel with a scalar multiple of the time

series of systematics from the white light curve fit. We obtained consistent results from both methods (see Table A.1), and report here results from the second. See the supplementary information presented in Appendix A for more detail on the observations, data reduction, and systematics correction.

We fit the light curves in each spectroscopic channel with a transit model (Mandel & Agol, 2002) to measure the transit depth as a function of wavelength; this constitutes the transmission spectrum. See Figure 2.1 for the fitted transit light curves. We used the second systematics correction technique described above and fit a unique planet-to-star radius ratio R_p/R_s and normalization C to each channel and each visit, and a unique linear limb darkening parameter u to each channel. We assumed a circular orbit (Anglada-Escudé et al., 2013) and fixed the inclination $i = 89.1°$, the ratio of the semi-major axis to the stellar radius $a/R_s = 15.23$, the orbital period $P = 1.58040464894$ days, and the time of central transit $T_c = 2454966.52488$ $\mathrm{BJD_{TDB}}$. These are the best fit values to the white light curve.

The measured transit depths in each channel are consistent over all transit epochs (see Fig. A.5), and we report the weighted average depth per channel. The resulting transmission spectrum is shown in Figure 2.2. Our results are not significantly affected by stellar activity, as we discuss further in Appendix A. Careful treatment of the limb darkening is critical to the results, but our limb darkening measurements are not degenerate with the transit depth (see Figure A.4) and agree with the predictions from theoretical models (see Figure A.6). Our conclusions are unchanged if we fix the limb darkening on theoretical values. We find that a linear limb darkening law is sufficient to model the data. For further description of the limb darkening treatment, see Appendix A.

2.3 Implications for the Atmosphere

The transmission spectrum we report here has the precision necessary to detect the spectral features of a high mean molecular mass atmosphere for the first time. However, the observed spectrum is featureless. The data are best fit with a flat line, which has a reduced χ^2 of

Figure 2.1: Spectrophotometric Data for Transit Observations of GJ 1214b

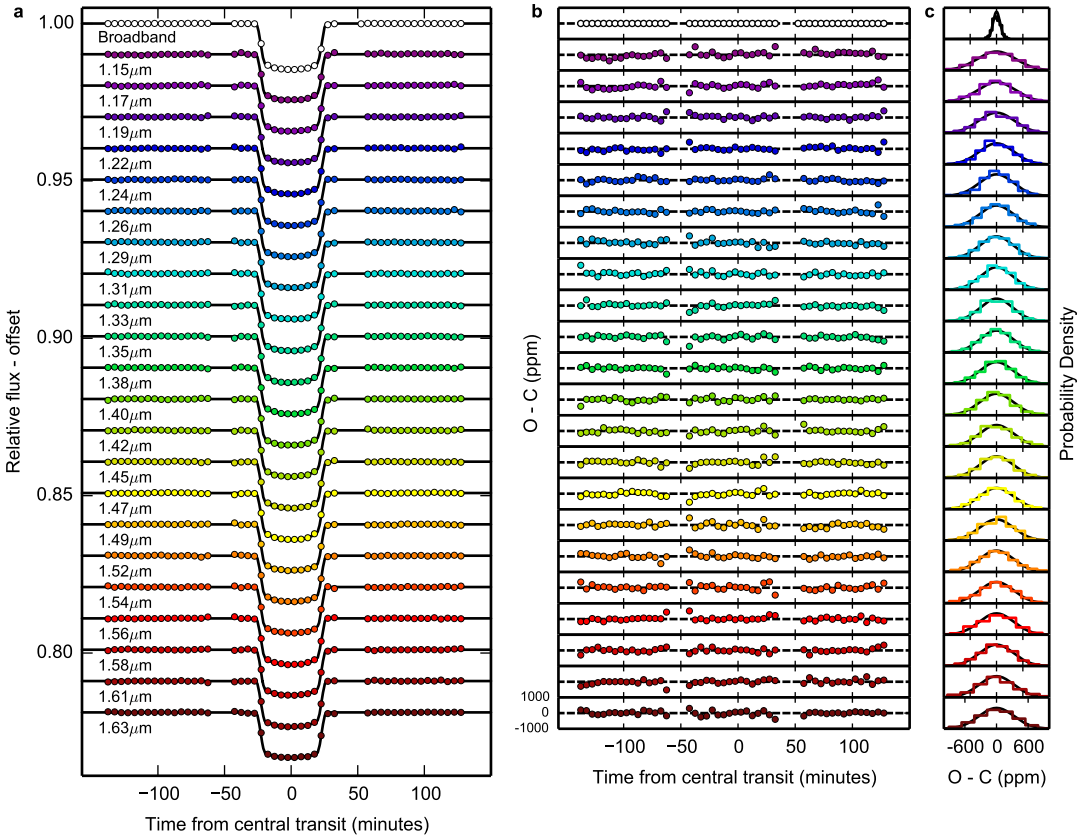

Panel **a**: Normalized and systematics-corrected data (points) with best-fit transit models (lines), offset for clarity. The data consist of 12 transit observations and are binned in phase in 5-minute increments. The spectroscopic light curve fit parameters are transit depth, a linear limb darkening coefficient, and a normalization term to correct for systematics. A unique transit depth is determined for each observation and the measured transit depths are consistent from epoch to epoch in all channels. Panel **b**: Binned residuals from the best-fit model light curves. The residuals are within 14% of the predicted photon-limited shot noise in all spectroscopic channels. The median observed rms in the spectroscopic channels is 315 ppm, prior to binning. **c**, Histograms of the unbinned residuals (colored lines) compared to the expected photon noise (black lines). The residuals are Gaussian, satisfying a Shapiro-Wilk test for normality at the the $\alpha = 0.1$ level in all but one channel (1.24 μm). The median reduced χ^2 value for the spectroscopic light curve fits is 1.02.

Figure 2.2: The Transmission Spectrum of GJ 1214b

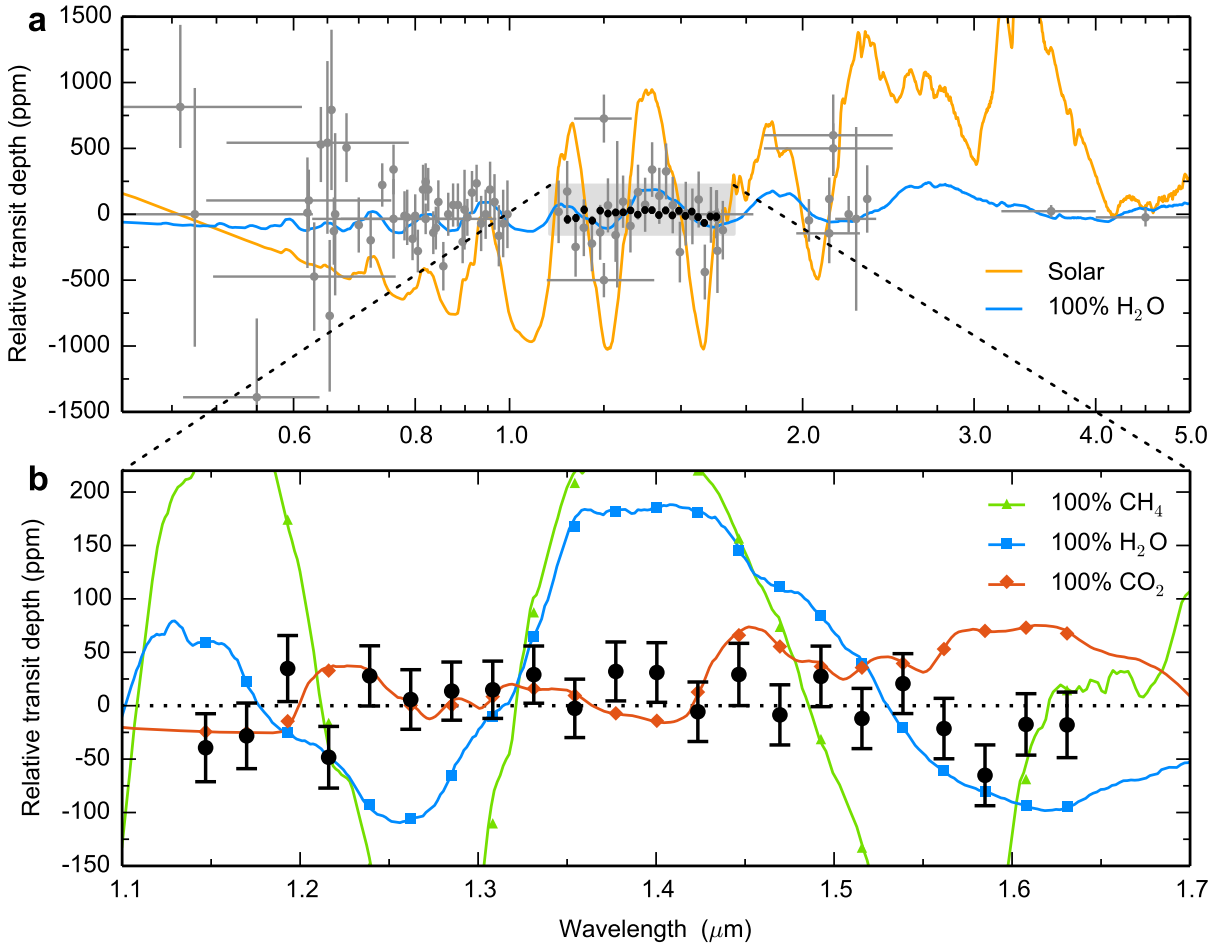

Panel **a**: Transmission spectrum measurements from our data (black points) and previous work (gray points)Bean et al. (2010); Désert et al. (2011); Bean et al. (2011); Berta et al. (2012); Fraine et al. (2013), compared to theoretical models (lines). The error bars correspond to $1\,\sigma$ uncertainties. Each data set is plotted relative to its mean. Our measurements are consistent with past results for GJ 1214 using WFC3Berta et al. (2012). Previous data rule out a cloud-free solar composition (orange line), but are consistent with a high-mean molecular weight atmosphere (e.g. 100% water, blue line) or a hydrogen-rich atmosphere with high-altitude clouds. Panel **b**: Detail view of our measured transmission spectrum (black points) compared to high mean molecular weight models (lines). The error bars are $1\,\sigma$ uncertainties in the posterior distribution from a Markov chain Monte Carlo fit to the light curves (see Appendix A for details of the fits). The colored points correspond to the models binned at the resolution of the observations. The data are consistent with a featureless spectrum ($\chi^2 = 21.1$ for 21 degrees of freedom), but inconsistent with cloud-free high-mean molecular weight scenarios. Fits to pure water (blue line), methane (green line), carbon monoxide (not shown), and carbon dioxide (red line) models have $\chi^2 = 334.7$, 1067.0, 110.0, and 75.4 with 21 degrees of freedom, and are ruled out at 16.1, 31.1, 7.5, and $5.5\,\sigma$ confidence, respectively.

1.0. We compare several models to the data that represent limiting case scenarios in the range of expected atmospheric compositions (Benneke & Seager, 2013; Fortney et al., 2013). Depending on the formation history and evolution of the planet, a high mean molecular mass atmosphere could be dominated by water (H_2O), methane (CH_4), carbon monoxide (CO), carbon dioxide (CO_2), or nitrogen (N_2). Water is expected to be the dominant absorber in the wavelength range of our observations, so a wide range of high mean molecular mass atmospheres with trace amounts of water can be approximated by a pure H_2O model. The data show no evidence for water absorption. A cloud-free pure H_2O composition is ruled out at $16.1\,\sigma$ confidence. In the case of a dry atmosphere, features from other absorbers such as CH_4, CO, or CO_2 could be visible in the transmission spectrum. Cloud-free atmospheres composed of these absorbers are also excluded by the data, at 31.1, 7.5, and $5.5\,\sigma$ confidence, respectively. Nitrogen has no spectral features in the observed wavelength range, but our measurements are sensitive to a nitrogen-rich atmosphere with trace amounts of spectrally active molecules. For example, we can rule out a 99.9% N_2, 0.1% H_2O atmosphere at $5.6\,\sigma$ confidence. Of the scenarios considered here, a 100% CO_2 atmosphere is the most challenging to detect because CO_2 has the highest molecular mass and a relatively small opacity in the observed wavelength range. Given that the data are precise enough to rule out even a CO_2 composition at high confidence, the most likely explanation for the absence of spectral features is a gray opacity source, suggesting that clouds are present in the atmosphere. Clouds can block transmission of stellar flux through the atmosphere, which truncates spectral features arising from below the cloud altitude (Fortney, 2005).

To illustrate the properties of potential clouds, we perform a Bayesian analysis on the transmission spectrum with a code designed for spectral retrieval of super-Earth atmospheric compositions (Benneke & Seager, 2012). We assume a two-component model atmosphere of water and a solar mix of hydrogen/helium gas, motivated by the fact that water is the most abundant icy volatile for solar abundance ratios. Clouds are modeled as a gray, optically thick opacity source below a given altitude. See Figure 2.3 for the retrieval results. For this

model, the data constrain the cloud top pressure to less than 10^{-2} mbar for a mixing ratio with mean molecular mass equal to solar and less than 10^{-1} mbar for a water-dominated composition (both at $3\,\sigma$ confidence). At the temperatures and pressures expected in the atmosphere of GJ 1214b, equilibrium condensates of ZnS and KCl can form in the observable part of the atmosphere. While these species could provide the necessary opacity, they are predicted to form at much higher pressures (deeper than 10 mbar for a 50x solar metallicity model; Morley et al., 2013), requiring that clouds be lofted high from their base altitude to explain our measured spectrum. Alternatively, photochemistry could produce a layer of hydrocarbons in the upper atmosphere, analogous to the haze on Saturn's moon Titan (Miller-Ricci Kempton et al., 2012; Morley et al., 2013).

2.4 Conclusions

The result presented here demonstrates the capability of current facilities to measure very precise spectra of exoplanets by combining many transit observations. This observational strategy has the potential to yield the atmospheric characterization of an Earth-size planet orbiting in the habitable zone of a small, nearby star. Transmission spectrum features probing five scale heights of a nitrogen-rich atmosphere on such a planet would have an amplitude of 30 ppm, which is comparable to the photon-limited measurement precision we obtained with the Hubble Space Telescope. However, our findings for the super-Earth archetype GJ 1214b, as well as emerging results for hot, giant exoplanets (Pont et al., 2008; Deming et al., 2013), suggest that clouds may exist across a wide range of planetary atmosphere compositions, temperatures, and pressures. Clouds generally do not have constant opacity at all wavelengths, so further progress in this area can be made by obtaining high-precision data with broad spectral coverage. Another avenue forward is to focus on measuring exoplanet emission and reflection spectra during secondary eclipse, because the optical depth of clouds viewed at near-normal incidence is lower than that for the slant geometry observed during transit (Fortney, 2005). Fortunately, the next generation of large ground-based telescopes

Figure 2.3: Spectral Retrieval Results for a Two-Component (H/He and Water) Model Atmosphere for GJ 1214b

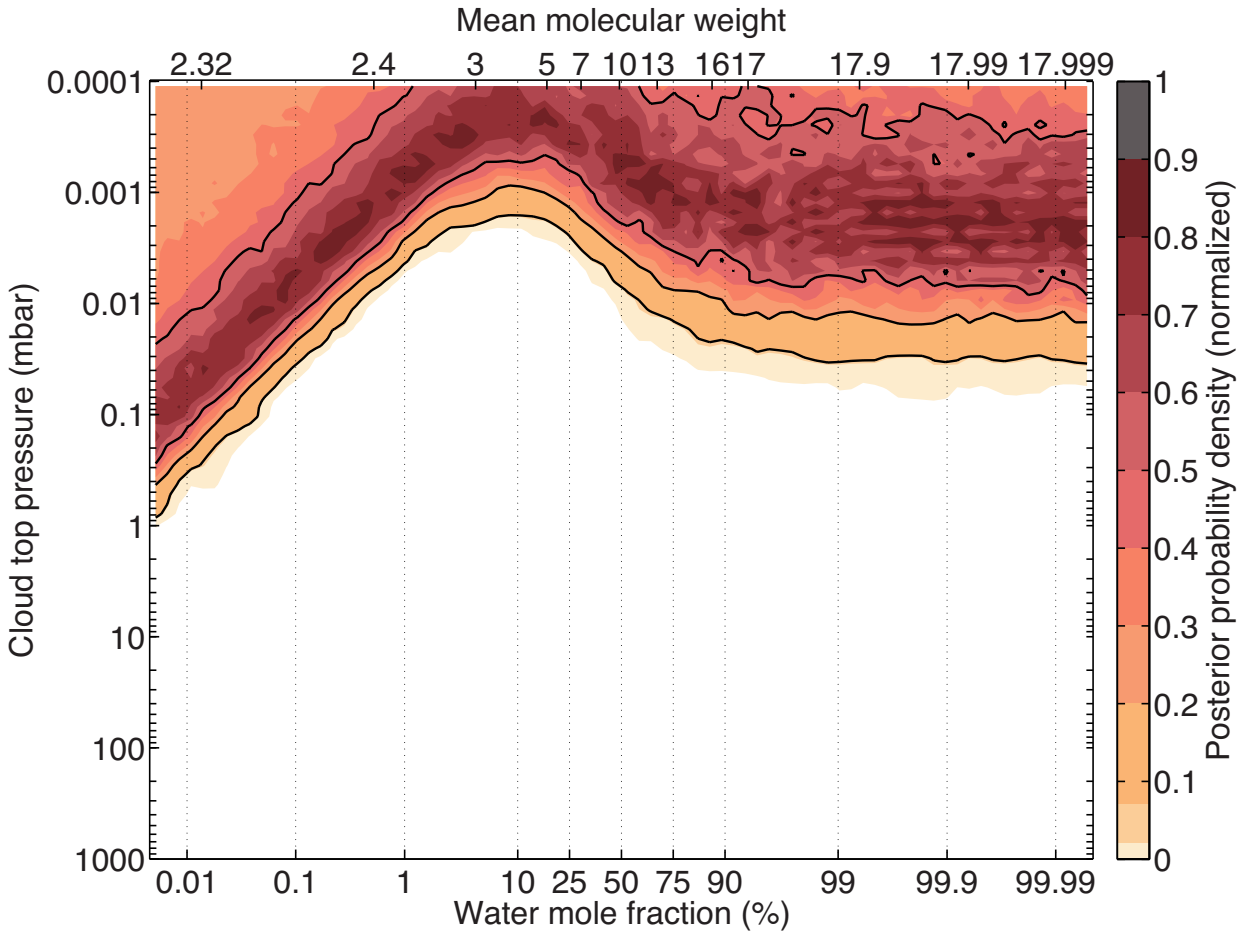

Retrieved water abundance and cloud top pressure for GJ 1214b. Colors indicate posterior probability density. Black contours mark the 1, 2, and 3 σ Bayesian credible regions. Clouds are modeled with a gray opacity, with transmission truncated below the cloud altitude. The atmospheric modeling assumes a surface gravity of 8.48 m/s^2 and an equilibrium temperature equal to 580 K.

and the James Webb Space Telescope will have the capabilities to make these kinds of measurements, bringing us within reach of characterizing potentially habitable worlds beyond our Solar System.

CHAPTER 3

A PRECISE WATER ABUNDANCE MEASUREMENT FOR THE HOT JUPITER WASP-43b

The water abundance in a planetary atmosphere provides a key constraint on the planet's primordial origins because water ice is expected to play an important role in the core accretion model of planet formation. However, the water content of the Solar System giant planets is not well known because water is sequestered in clouds deep in their atmospheres. By contrast, short-period exoplanets have such high temperatures that their atmospheres have water in the gas phase, making it possible to measure the water abundance for these objects. We present a precise determination of the water abundance in the atmosphere of the $2\,M_{Jup}$ short-period exoplanet WASP-43b based on thermal emission and transmission spectroscopy measurements obtained with the *Hubble Space Telescope*. We find the water content is consistent with the value expected in a solar composition gas at planetary temperatures ($0.4 - 3.5\times$ solar at $1\,\sigma$ confidence). The metallicity of WASP-43b's atmosphere suggested by this result extends the trend observed in the Solar System of lower metal enrichment for higher planet masses.

3.1 Introduction

Water ice is an important building block for planet formation under the core accretion paradigm (Pollack et al., 1996). According to this model, protoplanetary cores form by sticky collisions of planetesimals. Once the cores reach a threshold mass, they experience runaway accretion of nearby material. Beyond the water frost line, water is expected to be the dominant component by mass of planetesimals in solar composition protoplanetary disks (Marboeuf et al., 2008; Johnson et al., 2012). Measurements of a planet's water content can therefore help constrain the disk chemistry, location, and surface density of solids where it formed (e.g. Lodders, 2004; Mousis et al., 2009; Öberg et al., 2011; Madhusudhan et al.,

2011b; Mousis et al., 2012; Helled & Lunine, 2014; Marboeuf et al., 2014).

Despite water's important role in planet formation, there are few observational constraints on the bulk abundance of water in gas giant planets. The Solar System giants have such low temperatures that water has condensed into clouds deep in their atmospheres, and is not easily accessible to remote observations (Guillot & Gautier, 2014). The Galileo probe mass spectrometer entered Jupiter's atmosphere and provided a direct measurement of the water abundance, but found a surprisingly small value ($0.29 \pm 0.10\times$ solar) which contrasts with the $2-5\times$ solar enhancement of most other volatile species (Wong et al., 2004). The reliability of the water measurement is uncertain given local meteorological effects at the probe entry point (Showman & Ingersoll, 1998) and it is generally considered a lower limit. One of the main goals of NASA's JUNO mission, which is scheduled to arrive at Jupiter in 2016, is to make a new measurement of the atmospheric water abundance (Matousek, 2007).

In contrast to the Solar System planets, hot exoplanets should harbor gaseous water in their observable atmospheres. Detections of water have been reported for a number of giant exoplanets (Grillmair et al., 2008; Konopacky et al., 2013; Deming et al., 2013; Birkby et al., 2013), and some previous measurements have yielded precise constraints on the abundance of water in these objects (Lee et al., 2013; Line et al., 2014; Madhusudhan et al., 2014b). However, interpretation of past results has been challenging for cases when theoretical models do not provide good fits to the observed spectra (e.g. Line et al., 2014) and when measurement reproducibility has been questioned (e.g. Swain et al., 2009; Gibson et al., 2011).

The Wide Field Camera 3 (WFC3) instrument on the *Hubble Space Telescope* (*HST*) has enabled transit and eclipse observations of exoplanets that give repeatable results over year-long time baselines (Kreidberg et al., 2014b) and consistent measurements with multiple analysis techniques (Deming et al., 2013; Kreidberg et al., 2014b; Knutson et al., 2014b; McCullough et al., 2014). We use *HST*/WFC3 to measure precise transmission and emission spectra for the 2 M_{Jup}, short-period exoplanet WASP-43b that enable comparative

planetology with gas giants in the Solar System.

3.2 Observations and Data Reduction

We observed three full-orbit phase curves, three primary transits, and two secondary eclipses of WASP-43b with 61 *HST* orbits as part of GO Program 13467. During the observations, we obtained low-resolution time series spectroscopy with the WFC3 G141 grism over the wavelength range 1.1 to 1.7 μm. The phase curves each span the entire orbital period of the planet (19.5 hours) and include coverage of a transit and eclipse, yielding a total of six transit and five eclipse observations. Further details of the observing campaign are described in (Stevenson et al., 2014d). We focus here on constraints on the planet's water abundance obtained from the transit and eclipse data.

We extracted spectroscopic light curves from the data using a technique outlined in past work (Kreidberg et al., 2014b). In our analysis, we used a subset of the total observations, including only spectra obtained within 160 minutes of the time of central transit or eclipse. We fit the spectroscopic light curves to derive transmission and emission spectra, shown in Figure 3.1.

The light curve fits consisted of either a transit or eclipse model (as appropriate, Mandel & Agol, 2002) multiplied by an analytic function of time used to correct systematic trends in the data. The dominant systematic is an *HST* orbit-long ramp (Berta et al., 2012; Deming et al., 2013; Kreidberg et al., 2014b; Wilkins et al., 2014), which we fit with an exponential function (using the `model-ramp` parameterization from Kreidberg et al., 2014b). The free parameters in our transit model are the planet-to-star radius ratio and a linear limb darkening coefficient. The eclipse model has one free parameter, the planet-to-star flux ratio. In all of our spectroscopic light curve fits, we fixed the orbital inclination to 82.1°, the ratio of semimajor axis to stellar radius to 4.872, and the time of central transit to 2456601.02748 $\mathrm{BJD_{TDB}}$ based on the best fit to the band-integrated ("white") transit light curve. For the eclipse data, we also fixed the planet-to-star radius ratio to $R_p/R_s = 0.12$. Our models use

an orbital period equal to 0.81347436 days (Blecic et al., 2014). The secondary eclipse time measured from the white eclipse light curve is consistent with a circular orbit, so we assume zero eccentricity for our spectroscopic light curve fits.

We show the transit and eclipse depths from this analysis in Table 3.1 and the transmission and emission spectra in Figure 3.1. All of the fitted light curves have residuals within 10% of the predicted photon+read noise. The median reduced chi-squared for the fits is 1.0 (for both transit and eclipse light curves). We measure consistent depths from epoch to epoch, which suggests that stellar variability does not significantly impact our measurements. We obtained further confirmation of this from photometric monitoring of WASP-43 that shows minimal variation, indicating that the effect of starspots is below the precision of our data.

3.3 Analysis

We retrieved the planet's atmospheric properties by fitting the transmission and dayside emission spectra with the CHIMERA Bayesian retrieval suite (Line et al., 2013b; Line & Yung, 2013a; Line et al., 2014). The retrieval constrains the molecular abundances and the temperature-pressure (T-P) profile of WASP-43b's atmosphere. In addition to our *HST* data, we included two high-precision, 3.6- and 4.5-μm broadband photometric *Spitzer Space Telescope*/IRAC secondary eclipse measurements (Blecic et al., 2014) in the retrieval. We found that using the highest-precision ground-based secondary eclipse measurements (Gillon et al., 2012) did not significantly affect our results, so our final analysis incorporates data from *HST* and *Spitzer* only.

We analyzed the transmission and emission spectra independently. In both cases, we retrieved the abundances of H_2O, CH_4, CO, and CO_2, which are expected to be the dominant opacity sources at the observed wavelengths for a hydrogen-rich atmosphere. Our model also includes collision-induced H_2/He absorption. We explored the effects of including the additional chemical species H_2S, NH_3, K, and FeH, and found that our results were

Table 3.1. Transit and Eclipse Depths for WASP-43b

Wavelength (μm)	Transit Depth[a] (ppm)	Wavelength (μm)	Eclipse Depth (ppm)
1.135 – 1.158	96 ± 54	1.125 – 1.160	367±45
1.158 – 1.181	-14 ± 52	1.160 – 1.195	431±39
1.181 – 1.204	-24 ± 49	1.195 – 1.230	414±38
1.205 – 1.228	-134 ± 52	1.230 – 1.265	482±36
1.228 – 1.251	56 ± 49	1.265 – 1.300	460±37
1.251 – 1.274	-14 ± 52	1.300 – 1.335	473±33
1.274 – 1.297	-24 ± 49	1.335 – 1.370	353±34
1.297 – 1.320	-14 ± 50	1.370 – 1.405	313±30
1.320 – 1.343	6 ± 45	1.405 – 1.440	320±36
1.343 – 1.366	156 ± 50	1.440 – 1.475	394±36
1.366 – 1.389	126 ± 46	1.475 – 1.510	439±33
1.389 – 1.412	116 ± 49	1.510 – 1.545	458±35
1.412 – 1.435	36 ± 46	1.545 – 1.580	595±36
1.435 – 1.458	-34 ± 51	1.580 – 1.615	614±37
1.458 – 1.481	-84 ± 46	1.615 – 1.650	732±42
1.481 – 1.504	-44 ± 51		
1.504 – 1.527	6 ± 47		
1.527 – 1.550	6 ± 48		
1.550 – 1.573	-14 ± 49		
1.573 – 1.596	-54 ± 49		
1.596 – 1.619	-74 ± 53		
1.619 – 1.642	-74 ± 51		

[a]Transit depths are given relative to the mean over all wavelengths, which is 2.5434%.

Figure 3.1: Emission and Transmission Spectra for WASP-43b

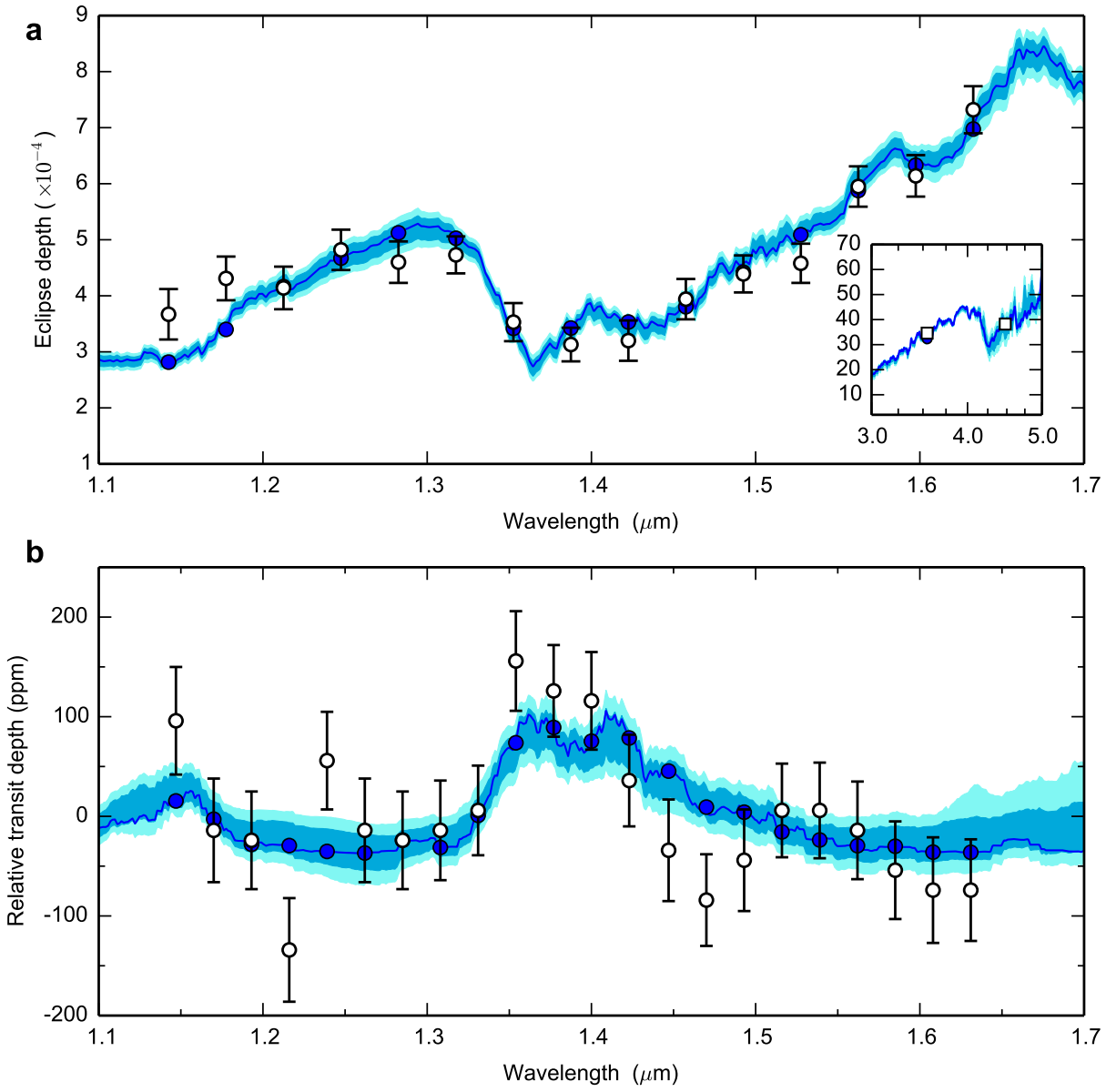

Panel **a**: The emission spectrum measurements from *HST*/WFC3 (white circles) and *Spitzer*/IRAC (white squares; inset). Panel **b**: The transmission spectrum from WFC3 (white circles). For both panels, the uncertainties correspond to 1 σ errors from a Markov chain fit. The error bars for the *Spitzer* measurements are smaller than the symbols. We show the best fit models from our retrieval analysis (dark blue lines) with 1- and 2-σ confidence regions denoted by blue and cyan shading. The blue circles indicate the best fit model averaged over the bandpass of each spectroscopic channel. The fits to both the emission and transmission spectra have chi-squared values nearly equal to the number of data points n ($\chi^2/n = 1.2$ for both).

unchanged.

For the emission spectrum retrieval, we used a five-parameter model for the T-P profile motivated by analytic gray radiative-equilibrium solutions (Parmentier & Guillot, 2014). The model fits a one-dimensional T-P profile to the hemispherically averaged emission spectrum. For the transmission spectrum modeling, we retrieved an effective scale height temperature, a reference pressure at which the fiducial radius is defined, and an opaque gray cloud top pressure, in addition to the molecular abundances (Line & Yung, 2013b). The distributions of retrieved parameters are shown in Figure 3.2. The retrieved T-P profile for the dayside emission spectrum is presented in Stevenson et al. (2014d).

3.4 Results

3.4.1 Constraints from the Emission Spectrum

The emission spectrum shows strong evidence for water absorption. We detect water at $11.7\,\sigma$ confidence ($6.4\,\sigma$ from the WFC3 data alone), according to the Bayesian information criterion (BIC). The data constrain the volume mixing ratio of H_2O in the planet's atmosphere to be 3.1×10^{-4} – 4.4×10^{-3} at $1\,\sigma$ confidence. Figure 3.3 shows the distribution of H_2O abundances that fit the observations.

Water is the only molecule significantly detected over the WFC3 wavelength range; however, additional constraints from the *Spitzer* data suggest CO and/or CO_2 are also present in the planet's atmosphere. We detect CO+CO_2 at $4.7\,\sigma$ confidence in the combined WFC3/IRAC spectrum. The measured abundance of CO_2 is relatively high compared to the expected thermochemical value for a solar composition gas ($\sim 5 \times 10^{-8}$). We find that a moderately super-solar metallicity composition has equilibrium H_2O, CO_2, and CO abundances that are within the range of our retrieved values. However, the CO+CO_2 constraints are driven mainly by the photometric point from the *Spitzer* 4.5 μm channel. The bandpass for this channel is about 1 μm wide, and covers features from CO, CO_2, and H_2O (Sharp

Figure 3.2: Pairs Plots of Retrieved Parameters

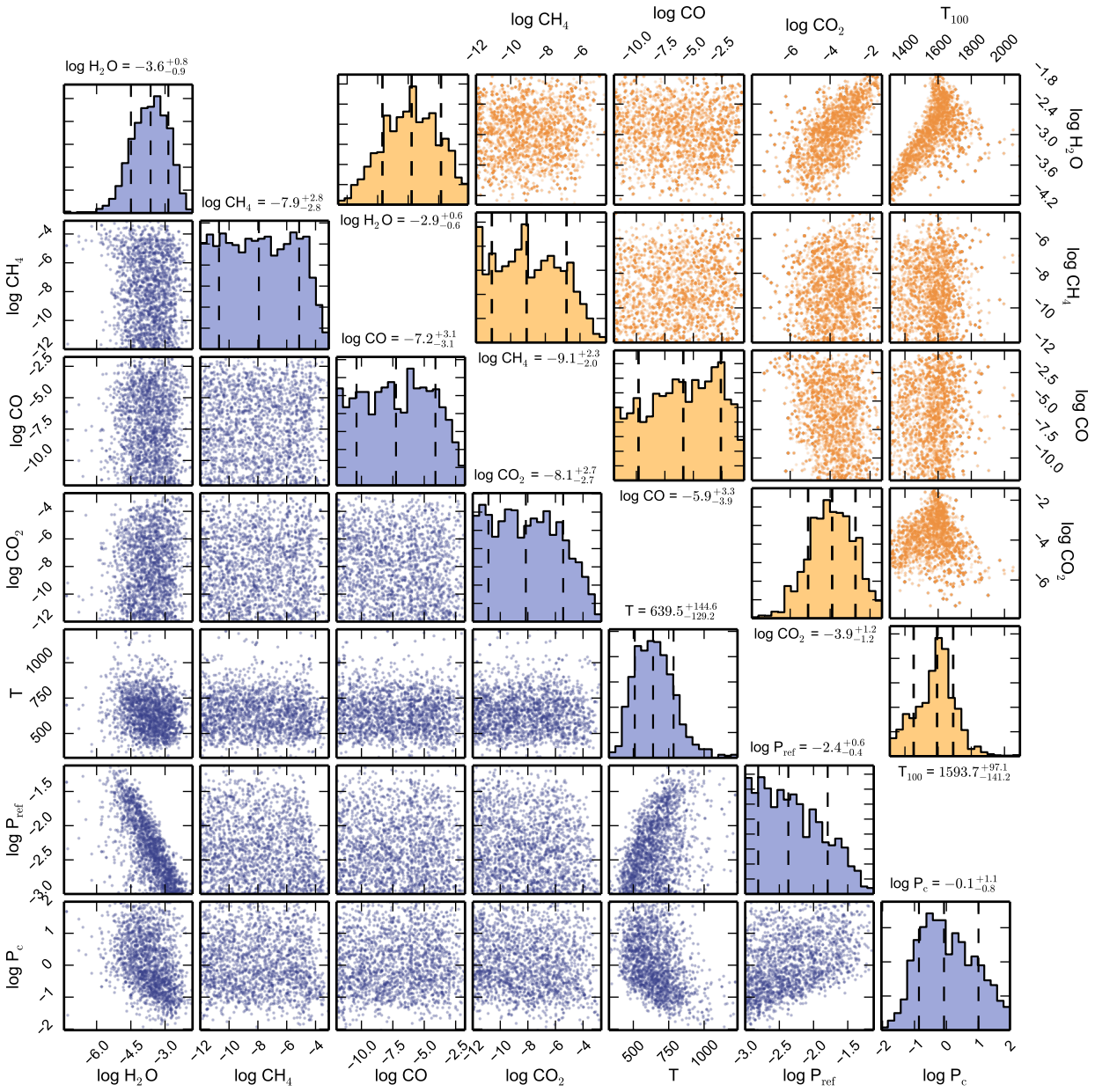

Retrieved parameters from the emission spectrum (top right) and the transmission spectrum (lower left). We plot every tenth point from our MCMC chains. For the emission spectrum fits, we show constraints on the retrieved molecular abundances (in units of log mixing ratio) and the temperature at the 100 mbar pressure level (T_{100}, in Kelvin). For the transmission spectrum, we show constraints on the molecular abundances (in units of log mixing ratio), the scale height temperature (in Kelvin), the reference pressure $P_{\rm ref}$ (in bars), and the cloud-top pressure P_c (in bars).

& Burrows, 2007). Making a robust determination of the abundances of these molecules requires spectroscopic observations to resolve their absorption features. The main conclusions of this work are unchanged if we exclude the *Spitzer* data from our analysis.

The best-fit thermal profile has decreasing temperature with pressure and is consistent with predictions from a radiative-convective model for the substellar point over the range of pressures to which our data are sensitive. We find no evidence for a thermal inversion. Further details of the thermal structure of the planet's atmosphere are available in Stevenson et al. (2014d).

3.4.2 Constraints from the Transmission Spectrum

We obtain complementary results for the atmospheric composition based on a retrieval for the transmission spectrum. Water absorption is detected at $5\,\sigma$ confidence and is visible in the data, shown in Figure 4.3 (panel b). The transmission spectrum fit allows a water volume mixing ratio between 3.3×10^{-5} and 1.4×10^{-3} at $1\,\sigma$, which is consistent with the bounds derived from the emission measurements. No other molecules are detected in the spectrum according to the BIC. The constraints on the water abundance (shown in Figure 3.3) are broader than those obtained from the emission spectrum because the abundance is correlated with the reference pressure level, which is only weakly constrained by the observations. We remind the reader that the size of features in the transmission spectrum is controlled by the molecular abundances, the planet's atmospheric scale height, and the radius of the planet relative to the star (Miller-Ricci et al., 2009b).

In addition to probing the atmospheric composition, the data also constrain the temperature at the terminator and the cloud top pressure. The $1\,\sigma$ confidence interval on the scale height temperature is 500–780 K. We find no evidence for a cloud at the pressure levels to which our observations are sensitive.

3.4.3 Joint Constraint on the Water Abundance

We derive consistent water abundances for WASP-43b from the emission and transmission spectra. This consistency matches the prediction from theoretical models of hot Jupiters that water has a nearly uniform abundance with both pressure (from 10 to 10^{-8} bar) and with temperature (Moses et al., 2011). Therefore, to obtain a more precise estimate of WASP-43b's water abundance, we assume the regions of the atmosphere probed by the emission and transmission data have the same water content. Because the measurements are independent, we can combine their constraints by multiplying the probability distributions for water abundance retrieved from each data set. This yields a joint distribution, shown in Figure 3.3, which constrains the water volume mixing ratio to 2.4×10^{-4} – 2.1×10^{-3} at $1\,\sigma$ confidence. This measurement contrasts with the sub-solar water abundance values reported for three other hot Jupiters by Madhusudhan et al. (2014b), and suggests that additional observations are needed to understand the diversity in composition of these objects.

3.5 Discussion

3.5.1 Comparison with Solar System Planets

With our well-determined water abundance for the atmosphere of WASP-43b, we can begin a comparative study with the giant planets in the Solar System. However, it is not possible to directly compare water abundances, because the water content in the Solar System giants is poorly constrained. We instead compare the planets' metallicities, which we estimate from chemical species with well-determined abundances. To calculate metallicity based on a molecule X, we determine the planet's enhancement in X relative to the volume mixing ratio of X expected for a solar composition gas at planetary temperatures. We use solar abundances from Asplund et al. (2009) for the calculation.

We infer the Solar System planets' metallicities from the abundance of methane, which has been precisely measured for all four giant planets. Jupiter's methane abundance is from

Figure 3.3: Water Abundance of WASP-43b

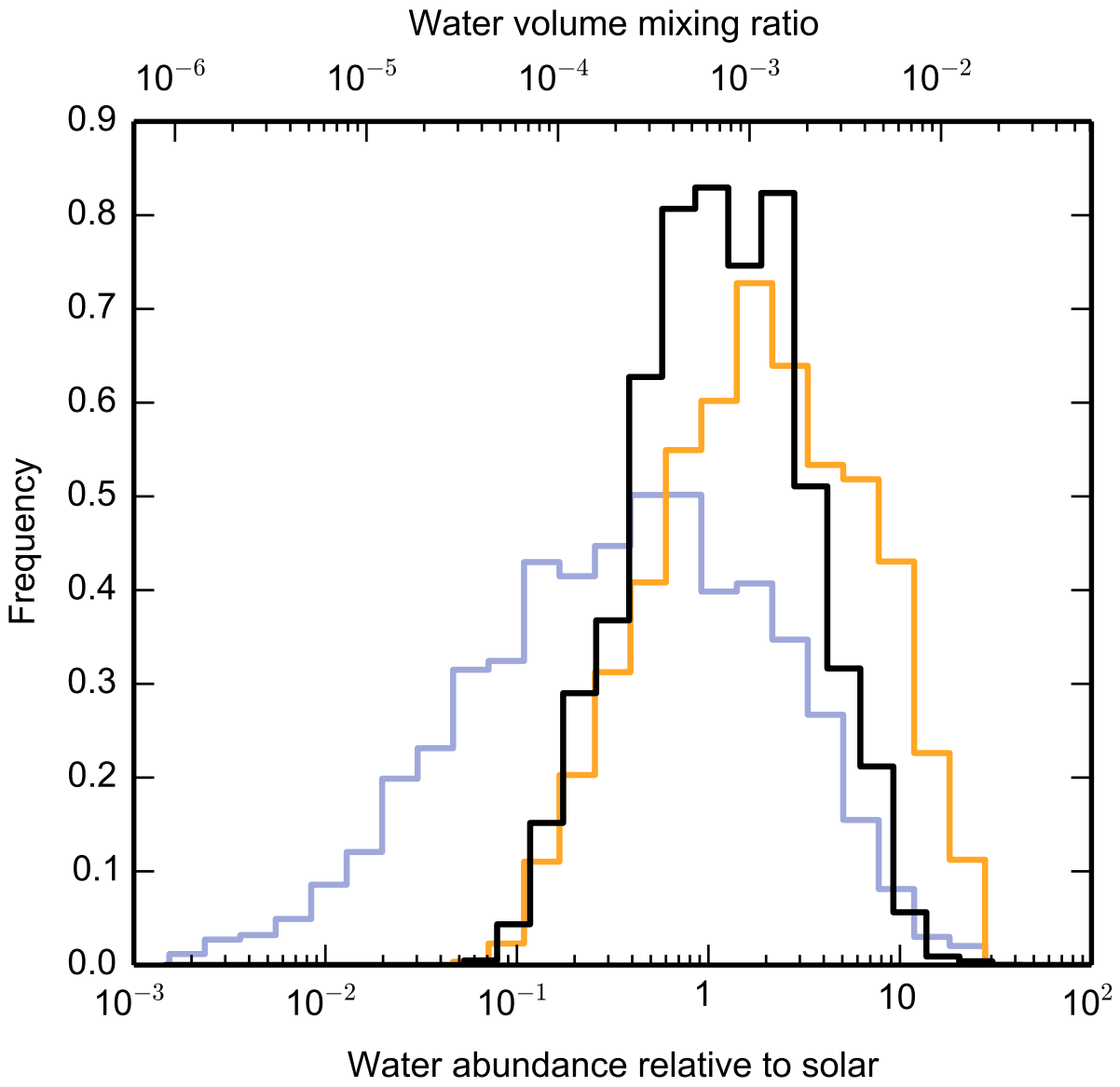

Constraints on the water abundance of WASP-43b. We show the probability distributions of water abundances measured from the emission spectrum (orange line) and transmission spectrum (blue line). The water abundance relative to solar is calculated using a "solar water abundance" of 6.1×10^{-4}, which is the water volume mixing ratio for a solar composition gas in thermochemical equilibrium at planetary temperatures. The constraints from the emission and transmission spectra are consistent with each other, in accordance with expectations from theoretical models that the water abundance is constant to within a factor of ~ 2 over the pressure levels and temperatures in the observable atmosphere (Moses et al., 2011). The joint constraint from multiplying the two probability distributions is indicated by the solid black line, and constrains the water abundance to between 3.1×10^{-4} and 4.4×10^{-3} ($0.4 - 3.5\times$ solar) at $1\,\sigma$ confidence.

the Galileo probe (Wong et al., 2004), while those of the other planets are from infrared spectroscopy (Fletcher et al., 2009; Karkoschka & Tomasko, 2011; Sromovsky et al., 2011). The $1\,\sigma$ confidence intervals for the planets' metallicities are 3.3–5.5, 9.5–10.3, 71–100, and 67–111 $\times$ solar for Jupiter, Saturn, Neptune, and Uranus, respectively. These bounds are shown in Figure 3.4.

We determine the metallicity of WASP-43b based on our measured water abundance. The planet's temperature is cooler at the terminator than at the substellar point. The difference between these temperatures leads to a factor of two discrepancy in the expected water volume mixing ratio for a solar composition gas. This difference is small relative to the uncertainty in the planet's measured water abundance, so we therefore adopt the average predicted water volume mixing ratio (6.1×10^{-4}). Using the joint constraint from the transmission and emission spectra, we find the water abundance is 0.4 to 3.5$\times$ solar at $1\,\sigma$ confidence. The $3\,\sigma$ upper limit on the water enhancement is 20$\times$ solar.

We note that determining the metallicity relative to solar composition assumes that the planets have a scaled solar abundance pattern. This assumption could lead to an incorrect estimate of metallicity in the case of non-solar abundance ratios. For example, if WASP-43b had a super-solar carbon-to-oxygen (C/O) ratio, we would expect a smaller fraction of the total oxygen to be partitioned into H_2O (Madhusudhan, 2012). We would therefore underestimate the planet's metallicity based on our assumption of solar abundances. However, given that the C/O ratio is poorly constrained by our data but broadly consistent with solar, we proceed with the comparison with these caveats in mind.

The metallicity estimates for the Solar System planets show a pattern of decreasing metal enhancement with increasing planet mass (see Figure 3.4). This trend is generally thought to be controlled by the relative importance of accretion of solid planetesimals versus H/He-dominated gas. Planet population synthesis models aim to match atmospheric metallicity to planet mass (Fortney et al., 2013; Marboeuf et al., 2014), but there are limited data available for planets outside the Solar System. The metallicity of WASP-43b indicates that the trend

seen in the Solar System may extend to exoplanets.

3.5.2 Prospects for Future Work

WASP-43b, with twice the mass of Jupiter and an orbital period of less than one day, exemplifies the opportunity exoplanets provide to study planet formation over a larger parameter space than what is available in our Solar System. A more insightful comparative planetology study using WASP-43b could be performed by improving the precision of the water abundance estimate and measuring the abundances of additional molecules. Such measurements will be enabled by the broad wavelength coverage and increased sensitivity of next-generation observing facilities such as the *James Webb Space Telescope*.

However, a planet's chemical composition depends on many factors, including the planet's formation location within the protoplanetary disk, the composition, size and accretion rate of planetesimals, and the planet's migration history. Even perfect constraints on the abundances of many chemical species for a small number of objects may not yield a unique model for the origin of giant planets. Fortunately, the plethora of transiting exoplanets that have already been found and will be discovered with future missions offer the potential for statistical studies. Measuring precise chemical abundances for a large and diverse sample of these objects would facilitate the development of a more comprehensive theory of planet formation.

Figure 3.4: Atmospheric Metallicity Versus Planet Mass

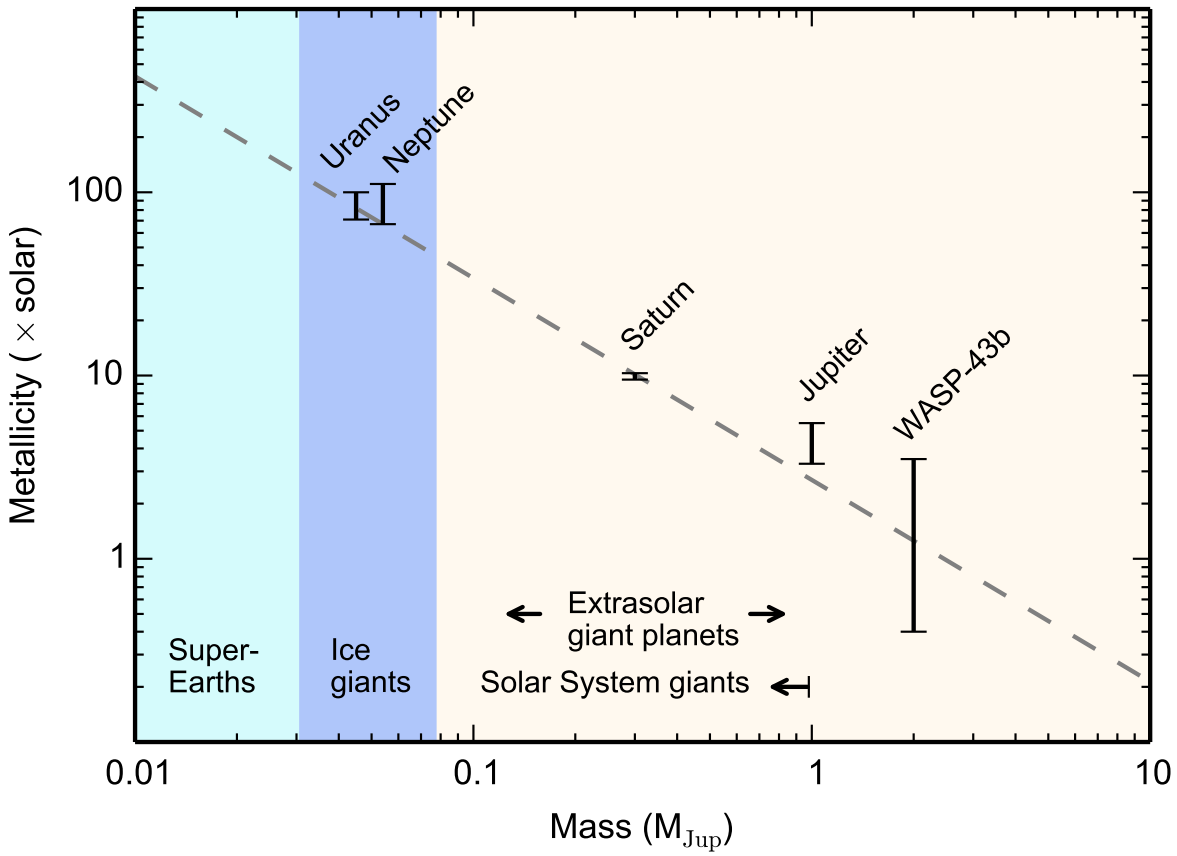

Atmospheric metal abundances as a function of planet mass for the Solar System giant planets and WASP-43b. The dashed line is a power law fit to the data. We base the metallicity estimates on the abundances of representative proxies. The Solar System planet metallicities are inferred from methane, and the metallicity of WASP-43b is based on our derived water abundance.

CHAPTER 4

A DETECTION OF WATER IN THE TRANSMISSION SPECTRUM OF THE HOT JUPITER WASP-12b AND IMPLICATIONS FOR ITS ATMOSPHERIC COMPOSITION

Detailed characterization of exoplanets has begun to yield measurements of their atmospheric properties that constrain the planets' origins and evolution. For example, past observations of the dayside emission spectrum of the hot Jupiter WASP-12b indicated that its atmosphere has a high carbon-to-oxygen ratio (C/O > 1), suggesting it had a different formation pathway than is commonly assumed for giant planets. Here we report a precise near-infrared transmission spectrum for WASP-12b based on six transit observations with the *Hubble Space Telescope*/Wide Field Camera 3. We bin the data in 13 spectrophotometric light curves from 0.84 - 1.67 μm and measure the transit depths to a median precision of 51 ppm. We retrieve the atmospheric properties using the transmission spectrum and find strong evidence for water absorption ($7\,\sigma$ confidence). This detection marks the first high-confidence, spectroscopic identification of a molecule in the atmosphere of WASP-12b. The retrieved $1\,\sigma$ water volume mixing ratio is between $10^{-5} - 10^{-2}$, which is consistent with C/O > 1 to within $2\,\sigma$. However, we also introduce a new retrieval parameterization that fits for C/O and metallicity under the assumption of chemical equilibrium. With this approach, we constrain C/O to $0.5^{+0.2}_{-0.3}$ at $1\,\sigma$ and rule out a carbon-rich atmosphere composition (C/O > 1) at $> 3\,\sigma$ confidence. Further observations and modeling of the planet's global thermal structure and dynamics would aid in resolving the tension between our inferred C/O and previous constraints. Our findings highlight the importance of obtaining high-precision data with multiple observing techniques in order to obtain robust constraints on the chemistry and physics of exoplanet atmospheres.

4.1 Introduction

The chemical composition of a planetary atmosphere provides a rich record of the planet's formation conditions and evolutionary history. Measurements of the composition can constrain the planet's formation mechanism, its formation location in the protoplanetary disk, the surface density and composition of planetesimals at the formation site, the relative accretion rates of gas and solids, and possible migration pathways (e.g. Atreya et al., 1999; Owen et al., 1999; Gautier et al., 2001; Atreya et al., 2003; Hersant et al., 2004; Lodders, 2004; Dodson-Robinson et al., 2009; Öberg et al., 2011; Madhusudhan et al., 2011a, 2014a).

Because there are many factors that influence atmospheric chemical composition, a large sample size of planets is required to develop a comprehensive theory of giant planet formation. Fortunately, the sample of known extrasolar giant planets is large and growing, and recent observations of these planets have begun to yield basic constraints on their atmospheric chemistry. These include inferences of the carbon-to-oxygen ratio (C/O) and absolute water abundance, which in some cases rival our knowledge of those quantities for the Solar System planets (e.g. Madhusudhan et al., 2011c; Konopacky et al., 2013; Line et al., 2014; Kreidberg et al., 2014a; Brogi et al., 2014; Madhusudhan et al., 2014c).

One of the best studied exoplanet atmospheres is that of the transiting hot Jupiter WASP-12b. This planet is a $1.4\,M_{\rm Jup}$, $1.8\,R_{\rm Jup}$ gas giant orbiting a late-F host star with a period of just 1.1 days (Hebb et al., 2009). The brightness of the host star (H=10.2), the planet's high equilibrium temperature (2500 K), and the planet's large size make WASP-12b a favorable target for atmosphere characterization. The system has been observed extensively from the ground and space to measure the planet's transmission spectrum, dayside emission spectrum, and thermal phase variation (López-Morales et al., 2010; Fossati et al., 2010; Campo et al., 2011; Croll et al., 2011; Cowan et al., 2012; Crossfield et al., 2012; Haswell et al., 2012; Zhao et al., 2012; Föhring et al., 2013; Sing et al., 2013; Swain et al., 2013; Mandell et al., 2013; Copperwheat et al., 2013; Stevenson et al., 2014c,b; Burton et al., 2015; Nichols et al., 2015; Croll et al., 2015).

An intriguing possibility has emerged from these observations of WASP-12b, which is that the planet has a carbon-rich atmospheric composition (C/O $>$ 1, compared to the solar value of 0.55; Asplund et al., 2009). The high C/O interpretation was first suggested by Madhusudhan et al. (2011c) as the best explanation for the planet's dayside emission spectrum. This result was contested by subsequent work (Crossfield et al., 2012; Line et al., 2014); however, the most recent comprehensive analysis of the dayside spectrum reaffirmed the inference of high C/O (Stevenson et al., 2014b).

The claim of high C/O in WASP-12b's atmosphere has motivated substantial theoretical and observational work. This includes attempts to measure C/O for additional planets (e.g. Brogi et al., 2014; Line et al., 2014), studies of the effect of C/O on atmospheric chemistry (Madhusudhan et al., 2011a; Madhusudhan, 2012; Kopparapu et al., 2012; Moses et al., 2013; Venot et al., 2015), inferences of C/O in exoplanet host stars (Teske et al., 2013, 2014), and predictions of C/O from planet formation theory (Madhusudhan et al., 2011a; Öberg et al., 2011; Madhusudhan et al., 2014a; Ali-Dib et al., 2014).

We note, however, that the evidence for a carbon-rich atmosphere on WASP-12b is not definitive. The high C/O inference is based primarily on the photometric secondary eclipse depth from *Spitzer* at 4.5 μm. The low brightness temperature for the planet in this bandpass is best explained by absorption from carbon-bearing species (either CO, HCN, or C_2H_2; Madhusudhan et al., 2011c; Kopparapu et al., 2012; Moses et al., 2013; Stevenson et al., 2014c), but photometry alone cannot uniquely identify which molecule is the dominant absorber. No other molecular features have been confidently identified in the emission spectrum, and measurements of the planet's transmission spectrum have yielded even less conclusive constraints on the C/O (Sing et al., 2013; Mandell et al., 2013; Swain et al., 2013; Stevenson et al., 2014c; Madhusudhan et al., 2014c). High-precision spectroscopy is thus needed to obtain unambiguous determination of the atmospheric composition of this important planet.

In this work, we report a new, precise measurement of WASP-12b's transmission spectrum over the wavelength range 0.84 to 1.67 μm. The outline of the paper is as follows. In § 4.2

we present the observations and data reduction. The light curves fits and measurement of the transmission spectrum are outlined in § 4.3. We compare our results to previous measurements in § 4.4. We describe a retrieval of the planet's atmospheric properties based on this transmission spectrum in § 4.5 and discuss implications for the chemical composition in § 4.6. We conclude in § 4.7.

4.2 Observations and Data Reduction

4.2.1 Observations

We obtained time series spectroscopy during six transits of WASP-12b between UT 1 January and 4 March 2014 using the Wide Field Camera 3 (WFC3) IR detector on the *Hubble Space Telescope* (*HST*) as part of *HST* GO Program 13467. Three of the transit observations used the G102 grism, which provides spectral coverage from $0.82 - 1.12$ μm, and the other three used the G141 grism, which spans the range $1.12 - 1.65$ μm. The G141 grism has been widely used for exoplanet transit spectroscopy, but these observations are the first to use the G102 grism for this purpose. The additional wavelength coverage from the G102 grism provides access to features from more molecules and absorption bands, giving us greater leverage in constraining the atmospheric composition of the planet. Each transit observation (called a visit) consisted of five consecutive, 96-minute *HST* orbits. WASP-12 was visible during approximately 45 minutes per orbit and occulted by the Earth for the remainder of the time. We took a direct image of the target with the F126N narrow-band filter at the beginning of each orbit for wavelength calibration. Example staring mode and spatial scan images are shown in Figure 4.1.

The spectroscopic data were obtained in spatial scan mode with the 256x256 subarray, using the SPARS10, NSAMP=16 readout pattern, which has an exposure time of 103.1 s. The scan rates were 0.04 and 0.05 arcsec/second for the G102 and G141 grisms, respectively. The spectra extend roughly 40 pixels in the spatial direction, with peak per-pixel counts

Figure 4.1: Raw HST/WFC3 Images for WASP-12b

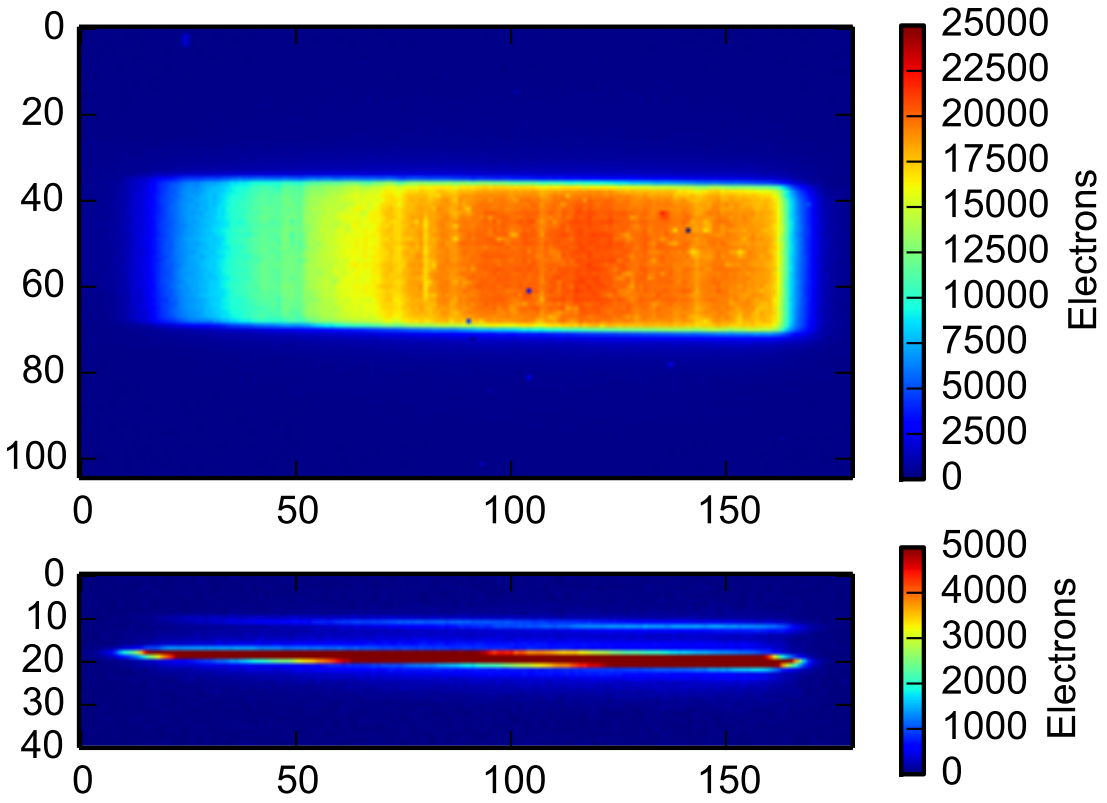

Raw *HST*/WFC3 images taken with the G102 grism. Spatial scan and staring mode data are shown in the top and bottom panels, respectively. The images are cutouts from a 256x256 pixel subarray. The spectrum of WASP-12A's binary companion is visible in the bottom panel near row 10.

Table 4.1. Summary of Photometric Observations for WASP-12

Season	N_{obs}	Date Range (HJD - 2,400,000)	Sigma (mag)	Seasonal Mean (mag)
2011-2012	126	55824-56059	0.00325	-0.28048 ± 0.00029
2012-2013	169	56189-56439	0.00297	-0.28119 ± 0.00023
2013-2014	133	56463-56799	0.00316	-0.28253 ± 0.00027

below 25,000 electrons for both grisms. We alternated between forward and reverse scanning along the detector to decrease instrumental overhead time. This setup yielded 19 exposures per orbit and a duty cycle of 74%.

In addition to the spatial scan data, we also obtained 10 staring mode spectra in each grism during the first orbit of the first visit. WASP-12 is a triple star system: WASP-12 A hosts the planet, and WASP-12 BC is an M-dwarf binary separated from WASP-12 A by about 1" (Bergfors et al., 2013; Bechter et al., 2014). We use these staring mode data to resolve the spectrum of WASP-12 A from WASP-12 BC, enabling us to correct for dilution to the planet's transit light curve due to the binary. The detector orientation was set to 178.7° in order to spatially separate the spectra. At this orientation, the spectra are separated by 7.9 pixels (compared to the FWHM of 1.1 pixel at 1.4 μm). We describe the dilution correction in detail in § 4.3.3.

We also obtained photometric monitoring of the WASP-12 system to search for stellar activity. We acquired 428 out-of-transit R-band images over the 2011-2012, 2012-2013, and 2013-2014 observing seasons with Tennessee State University's Celestron 14-inch automated imaging telescope. We tested for variability from star spots by calculating differential magnitudes for WASP-12 relative to 17 comparison stars (shown in Figure 4.2). The standard deviation of the differential magnitudes is 0.3%, which is comparable to the photon noise for the data. The brightness of the star increases by approximately 0.001 mag per year. There are no significant periodicities between 1 and 200 days. To calculate the impact of star

Figure 4.2: Photometric Monitoring

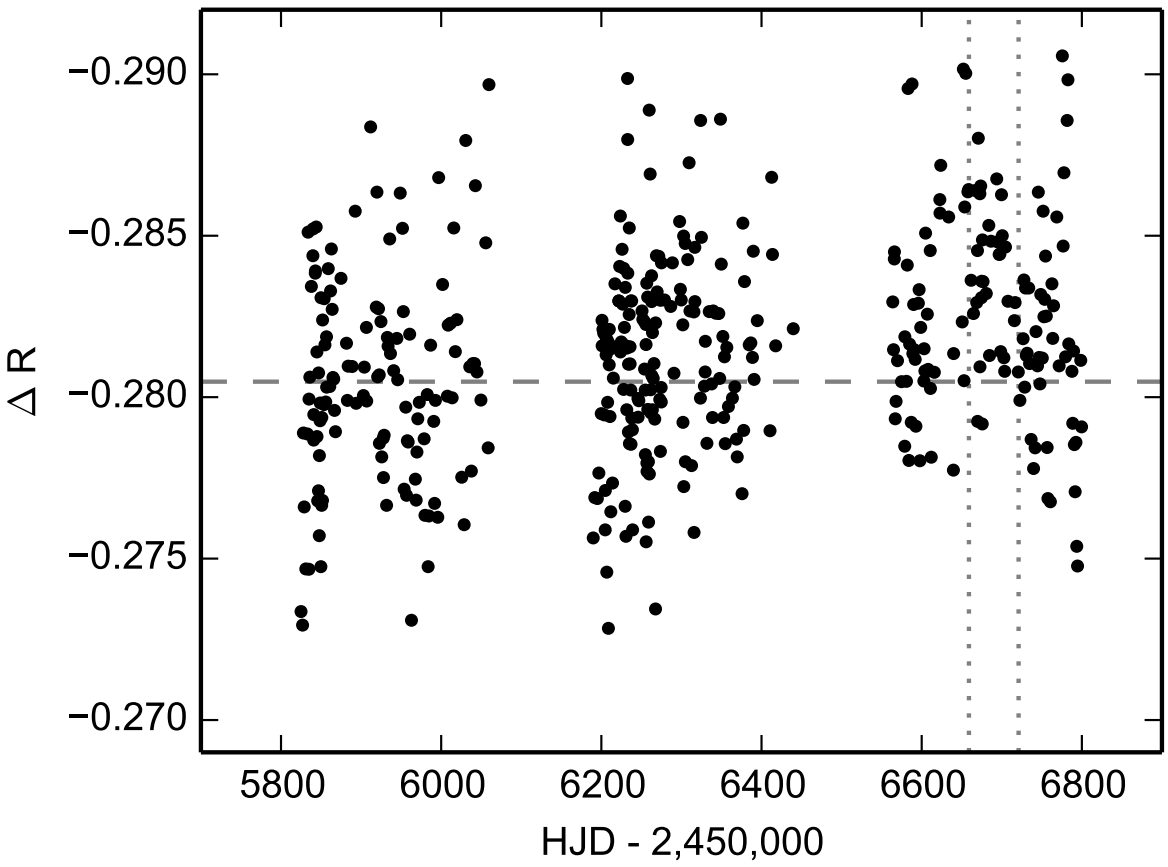

Nightly Cousins R-band photometric observations of WASP-12 over three observing seasons (points). The data are differential magnitudes relative to the average brightness of 17 comparison stars. The differential magnitudes have a mean of -0.281 and a standard deviation of 0.003. The horizontal dashed line indicates the mean brightness from the first observing season. The vertical dotted lines span the time range of the HST observations.

Figure 4.3: Example Spectra

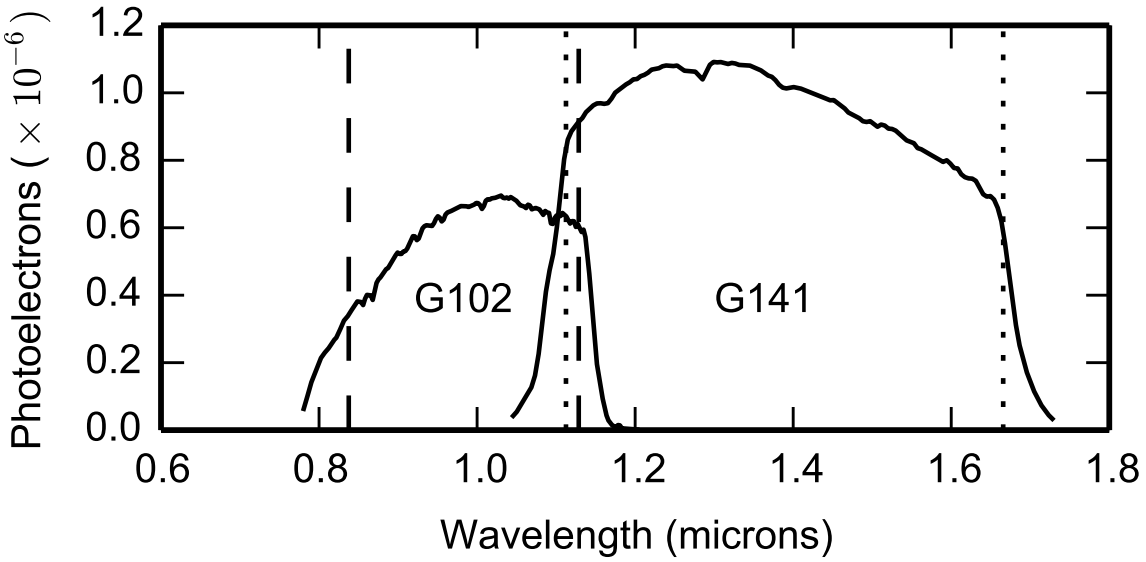

Example extracted spectra (solid lines). The wavelength ranges covered by the transmission spectra are indicated with dashed and dotted lines (for the G102 and G141 data, respectively). The uncertainties on the spectra are smaller than the plot linewidth.

spots on our transmission spectrum, we took 0.3% as an upper limit for the variability of WASP-12. Variability of this amplitude could be produced by star spots 300 K cooler than the star's effective temperature (6300 K; Hebb et al., 2009), covering 3% of the photosphere. Based on the formalism outlined in Berta et al. (2011) and Désert et al. (2011), we calculated that the maximum variation in transit depth due to spots with these properties is of order 10^{-5}, which is below the precision of our transit depth measurements.

4.2.2 Data Reduction

We reduced the *HST*/WFC3 data using the custom pipeline described in Kreidberg et al. (2014b). Example extracted spectra are shown in Figure 3.1. We bin the spectra into 24- and 15-pixel wide channels (for G102 and G141, respectively) to obtain a total of 13 spectrophotometric light curves at resolution $R \equiv \lambda/\Delta\lambda = 15 - 25$. We also sum the spectra over the full wavelength range to create broadband ("white") light curves for each grism.

The uncertainty in the flux per exposure is determined by adding in quadrature the photon noise, the read noise (22 electrons per differenced image), and the error in the estimate of the background, which we determine from the median absolute deviation of the flux values for the background pixels.

We also extract spectra from the staring mode data to determine the wavelength-dependent flux ratio of WASP-12 BC to WASP-12 A. The spectra are spatially separated on the detector, so to extract them we fit a double Gaussian model to each column of the final detector read. We obtain final estimates and uncertainties for the spectra of WASP-12 A and WASP-12 BC by taking the mean and standard deviation of the spectra from all 10 exposures. These extracted spectra are each assigned a wavelength solution using the centroids of the stars in the direct image.

4.3 Light Curve Fits

4.3.1 Broadband Light Curves

We fit the broadband light curves with a transit model (Mandel & Agol, 2002) and an analytic function to correct for instrument systematics. Transit light curve observations with *HST*/WFC3 have several well-documented systematic trends in flux with time, including visit-long slopes and orbit-long exponential ramps (Berta et al., 2012; Swain et al., 2013; Kreidberg et al., 2014b; Stevenson et al., 2014d). The first orbit of a visit has a larger amplitude ramp than subsequent orbits, so we follow established practice and do not use this initial orbit in the light curve fits. We also discard the first exposure from the remaining orbits, which improves the fit quality. We fit the remaining data (216 exposures for each grism) with a systematics model based on the `model-ramp` parameterization of Berta et al. (2012). The model $M(t)$ has the form:

$$M(t) = T(t) \times (c\,S(t) + v\,t_{\rm v}) \times (1 - \exp(-a\,t_{\rm orb} - b - D(t))). \quad (4.1)$$

In our fits, $T(t)$ is the transit model, or relative stellar flux as a function of time t (in $\mathrm{BJD_{TDB}}$). The free parameters for the transit model are the planet-to-star radius ratio k, a linear limb darkening parameter u, the ratio of semi-major axis to stellar radius a/R_s, the orbital inclination i, and the time of mid-transit T_0. The light curves have poor coverage of the planet's ingress, so we put priors on a/R_s and i to enable the measurement of T_0. We use Gaussian priors with mean and standard deviation 2.91 ± 0.02 and $80.56 \pm 0.03°$ (for a/R_s and i, respectively), based on estimates of those parameters from Stevenson et al. (2014c). We use an orbital period $P = 1.091424$ days and assume a circular orbit (Campo et al., 2011). The data from the two grisms are fit separately, but for each grism the three transits are fit simultaneously. We fit unique values of k and T_0 to each transit, but tie the values for u, a/R_s, and i over all the transits.

We fit the instrument systematics with a constant normalization term c, a scaling factor $S(t)$, a visit-long linear slope v, and an orbit-long exponential ramp with rate constant a, amplitude b, and delay $D(t)$. The timescale $t_{\rm v}$ corresponds to time relative to the expected transit midpoint for each visit, and $t_{\rm orb}$ is time since the first exposure in an orbit (both in $\mathrm{BJD_{TDB}}$). The scaling factor $S(t)$ is equal to 1 for exposures with forward spatial scanning and s for reverse scanning; this accounts for a small offset in normalization between the scan directions caused by the upstream-downstream effect of the detector readout (McCullough & MacKenty, 2012). The function $D(t)$ is equal to d for times t during the first fitted orbit and 0 elsewhere. A negative value for d implies that the ramp amplitude is larger in the first orbit than in subsequent orbits. The parameters u, a, b, and d were constrained to the same value for all the transits, whereas k, s, c, and v were allowed to vary between transits.

Table 4.2. Transit Times

Observation Start (UT)	T_c[a] ($\mathrm{BJD_{TDB}}$)	Uncertainty ($1\,\sigma$)
Jan 01 2014	6659.07598	3.4E-4
Jan 16 2014	6674.35560	2.8E-4
Feb 05 2014	6694.00161	2.9E-4
Feb 15 2014	6703.82417	2.9E-4
Mar 02 2014	6719.10428	3.4E-4
Mar 04 2014	6721.28692	3.4E-4

[a]We report the time of central transit T_c in $\mathrm{BJD_{TDB}}$ - 2,450,000.

There are a total of 21 free parameters in the fits to each grism's broadband light curve. We estimated the parameters and their uncertainties with a Markov chain Monte Carlo (MCMC) fit to the data, using the `emcee` package for Python (Foreman-Mackey et al., 2013). For the best-fit light curves, we calculated the Durbin-Watson statistic to test for time-correlated noise. The values were 1.77 and 2.17 for the G102 and G141 white light curves, indicating that the residuals are uncorrelated at the 1% significance level. The reduced chi-squared values (χ^2_ν) for the best-fit light curves are 1.45 and 1.34, and the residuals are 164 and 115 ppm (37 and 25% larger than the predicted photon+read noise) for the G102 and G141 data, respectively.

To obtain conservative estimates of the errors for the white light curve transit parameters, we redid the MCMC analyses with the per-exposure uncertainties scaled by a constant factor (1.20 and 1.16) chosen to yield $\chi^2_\nu = 1$. We report the transit times from the white light curve fits in Table 4.2. These values extend the baseline of precise transit times by two years from the Stevenson et al. (2014c) measurements and will aid in testing the possibility of perihelion precession for this system (first studied by Campo et al., 2011). The white light curves are consistent with the priors on a/R_s and i but do not yield improved values for those parameters due to the poor phase coverage of the transit ingress.

4.3.2 Spectroscopic Light Curves

Figure 4.4: Spectroscopic Light Curve Fit

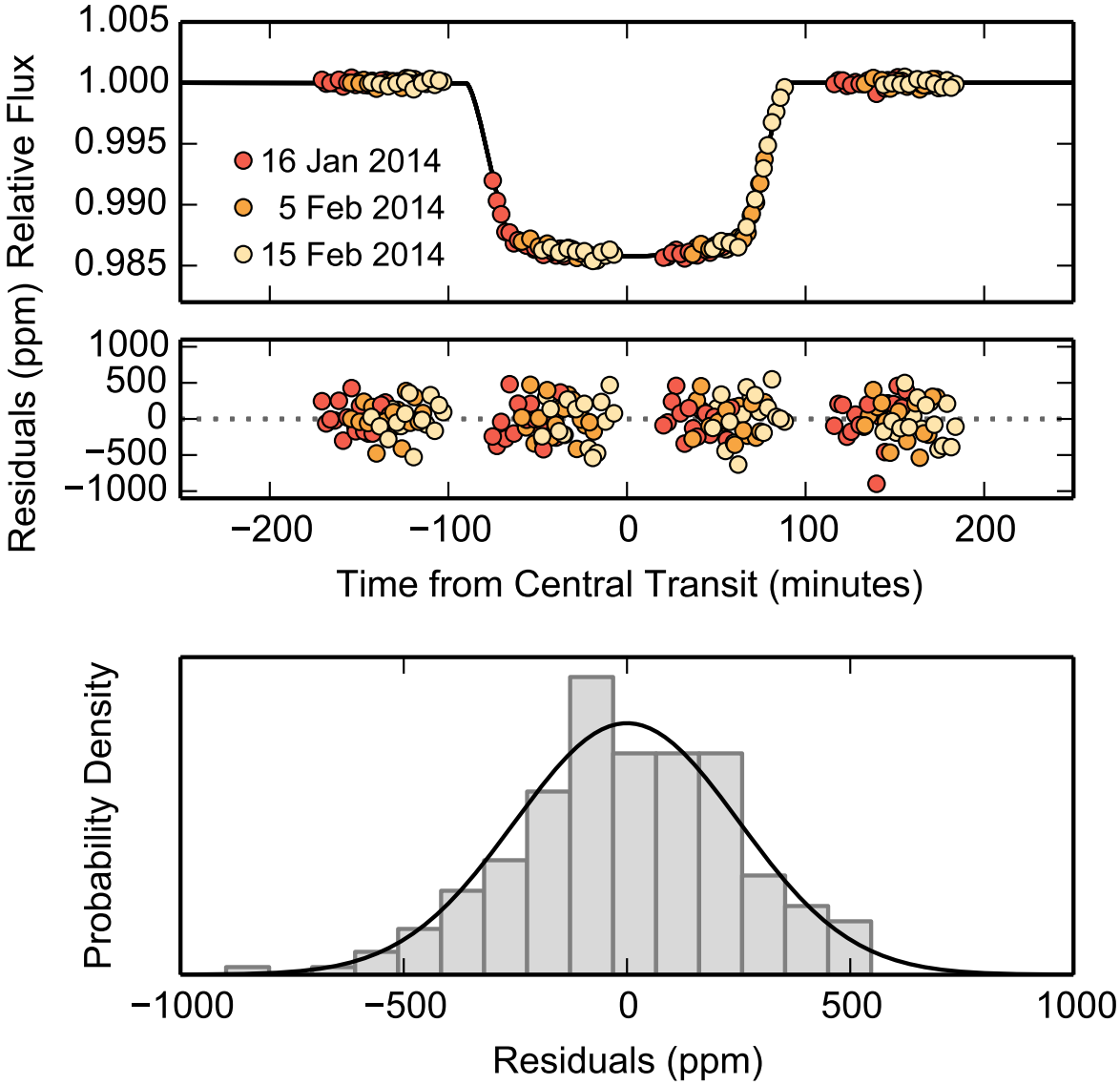

An example light curve fit to the $1.320 - 1.389$ μm spectroscopic channel from the G141 grism. The top panel shows the best fitting model light curve (black line), overlaid with the systematics-corrected data (points). Residuals from the light curve fit are shown in the middle panel. The bottom panel shows a normalized histogram of the residuals compared to a Gaussian probability density with mean zero and standard deviation equal to the predicted photon+read noise (252 ppm).

We fit the spectroscopic light curves with a similar model as we use for the broadband data. The only differences are that we hold a/R_s and i fixed to the prior mean values and fix the mid-transit times to the white light curve best fit values. We also solve for a constant rescaling parameter for the photometric uncertainties in each spectroscopic channel to ensure that the reduced χ^2 for the light curve fits is unity. We chose to fix a/R_s, i, and T_c because they impact the mean spectroscopic transit depth only, not the relative depths. Changes in the mean transit depth do not significantly affect our retrieval results, as the planet-to-star radius ratio is included as a free parameter in the atmospheric retrieval.

We fit each of the spectroscopic channel light curves independently. We achieve nearly photon-limited precision: the median rescaling factor for the photometric uncertainties is 1.1. The light curves do not exhibit statistically significant time-correlated noise, based on a Durbin-Watson test at the 1% significance level. An example spectroscopic light curve fit for the $1.320 - 1.389$ μm channel from the G141 grism is shown in Figure 4.4. We show a pairs plot of the fit parameters for the same channel in Figure 4.5.

We tested an analytic model for the systematics that included a quadratic term for the visit-long trend. Previous analyses of WFC3 data have suggested that a quadratic model produces better light curve fits (Stevenson et al., 2014d). However, for this data set we find that the quadratic model is disfavored according to the Bayesian Information Criterion (BIC), with typical Δ BIC values of 10 compared to the linear model. In any case, the main consequence of adding a quadratic term is to shift the transmission spectrum up or down. This affects our estimate of the planetary radius, but the effect is small relative to the error introduced by uncertainties in the stellar radius.

We also explored modeling the instrument systematics with the `divide-white` technique, which has been applied successfully to several other data sets (Stevenson et al., 2014c; Kreidberg et al., 2014b; Knutson et al., 2014c). This method assumes the systematics are independent of wavelength. For the WASP-12 data, however, this assumption is not appropriate. WFC3 instrument systematics are known to depend on detector illumination (Berta et al.,

2012; Swain et al., 2013), and in our data the mean pixel fluence varies by 30% between the spectroscopic channels (see Figure 3.1).

To illustrate the dependence of the systematics on the illumination level, we show in Figure 4.6 the systematics decorrelation parameters from the analytic model as a function of light curve normalization c. The value c represents the baseline flux level in each spectroscopic light curve. This value is directly proportional to the mean detector illumination in the channel. We note several qualitative trends in the decorrelation parameters: with increasing illumination, the visit-long slope decreases, the delay term increases toward zero, and the ramp rate increases.

The upshot of these trends is that there are residual systematics for the `divide-white` light curve fits that are correlated with detector illumination. We therefore only report the results for the analytic model.

Limb Darkening Models

We tested fixing the limb darkening to values predicted by stellar models. We used theoretical quadratic limb darkening coefficients from both PHOENIX and Kurucz models (Hauschildt et al., 1999; Castelli & Kurucz, 2004) generated for Stevenson et al. (2014c). These theoretical coefficients yielded lower quality light curve fits than we obtained from empirically estimating a linear limb darkening parameter. For both PHOENIX and Kurucz model coefficients, the light curve residuals exhibited systematic trends near ingress and egress, and the typical reduced chi-squared values increased. The poor match of theoretical limb darkening coefficients to our data may arise from inaccurate assumptions about the stellar composition, or inaccuracies in the models themselves. Similar disagreement with model limb darkening has been seen for other high quality data (e.g. Knutson et al., 2007a).

Since incorrect limb darkening coefficients can introduce systematic bias in the measured transit depths, we chose to estimate the limb darkening coefficients directly from the data. Our light curves are not precise enough to constrain a two-parameter limb darkening model,

so we instead fit for a single linear parameter in each channel. The data are sufficiently precise to distinguish between the transit depth and the limb darkening coefficient, as evidenced by the lack of correlation between those parameters in the pairs plot shown in Figure 4.5.

4.3.3 Correction of Dilution from Stellar Companions

The transit light curves are affected by dilution from WASP-12 A's two companion stars, WASP-12 BC, and from the planet's nightside emission. Following Stevenson et al. (2014c), we calculated a corrected transit depth δ' for each spectroscopic channel using the formula

$$\delta' = \delta(1 + \alpha_{\mathrm{Comp}} + \alpha_p) \tag{4.2}$$

where δ is the measured transit depth, α_{Comp} is the ratio of flux from WASP-12 BC to WASP-12 A, and α_p is the ratio of the planet's nightside emission to the flux of WASP-12 A. We calculated α_p using the same model as Stevenson et al. (2014c). We determined α_{Comp} empirically using the spectra extracted from the staring mode observations. Each visit is assigned a unique α_{Comp} value to account for differences in the orientation of the spectra on the detector. We plot the dilution factor as a function of wavelength in Figure 4.7 (calculated by interpolating the companion spectrum to the same wavelength scale as the WASP-12 A spectrum). The measured dilution is roughly 10% larger than the values used by Stevenson et al. (2014c); this difference could result from systematic uncertainty in the aperture photometry used to scale the dilution (Stevenson et al., 2014c).

To obtain final transit depths, we take the weighted average of the corrected transit depths from each visit. Uncertainties in the dilution factor corrections are propagated through to the final transit depth uncertainties. We report the corrected transit depth measurements in Table 4.3, and we show the transmission spectrum in Figure 4.8. The corrected transit depths are consistent between the visits, indicating that the estimated uncertainties are appropriate, and confirming that stellar activity does not significantly influence the measured spectrum.

4.4 Comparison with Previous Results

There are several other high-precision transit depth measurements for WASP-12b in addition to the WFC3 spectrum we report here. The most precise of these are spectroscopy between 0.34 and 0.94 μm from *HST*/STIS (Sing et al., 2013), spectroscopy between 0.73 and 1.00 μm from *Gemini*/GMOS (Stevenson et al., 2014c), a staring mode *HST*/WFC3 G141 spectrum from Swain et al. (2013), and photometry at 3.6 and 4.5 μm from *Spitzer*/IRAC (Cowan et al., 2012). Figure 4.9 shows past optical/near-IR transmission spectrum measurements compared to our results.

Our transit depth measurements are consistent with the staring mode spectrum from *HST*/WFC3 (Swain et al., 2013; Mandell et al., 2013; Stevenson et al., 2014c), modulo a constant offset in the absolute transit depths. We chose not to incorporate this data set in our analysis, however. The staring mode data has a low duty cycle and increases the amount of in-transit exposure time by just 10% over the total from our three spatial scan observations. Morever, there is uncertainty about the best instrument systematics model for this data set (Stevenson et al., 2014c). Since the marginal improvement in measurement precision is counteracted by increased systematic uncertainty, we chose to focus on the transmission spectrum derived from the spatial scan data only.

Our spectrum agrees less well with the ground-based transmission spectrum from *Gemini*/GMOS (Stevenson et al., 2014c). To compare the WFC3 and GMOS results, we computed χ^2 values for the data using the best fit model spectrum from the FREE retrieval (described in § 4.5.1) over the wavelength range where the spectra overlap (0.86 - 1.00 μm). We allowed a free offset in the model for the GMOS data to account for differences in the absolute measured transit depths. We find that the GMOS data are inconsistent with the model at $> 4\,\sigma$ ($\chi^2 = 38.7$ for 9 degrees of freedom). Based on the track record of precise, reproducible transmission spectra from WFC3 that are well-fit by theoretical models (e.g. Kreidberg et al., 2014b,a; Stevenson et al., 2014a), we trust the reliability of the WFC3 measurements over those from GMOS. Ground-based transit observations exhibit strong

time-correlated noise that makes estimating accurate confidence intervals challenging. Additional GMOS transit spectroscopy observations would help identify the number of repeated observations with this instrument needed to make robust measurements.

The *Spitzer* transit depths measurements are approximately 0.1% smaller than the mean WFC3 transit depth. Based on the random errors alone, this difference is significant. However, the *Spitzer* data have significant systematic uncertainties, because the relative transit depths measured with IRAC channels 1 and 2 can shift by $> 0.1\%$ depending on the aperture size used in the data reduction. There is no obvious optimal choice of aperture (see Figure 17, Stevenson et al., 2014c). We therefore chose not to incorporate the Spitzer results in our analysis.

4.5 Retrieval of the Atmospheric Properties

Given the high precision of the WFC3 transmission spectrum, we can put more powerful constraints on the planet's atmosphere than has been possible with past measurements. No previous data set for WASP-12b has shown conclusive spectroscopic evidence for molecular absorption, but the WFC3 spectrum has a noticeable increase in transit depth near the center of the water absorption band at 1.4 μm (see Figure 4.8).

To quantify the water abundance and other atmospheric properties based on the transmission spectrum, we performed a retrieval using the CHIMERA suite (Line et al., 2013b, 2014). Modifications to the retrieval code and description of the transmission forward model are provided in Line & Yung (2013a); Stevenson et al. (2014a); Kreidberg et al. (2014a); Swain et al. (2014); Diamond-Lowe et al. (2014). We tested two different model parameterizations with CHIMERA. The first is the widely adopted approach of retrieving molecular abundances without any constraints from chemistry (e.g. Madhusudhan & Seager, 2009). For our second approach, we developed a new parameterization that retrieves C/O and atmospheric metallicity under the assumption of chemical equilibrium. We refer to these methods as the FREE approach and the CHEMICALLY-CONSISTENT (C-C) approach,

Table 4.3. Transit Fit Parameters

Bandpass[a] (μm)	$(R_p/R_\star)^{2}$[b] (%)	Limb-darkening u	rms (ppm)
0.838 – 0.896	1.4441 ± 0.0069	0.27 ± 0.02	349
0.896 – 0.954	1.4422 ± 0.0055	0.28 ± 0.01	300
0.954 – 1.012	1.4402 ± 0.0052	0.27 ± 0.01	296
1.012 – 1.070	1.4428 ± 0.0051	0.26 ± 0.01	301
1.070 – 1.129	1.4391 ± 0.0053	0.25 ± 0.01	299
1.112 – 1.182	1.4386 ± 0.0047	0.26 ± 0.01	267
1.182 – 1.251	1.4365 ± 0.0045	0.26 ± 0.01	267
1.251 – 1.320	1.4327 ± 0.0041	0.21 ± 0.01	253
1.320 – 1.389	1.4582 ± 0.0040	0.22 ± 0.01	242
1.389 – 1.458	1.4600 ± 0.0043	0.18 ± 0.01	255
1.458 – 1.527	1.4530 ± 0.0045	0.20 ± 0.01	270
1.527 – 1.597	1.4475 ± 0.0058	0.16 ± 0.02	332
1.597 – 1.666	1.4332 ± 0.0055	0.16 ± 0.02	321

[a]The measurements between 0.838 - 1.129 μm are from the G102 grism; those from 1.112 - 1.666 μm are from the G141 grism.

[b]Transit depths corrected for dilution from companion stars and planet nightside emission. The light curve fits had a/R_s and i fixed to 2.91 and 80.56°, respectively.

respectively. Both methods are described in more detail below. We also present a comparison with results from the NEMESIS retrieval code (Irwin et al., 2008).

We elected to focus on the WFC3 data for our retrievals, based on the caveats for other data described in § 4.4. We treated the spectra from the two WFC3 grisms as a single data set, with no offset in transit depth between them. The transit depths are consistent between the grisms because the influence of stellar activity is below the measurement precision (see § 4.2.1), so no offset is needed. We also tested including STIS data in some of the retrievals (see § 4.5.1), but found that it does not affect the main conclusions of this work.

4.5.1 FREE Retrieval with CHIMERA

The FREE parameterization retrieves molecular abundances, cloud and haze properties, and the altitude-independent scale height temperature.

Our model explored the dominant molecular opacities expected for a solar composition gas at the temperatures and pressures probed by the observations. These are H_2O, TiO, Na, and K over the wavelength range of the WFC3 spectrum (Burrows & Sharp, 1999; Fortney et al., 2008). The remaining gas is assumed to be a solar composition mixture of H_2 and He. We discuss results for including additional molecular species in § 4.5.1.

In addition to the molecular opacities, we included opacity from clouds and haze. Previous analyses of WASP-12b's transmission spectrum have suggested that hazes are present in the atmosphere, but the haze composition is poorly constrained (Sing et al., 2013; Stevenson et al., 2014c). We therefore used a flexible model that includes a power law haze and an opaque gray cloud deck. We modeled clouds as a gray opacity source that masks transmission through the atmosphere below a fixed pressure level P_c. The haze opacity was parameterized by $\sigma(\lambda) = \sigma_0(\lambda/\lambda_0)^\gamma$, where the scattering amplitude σ_0 and slope γ are free parameters (as in Lecavelier Des Etangs et al., 2008). The scattering is presumed to happen throughout the entire atmosphere as if it were a well mixed gas. The scattering amplitude is a scaling to the H_2 Rayleigh scattering cross section times the solar H_2 abundance at 0.43 μm. More

sophisticated models for clouds and haze would require additional free parameters that are not justified by the precision of our data. Our simple parameterization is sufficient to capture degeneracies between clouds/haze and the water abundance, which is the primary goal of this investigation.

We also retrieved a "scale height temperature" parameter T_s. We assumed the atmosphere is isothermal, with temperature equal to T_s at all pressures. We tested fitting for a more complex temperature-pressure profile but found it did not affect our results because the transmission spectrum is only weakly sensitive to the atmosphere's thermal structure (see Barstow et al., 2013, 2014).

The final free parameter in the retrieval was a scale factor for the planet's 10 bar radius. We assumed a baseline planet radius of 1.79 $R_{\rm J}$ and a stellar radius of 1.57 $R_{\odot}$ from Hebb et al. (2009). The planet radius was scaled by a factor $R_{\rm scale}$ to account for uncertainty in the pressure level in the atmosphere at a given radius. To first order, the effect of this scaling is to shift the model transit depths by a constant factor. A second order effect is that scaling the radius changes the amplitude of spectral features (see Equation 1 in Lecavelier Des Etangs et al., 2008).

In sum, the retrieval had 8 free parameters: the abundances of H_2O, Na+K (fixed at the solar abundance ratio), and TiO, as well as clouds and haze, the scale height temperature, and the planet radius scale factor. We refer to this 8-parameter fit as the FULL model. The best fits for the FULL model and nested models within it are shown in Figure 4.10. The best-fit models are those that produced the lowest χ^2 values in the MCMC. We list the retrieved water abundances, temperatures, and best fit χ^2 values for these models in Table 4.4. The distributions of retrieved parameters from the FULL model are shown in Figure 4.11. We note that all of the nested models are nearly indistinguishable near the water absorption feature at 1.4 μm. The best constrained molecular abundance is that of water: we retrieved a water volume mixing ratio (VMR) of $1.6 \times 10^{-4} - 2.0 \times 10^{-2}$ at $1\,\sigma$, which is consistent with expectations for a solar composition gas. The other molecular

abundances are not as well constrained. We retrieved a $3\,\sigma$ upper limit on the VMR of TiO equal to 2×10^{-4}, and the abundance of Na+K is unbounded. The cloud and haze properties are also poorly constrained. We discuss the implications of these measurements for the atmosphere composition in detail in § 4.6.

Detection Significances

We performed nested model selection to identify how strongly each opacity source is detected in the spectrum. The standard Bayesian approach for comparing models is to use Bayes factors, which can be converted to detection significances (Sellke et al., 2001; Trotta, 2008). See also Benneke & Seager (2013) for an application of nested Bayesian model comparisons as applied to super-Earth atmospheres. Bayes factors are the ratio of the Bayesian evidence (marginal likelihood) of the two models under consideration. The evidence is a multidimensional integral over the entire posterior volume, a non-trivial calculation, so here we use two methods to approximate the integral. The first is the Numerical Lebesgue Algorithm described in Weinberg (2012) (see also Swain et al., 2014, for an application to exoplanet atmospheres and a comparison to the $\Delta\chi^2$ test). The second is the Laplace approximation (Kass & Raftery, 1995; Cornish & Littenberg, 2007). Most methods for computing Bayesian evidence diverge for low detection significances, but they agree well for highly significant detections (see Fig. 3 from Cornish & Littenberg, 2007).

Using these techniques, we determined the detection significances for the following parameter combinations: H_2O, absorbers other than H_2O, clouds and haze combined, clouds only, haze only, and all opacity sources other than H_2O. We computed the detection significance for each nested model by calculating its Bayes factor relative to the FULL model. The results are shown in Table 4.4. If a parameter has a low detection significance value ($\lessapprox 3\,\sigma$), that parameter does not provide a statistically significant improvement to the model fit.

We find that H_2O is detected at high confidence in the spectrum ($7\,\sigma$). We also find that the presence of all other opacity sources combined (clouds, haze, TiO, Na and K)

Table 4.4. FREE Retrieval Results

Scenario[a]	Water abundance[b] (VMR)	Temperature[b] (Kelvin)	χ^{2c}	Weinberg significance[d] (σ)
FULL (T_s, $R_{\rm scale}$, P_c, H_2O, TiO, Na+K, σ_0, γ)	$1.5 \times 10^{-4} - 2.2 \times 10^{-2}$	$1040 - 1870$	2.82	–
No water (T_s, $R_{\rm scale}$, P_c, TiO, Na+K, σ_0, γ)	–	$130 - 1560$	47.0	6.9
No cloud, haze, other absorbers (T_s, $R_{\rm scale}$, H_2O)	$1.1 \times 10^{-5} - 1.5 \times 10^{-2}$	$730 - 1170$	11.1	3.2
No other absorbers (T_s, $R_{\rm scale}$, P_c, H_2O, σ_0, γ)	$6.9 \times 10^{-5} - 2.9 \times 10^{-2}$	$1090 - 1890$	3.59	1.2
No haze (T_s, $R_{\rm scale}$, P_c, H_2O, TiO, Na+K)	$5.8 \times 10^{-5} - 8.3 \times 10^{-3}$	$910 - 1470$	2.87	1.6
No cloud (T_s, $R_{\rm scale}$, H_2O, TiO, Na+K, σ_0, γ)	$6.6 \times 10^{-5} - 2.0 \times 10^{-4}$	$1000 - 1840$	2.86	–
No cloud/haze (T_s, $R_{\rm scale}$, H_2O, TiO, Na+K)	$2.4 \times 10^{-5} - 5.5 \times 10^{-3}$	$860 - 1430$	2.95	–

[a]Indicates the parameters that are removed from the FULL model. The remaining parameters are shown in parentheses.

[b]The range of values corresponds to the 68% credible interval centered on the median retrieved value.

[c]χ^2 values are calculated for the best fit model.

[d]Scenarios where the detection significance is undefined (because the Bayes factor is less than 1) are marked by –. The detection significance for the FULL model is also undefined because significances are defined relative to it.

is significant at $> 3\,\sigma$. However, no other combination of these opacities is significantly detected (e.g., the detection significance for clouds alone is $< 2\,\sigma$). The reason for this is that the parameters are degenerate. For example, both clouds and haze both have the effect of truncating the height of the water feature. Similiarly, haze, the wings of the alkali metal lines, and presence of TiO can all contribute to the rise in transit depths towards the blue end of the spectrum. Therefore, if a few of these opacity sources are removed, the others can compensate. However, removing all opacities besides water results in a significantly poorer model fit (as can be seen in Figure 4.10). We therefore focus on results from the FULL model because it accounts for the likely presence of some combination of these other species and the degeneracies they may have with H_2O.

Retrievals with Additional Molecules/Data

We explored many different combinations of models and data sets before we arrived at the analysis presented above. One option we considered was to fit a WFC3 spectrum with smaller wavelength bins. We created a "high-resolution" spectrum with $R = 55 - 70$, in contrast to the "low-resolution" data ($R = 15 - 25$) we used for our final modeling. The spectra are qualitatively similar, but the models fit the low-resolution data better ($\chi^2_\nu = 0.6$ versus

1.5). The high-resolution spectrum has larger random scatter around the best fit model, but no systematic trends indicating that the model is missing a particular physical effect. The scatter could be due to undiagnosed systematics at the pixel level in the data, which is remedied by increasing the number of pixels that contribute to each spectral channel.

The retrieved water abundances for both resolutions are very similar ($1.5 \times 10^{-4} - 2.2 \times 10^{-2}$ and $1.2 \times 10^{-4} - 1.8 \times 10^{-2}$ for low- and high-resolution). On the other hand, the best fit scale height temperatures differ by $1.4\,\sigma$ (1370^{+470}_{-340} versus 2020^{+320}_{-340} for low/high). This difference is due to slight changes in the morphology of the water feature between the data sets. It illustrates how retrieval results can be biased or have underestimated uncertainties when the model does not provide a good fit to the data, either because of missing model physics or underestimated data error bars.

Another test we performed was to fit the combined transmission spectrum from *HST*/STIS and WFC3. The STIS spectrum covers optical wavelengths and exhibits a linear increase in transit depth from red to blue (see Figure 4.9). Incorporating the STIS data in the retrieval increased the detection significance of clouds and haze to $> 3\,\sigma$ (because of the rise in transit depth towards the blue), but otherwise did not significantly change the results.

We also tested including additional absorbing species in the retrieval. Previous work has suggested WASP-12b has a carbon-rich atmosphere composition (e.g. Madhusudhan et al., 2011c), so we wanted to confirm that our estimate of the water abundance is not biased by only including absorbers expected for solar composition. We therefore ran a retrieval including all the major opacity sources expected for either oxygen-rich or carbon-rich compositions, including H_2O, CO, CO_2, NH_3, TiO, VO, Na, K, CH_4, C_2H_2, HCN, H_2S, FeH, N_2, and collisionally-induced H_2/He absorption (Burrows & Sharp, 1999; Fortney et al., 2008; Madhusudhan, 2012). For this retrieval, we also fit the STIS data and used the higher-resolution WFC3 spectrum. The retrieved water abundance of $2.5 \times 10^{-4} - 2.0 \times 10^{-2}$ is nearly identical to the results we obtained from the FULL model. No individual absorbers were significantly detected besides H_2O.

Our conclusion from all the scenarios we fit is that the constraints on the water abundance are not significantly impacted by the choice of data sets or the absorbers included in the modeling.

4.5.2 CHEMICALLY-CONSISTENT Retrieval with CHIMERA

In addition to retrievals with the FREE parameterization (described in § 4.5.1), we also developed a reparameterized model to retrieve atmospheric properties that are consistent with chemical equilibrium. Rather than varying the mixing ratios of individual gases, we made C/O and metallicity free parameters and computed thermochemical equilibrium abundances along the temperature/pressure (T/P) profile for major species. We retrieved the T/P profile rather than a scale height temperature in order to explore any additional degeneracies due to the profile shape. The T/P profile is modeled with a 5-parameter analytic function (Line et al., 2013b) which produces physically realistic thermal profiles consistent with radiative equilibrium (e.g. Guillot, 2010; Robinson & Catling, 2012; Heng et al., 2012; Parmentier & Guillot, 2014). We calculated chemical profiles for H_2, He, H_2O, CH_4, CO, CO_2, NH_3, H_2S, PH_3, C_2H_2, HCN, Na, K, FeH, TiO, VO, and N_2 to cover the full range of gases that could contribute significant opacity in the near-IR. The equilibrium abundances are computed using the NASA Chemical Equilibrium with Applications code (McBride & Gordon, 1996; Moses et al., 2011; Line et al., 2011). The chemical profiles were fed into the radiative transfer model to calculate model transmission spectra for comparison with our data. The model also included opacity from clouds and haze (using the same formalism described in § 4.5.1), and the reference radius R_p, for a total of 11 free parameters. While we reduced the number of free absorber parameters to just C/O and metallicity, the overall number of free parameters increased due to the more flexible T/P profile.

We ran retrievals using three different priors for C/O. The fiducial case had an uninformative prior constraint on C/O. We also ran retrievals that constrained the atmospheric composition to be either oxygen-rich or carbon-rich. For the O-rich scenario, the prior proba-

Table 4.5. C-C Retrieval Results

Scenario	C/O	Metallicity ($\times$ solar) ($1\,\sigma$)	Water abundance ($1\,\sigma$)	Temperature[a](K) ($1\,\sigma$)	χ^2
Fiducial	$0.2-0.7$	$0.3-20$	9.3×10^{-5} - 5.3×10^{-3}	$1090-1760$	2.43
O-rich	$0.1-0.7$	$0.3-30$	1.2×10^{-4} - 1.5×10^{-2}	$1090-1890$	2.75
C-rich	$2.9-51$	$0.2-80$	1.5×10^{-5} - 8.6×10^{-3}	$120-550$	29.2

[a]The temperature range corresponds to a pressure level of 1 mbar.

bility was set to zero for C/O values greater than unity. Correspondingly, the C-rich scenario had zero prior probability for C/O < 1. We show the best fit models for all three cases in Figure 4.10. Figure 4.12 shows marginalized distributions of C/O and metallicity for each scenario, as well as constraints on the temperature-pressure profiles. Table 4.5 gives the χ^2 values of the best fits in each scenario. It also lists the 68% credible intervals for C/O, metallicity, and the temperature and water abundance at 1 mbar pressure.

The fiducial and oxygen-rich scenarios give nearly identical constraints on C/O and the atmospheric metallicity. Even though the fiducial model has an uninformative prior on C/O, 100% of the retrieved C/O values are less than unity for this case (suggesting the result is data-driven rather than prior-driven). Both scenarios yield constraints on the molecular abundances and thermal profile that agree well with results from the FULL model. The median retrieved water abundances are 6.3×10^{-4} and 1.0×10^{-3} for the fiducial and O-rich scenarios, respectively. The median 1 mbar temperatures are 1410 and 1450 K. We retrieved metallicities in the range $0.3-30\times$ solar (at $1\,\sigma$). The retrieved cloud and haze properties for these scenarios are consistent with the FULL model at $1\,\sigma$.

By contrast, the carbon-rich scenario produced significantly different atmospheric properties. To reproduce the water absorption feature in the spectrum, the temperature was driven to much lower values (the median is 320 K at 1 mbar). These low temperatures allow for higher water abundances (see Figure 4.13), though they are unlikely for the terminator

region given how highly irradiated the planet is. The median water abundance, 1.4×10^{-4}, is comparable to that for the O-rich and fiducial scenarios. On the other hand, the median methane abundance increases to 2.4×10^{-3}, versus 1.3×10^{-11} for the fiducial case. These differences have two main effects on the model transmission spectra. One is that absorption features have smaller amplitude because lower temperatures decrease the atmospheric scale height. The second effect is that methane absorption is present in the spectrum. It is especially noticeable in the window between water features at $> 1.6\,\mu$m wavelengths (see the best-fit C-rich model in Figure 4.10). The consequence of these changes is that C-rich models do not fit the measured spectrum as well as O-rich models. We discuss the strength of the evidence for one scenario over the other in quantitative detail in § 4.6.

As a test, we also considered a scenario with clouds and haze removed. We computed the Bayes factor for this nested model and found a detection significance of $3.7\,\sigma$ for the cloud and haze parameters. The detection significance is higher than for the FREE model parameterization because the assumption of chemical equilibrium breaks the degeneracy between the cloud/haze and the other molecular abundances (Na+K, TiO); i.e. the other molecular abundances can't increase arbitrarily to make up for the absence of clouds/haze.

4.5.3 Retrieval with NEMESIS

We also compared the results from CHIMERA with output from an independent retrievel code to test the robustness of our measurements against a different modeling approach (optimal estimation versus MCMC). We fit the high-resolution WFC3 spectrum with the NEMESIS code (Irwin et al., 2008). The model included H_2O as the only molecular opacity source. We modeled the atmosphere's thermal structure as a scalar multiple of the dayside temperature-pressure profile from Stevenson et al. (2014b). NEMESIS does not currently incorporate cloud-top pressure as a free parameter, so we fixed the altitude of an opaque gray cloud deck over a grid of pressures ranging from 10 to 10^{-3} mbar and retrieved the atmospheric properties for each case (for further discussion of retrieving cloud properties

with NEMESIS, see Barstow et al., 2013). The best fit model had a cloud deck at 1 mbar and a retrieved water abundance of $4.0 \times 10^{-4} - 1.7 \times 10^{-3}$ at $1\,\sigma$. Models with higher altitude cloud decks (0.1 - 0.001 mbar) achieved nearly as good a fit, and had 1 σ upper bounds on the water abundance of 3×10^{-2}. These results are in excellent agreement with the results from CHIMERA.

4.6 Implications for Atmospheric C/O

In this section, we quantify the strength of the evidence for oxygen-rich compositions (C/O $<$ 1) over carbon-rich compositions (C/O $>$ 1) based on our retrieval results from two separate modeling approaches. We focus first on constraints from the water abundance from the FREE retrieval, since water is the only molecule that is unambiguously detected in the spectrum. We then discuss constraints from the C-C model, which retrieves C/O directly under the assumption of chemical equilibrium.

4.6.1 Constraints from the FREE Retrieval

Broadly speaking, a carbon-rich atmosphere is expected to have lower water abundance than an oxygen-rich atmosphere, because most of the oxygen atoms are bound in CO in chemical equilibrium at high temperatures (Madhusudhan et al., 2011a). Our water abundance measurement is a qualitatively better match to predictions for an oxygen-rich composition. In Figure 4.13, we show the retrieved H_2O abundance for the FULL retrieval and nested models in comparison with thermochemical equilibrium predictions for oxygen-rich (C/O = 0.55 = solar) and carbon-rich (C/O = 1) atmospheres. The predicted abundance depends on pressure and temperature, so we plot the span of predictions over pressures from 0.1 to 10 mbar as a function of temperature.

To quantitatively compare our measurement to the models, we must marginalize over the uncertainty in the pressure and temperature probed by the observations. To do this, we

compute an equivalent pressure level p_{eq} corresponding to an optical depth $\tau = 0.56$ at 1.4 μm at each step in the MCMC chain. This quantity is representative of the typical pressure level at which photons are absorbed by water molecules (Lecavelier Des Etangs et al., 2008). Figure 4.14 shows the distribution of equivalent pressures from the MCMC chain. Note that p_{eq} is not a retrieved quantity, but rather derived from the opacities at each MCMC step. We show the distribution of equivalent pressures obtained from this method in Figure 4.14. The pressures have a $1\,\sigma$ range of 0.05 to 5 mbar, with a peak at 0.5 mbar.

For a specified atmospheric composition, we can then calculate the predicted equilibrium H_2O abundance for a temperature and pressure equal to T_s and p_{eq}. This procedure yields a "calculated" water abundance to compare with the "observed" water abundance at each step in the MCMC chain. We show the distribution of observed minus calculated ("O - C") values for the oxygen-rich and carbon-rich models in Figure 4.13 (right panel).

To test how well each model agrees with the retrieved H_2O abundance, we assess whether the O-C distribution is consistent with zero. For the oxygen-rich model, zero is contained in the $1\,\sigma$ credible interval centered on the median, indicating that this model is a good match. By contrast, the O-C distribution for the carbon-rich model is in tension with zero at approximately 2σ (the 95% credible interval is $0.1 - 6.4$). The median O-C value is 3.7, implying that the typical retrieved water abundances are nearly four orders of magnitude larger than predicted for a carbon-rich composition.

We emphasize that these results are strongly dependent on the temperature and pressure probed by the observations. Assuming a different local thermal profile can result in order-of-magnitude differences in the predicted abundances (cf. Figure 2, Madhusudhan, 2012). It is therefore essential to account for the temperature and pressure (and their uncertainties) when estimating C/O.

4.6.2 Constraints from the C-C Retrieval

We obtain more stringent constraints on the atmospheric C/O from the C-C retrieval than from the FREE parameterization. By every metric we enumerate below, C/O values greater than one are ruled out at high confidence. First, the entire posterior probability distribution for C/O from the fiducial model is less than one. We calculate that there are roughly 3000 independent samples in the MCMC chain for that model, which is a sufficient number to rule out C/O$>$ 1 at greater than $3\,\sigma$ confidence. Second, the χ^2 values for the best fit models provide additional evidence in favor of the O-rich scenario. The best fit O-rich model has $\chi^2 = 2.75$ versus $\chi^2 = 29.2$ for the best fit C-rich case (for 2 degrees of freedom). This difference in χ^2 implies the O-rich model is 10^6 times more likely than the best fit C-rich model, assuming Gaussian statistics. Third, the Bayes factor (the ratio of integrated posterior probabilities) for the C-rich scenario to the O-rich scenario is 14, which constitutes strong evidence in favor of the O-rich model (Jeffreys, 1998). In addition, the fact that the temperature range drops unphysically low – below the condensation temperature of water – is further evidence that the carbon-rich model is not appropriate for these data.

Taken together, these results rule out a carbon-rich composition for the atmosphere at high confidence. This is a more definitive constraint than what we obtained from studying the water abundance alone because the model is sensitive to both the presence of water *and* the absence of absorption features from other molecules. For example, the fact that no methane features are detected in the spectrum strengthens the case for an O-rich composition beyond the constraints from the presence of water alone. The C-C model also assumes more prior knowledge by imposing chemical equilibrium in the calculation of the model spectra.

4.7 Summary & Conclusions

We have measured a precise transmission spectrum for the hot Jupiter WASP-12b over the wavelength range 0.84 to 1.67 μm with *HST*/WFC3. The transmission spectrum is a factor

of three more precise than previous measurements in this wavelength range (Swain et al., 2013). We retrieved the atmospheric properties based on this spectrum with a variety of models, including a new retrieval parameterization that fits for C/O and metallicity rather than molecular abundances. Our conclusions about the nature of the planet are summarized as follows:

1. Water is present in the atmosphere. Models that do not include water absorption are excluded at $7\,\sigma$ confidence. This result is the first unambiguous spectroscopic detection of a molecule in the planet's atmosphere.

2. The 68% credible interval for the retrieved water abundance is $10^{-5} - 10^{-2}$ for a wide range of models. This result applies to scenarios where water is the only absorber included in the model, where clouds and haze are added, where additional absorbers are incorporated (CO, CO_2, NH_3, TiO, VO, Na, K, CH_4, C_2H_2, HCN, H_2S, FeH, and N_2), and where optical transit depth measurements from *HST*/STIS are also fit. This range agrees well with the predicted equilibrium water abundance for a solar composition atmosphere but is still consistent to within 2σ with the prediction for a carbon-rich composition.

3. Stellar photons are absorbed at temperatures of $1000 - 1900$ Kelvin and pressures of $0.1 - 10$ mbar (based on $1\,\sigma$ ranges for T_s and $P_{\rm eq}$ from the FULL model). These estimates have large uncertainties because the transmission spectrum is only weakly sensitive to the thermal structure of the atmosphere.

4. Based on a new retrieval parameterization that fits for C/O and metallicity under the assumption of chemical equilibrium, we constrain the C/O to $0.5^{+0.2}_{-0.3}$ at $1\,\sigma$ and rule out a carbon-rich atmosphere composition (C/O > 1) at $> 3\,\sigma$ confidence. With this model, we also detect the presence of clouds/haze at 3.7 σ confidence.

Our constraint on C/O is in tension with past studies of the planet's atmosphere that found a carbon-rich composition was the best explanation for the dayside emission spec-

trum (e.g. Madhusudhan et al., 2011c; Stevenson et al., 2014b). We would hope for better agreement between these analyses, as both results are based on very high precision data fit with state-of-the-art retrieval models. This methodology has yielded consistent results for other planets, notably the hot Jupiter WASP-43b, which shows excellent agreement between estimates of the composition from the dayside emission and transmission spectra (Kreidberg et al., 2014a).

We note that a caveat for our results from the C-C model is our assumption that the atmosphere is in chemical equilibrium. Moses et al. (2013) considered the effects of photochemistry and mixing for WASP-12b and found that the water abundance is either unchanged from equilibrium values (for solar composition), or pushed even lower (for a C/O = 1 composition). Based on these results, it is unlikely that our high observed water abundance is due to disequilibrium chemistry in a carbon-rich atmosphere. However, these calculations were for the planet's dayside and it would be worth exploring disequilibrium effects for the terminator region specifically in future work.

Another assumption in our model is that the temperature structure is well approximated as 1D. In reality, a photon's slant path through the atmosphere traverses many different temperatures and pressures. However, theoretical models predict that most of the stellar radiation is attenuated in a fairly localized region within a few degrees of the terminator (Fortney et al., 2010). The change in temperature and pressure over a region this size is small compared to the uncertainty in our estimates of the thermal profile, so our assumption of a 1D profile is unlikely to bias our assessment of the atmospheric composition. On the other hand, the observations integrate over the entire limb of the planet, and there could be large variations in temperature over this region due to atmospheric dynamics. It is therefore possible that fitting the limb-averaged spectrum with a single 1D thermal profile could bias the results.

One route to reconciling the disagreement between constraints on C/O from the transmission and emission spectra is to determine the planet's global thermal structure. This

could be achieved by combining phase-resolved emission spectroscopy of the planet with 3D atmospheric circulation modeling, as has been done for WASP-43b (Stevenson et al., 2014a; Kataria et al., 2014b). This combination would provide an independent measure of the temperature structure at the terminator to strengthen our interpretation of the transmission spectrum. It would also put the dayside temperature-pressure profile in context of the planet's global heat circulation and aid in understanding the dayside emission spectrum. In addition, a spectroscopic phase curve would allow us to estimate the water abundance for new regions of the planet's atmosphere. Furthermore, the spectroscopic phase curve amplitudes themselves could provide an additional diagnostic of the atmosphere composition. Day-night temperature differences for hot Jupiters are larger at lower pressures (Showman et al., 2009; Stevenson et al., 2014a; Kataria et al., 2014a,b), so light curves in absorption bands (which probe lower pressures) are expected to have larger amplitudes than those in spectral windows. Measuring the wavelength dependence of the phase curve amplitude could therefore provide an additional constraint on the atmospheric composition (Showman et al., 2009; Stevenson et al., 2014a; Kataria et al., 2014a,b).

Finally, our results highlight the necessity of obtaining high-precision data with multiple observing techniques (transmission spectroscopy, dayside emission spectroscopy, and phase curves) in order to obtain robust constraints on the rich chemistry and physics of exoplanet atmospheres. Studying the atmosphere from more than one angle (literally) is key to providing a detailed understanding of its thermal structure and dynamics, which is needed to unambiguously determine the composition (and vice versa). In addition, high-precision measurements are essential for revealing the small features present in exoplanet spectra. The amplitude of these features has often been smaller than predicted for transiting planets, due to the presence of clouds or haze and shallower thermal profiles (e.g. Fortney et al., 2006; Charbonneau et al., 2002; Deming et al., 2013). Our WASP-12b spectrum is a new example of this for transmission measurements, with features crossing just two scale heights. We therefore advocate applying an intensive approach of high-precision spectroscopy from

multiple angles to a larger sample of transiting exoplanets to shed light on their nature and origins. Such measurements will help develop the observing strategies needed for definitive characterization of exoplanet atmospheres, and prepare the community to make robust measurements of potentially habitable worlds with future facilities.

Figure 4.5: Pairs Plot for MCMC Fit to Light Curve

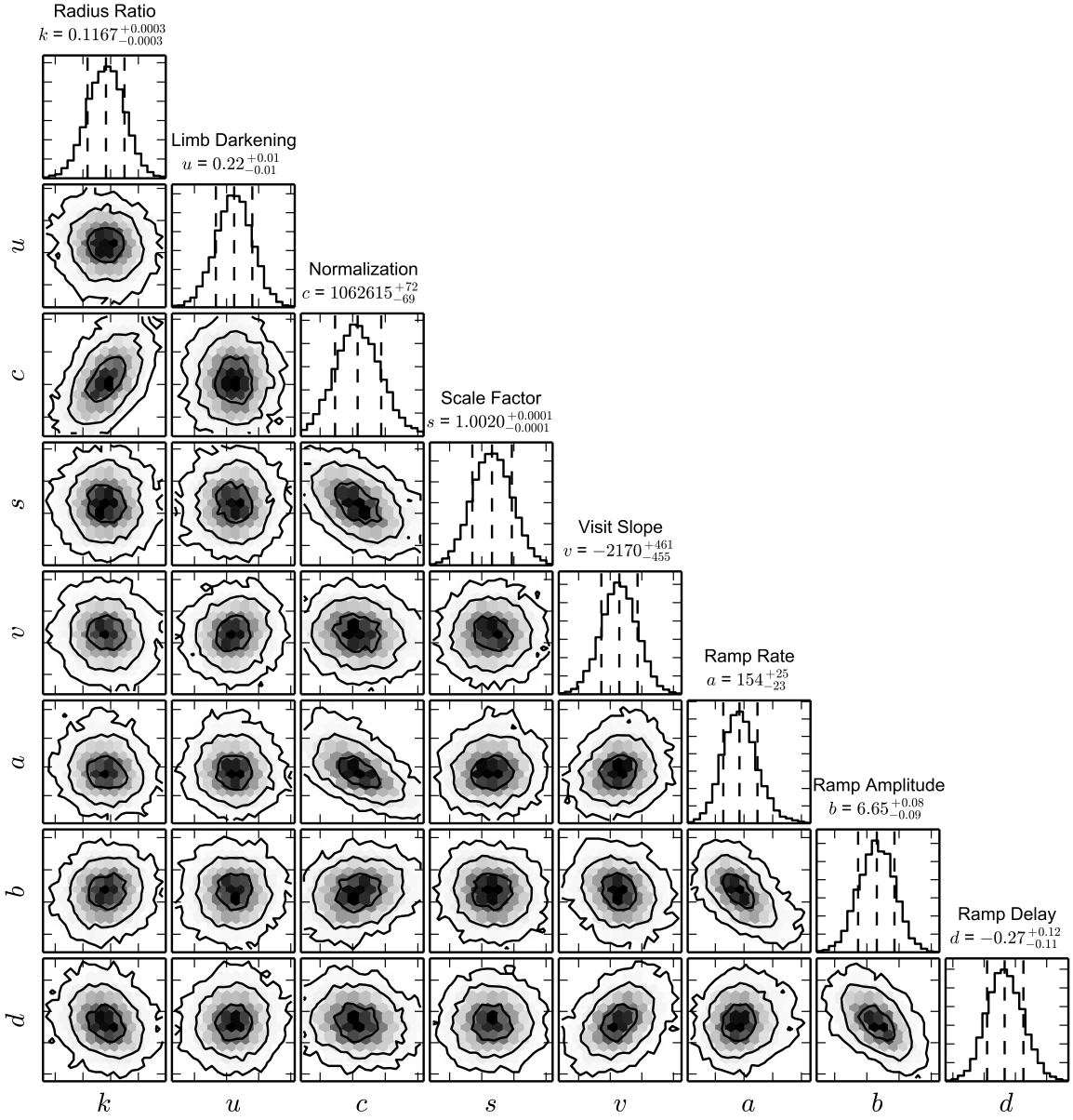

A pairs plot showing distributions of MCMC fit parameters for the $1.320 - 1.389$ μm light curve. The off-diagonal panels show marginalized posterior probability for pairs of parameters, with 1, 2, and $3\,\sigma$ credible intervals indicated with black contours. The gray shading corresponds to probability density (darker for higher probability). The panels on the diagonal show distributions of each parameter marginalized over the other model parameters, with the median and 68% credible interval marked with dashed lines. The planet-to-star radius ratio, k, is not strongly correlated with any of the other fit parameters. For parameters that are allowed to vary between transit observations (k, c, s, and v), we show distributions for the 16 Jan 2014 transit.

Figure 4.6: Trends in Systematics Decorrelation Parameters with Detector Illumination

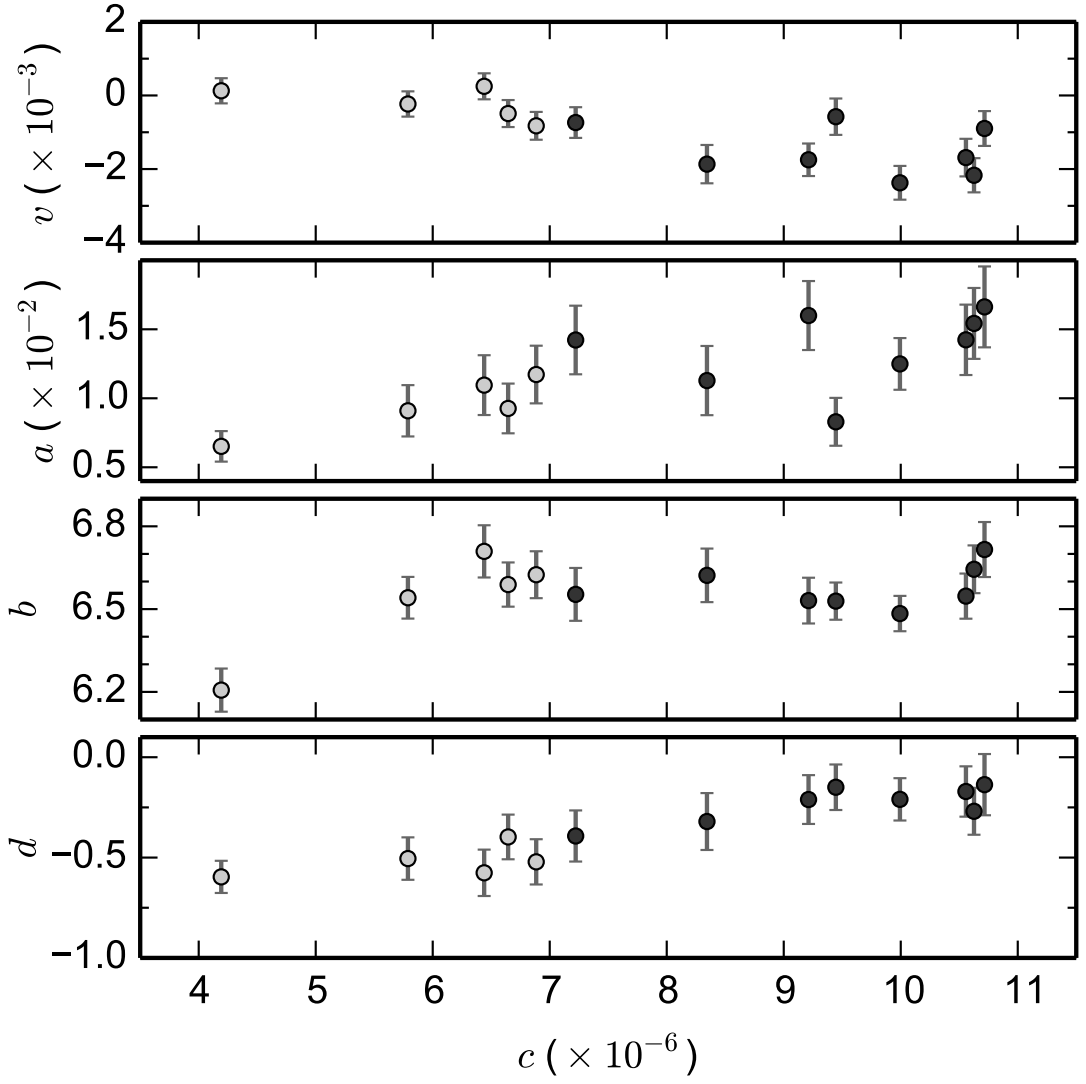

Systematics decorrelation parameters from the light curve fits plotted as a function of normalization c, which is a proxy for detector illumination. We show (from top to bottom) the visit-long slope v, ramp rate constant a, ramp amplitude b, and ramp delay d. The normalization constant c is linearly proportional to the per-pixel flux in a spectroscopic channel. Measurements from the G102 and G141 data are shown in light and dark gray, respectively. The error bars indicate $1\,\sigma$ uncertainties from an MCMC fit to the light curves using the analytic model for instrument systematics.

Figure 4.7: Dilution from Companion Star

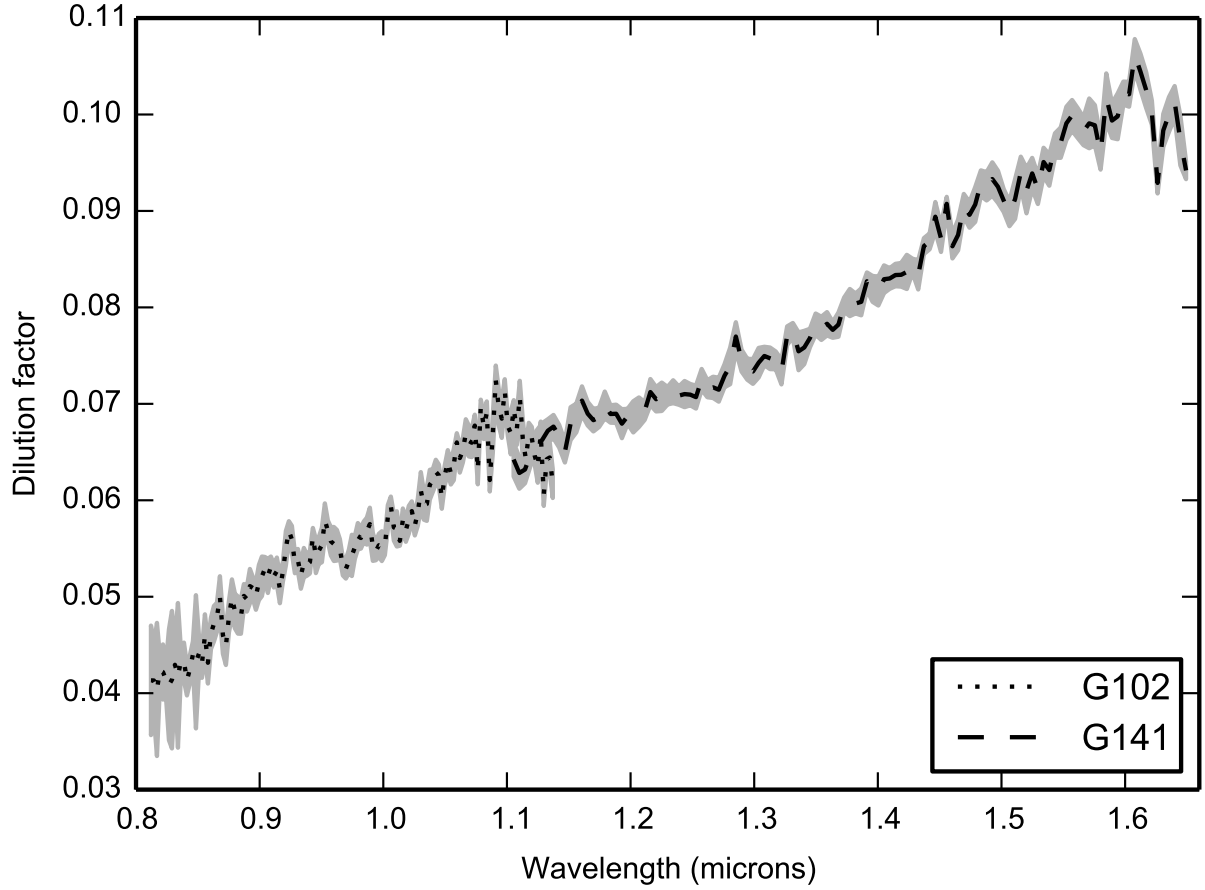

The dilution factor $\alpha_{\rm Comp}$, determined from the ratio of flux from WASP-12 BC to WASP-12 A. The median dilution (over the 10 staring mode observations) is shown with black lines (dotted for G102 and dashed for G141). The gray shaded region indicates 1σ uncertainty, determined from the median absolute deviation. To calculate the dilution and uncertainty, we interpolate the spectra from each grism onto a common wavelength scale.

Figure 4.8: WASP-12b Transmission Spectrum

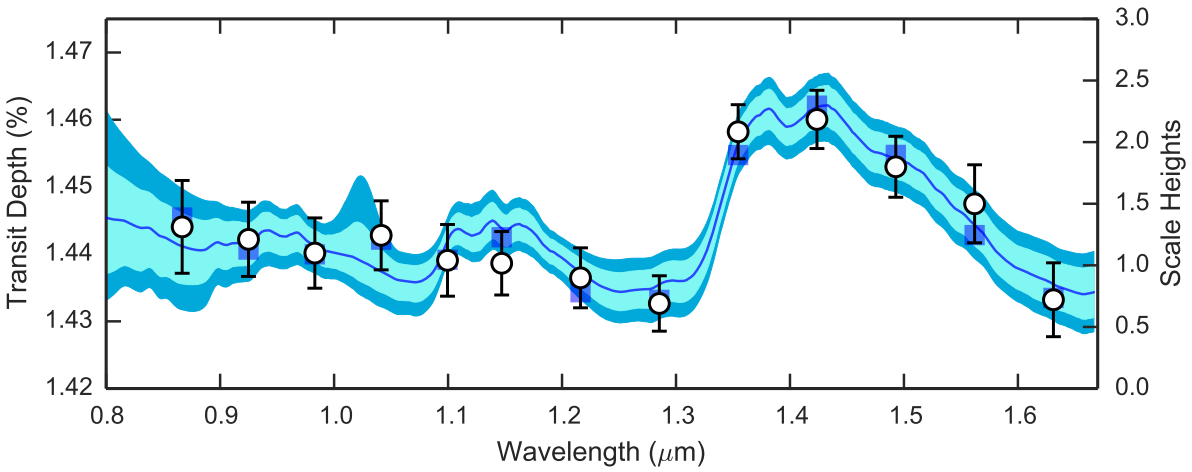

The transmission spectrum of WASP-12b measured with *HST*/WFC3 (points). The error bars on the transit depths are $1\,\sigma$ uncertainties from an MCMC fit to the light curves. We show the best fit model binned to the resolution of the data (blue squares). The shaded regions indicate 1- and $2\,\sigma$ credible intervals in the retrieved spectrum (medium and light blue, respectively), relative to the median fit (dark blue line). The secondary y-axis labels indicate the atmospheric scale height. One scale height corresponds to 470 km (for a temperature of 1400 K). The increase in transit depth near $1.4\,\mu$m corresponds to an H_2O bandhead.

Figure 4.9: Comparison with Previous Transmission Spectra Measurements

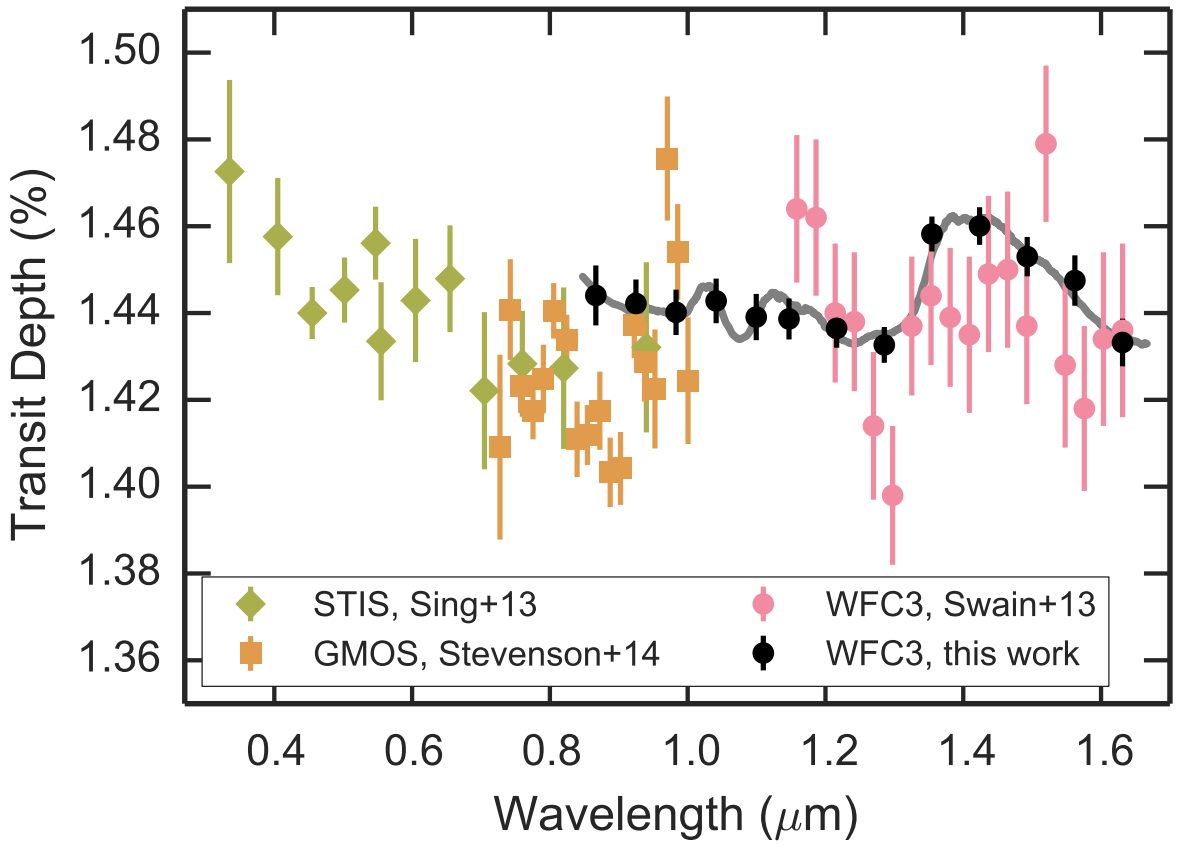

High-precision optical/near-IR transit depth measurements for WASP-12b. We show measurements from *HST*/STIS (green diamonds), *Gemini*/GMOS (orange squares), and *HST*/WFC3 (from this work, black circles; from staring mode data, pink circles). The best fit model from the CHIMERA FULL retrieval is indicated by the gray line. Note that this model was fit to the WFC3 data only. There may be small offsets between data sets due to different corrections for the companion star dilution and the challenge of measuring absolute transit depths in the presence of systematic errors (Stevenson et al., 2014c,d).

Figure 4.10: Best Fit Models from Spectral Retrieval

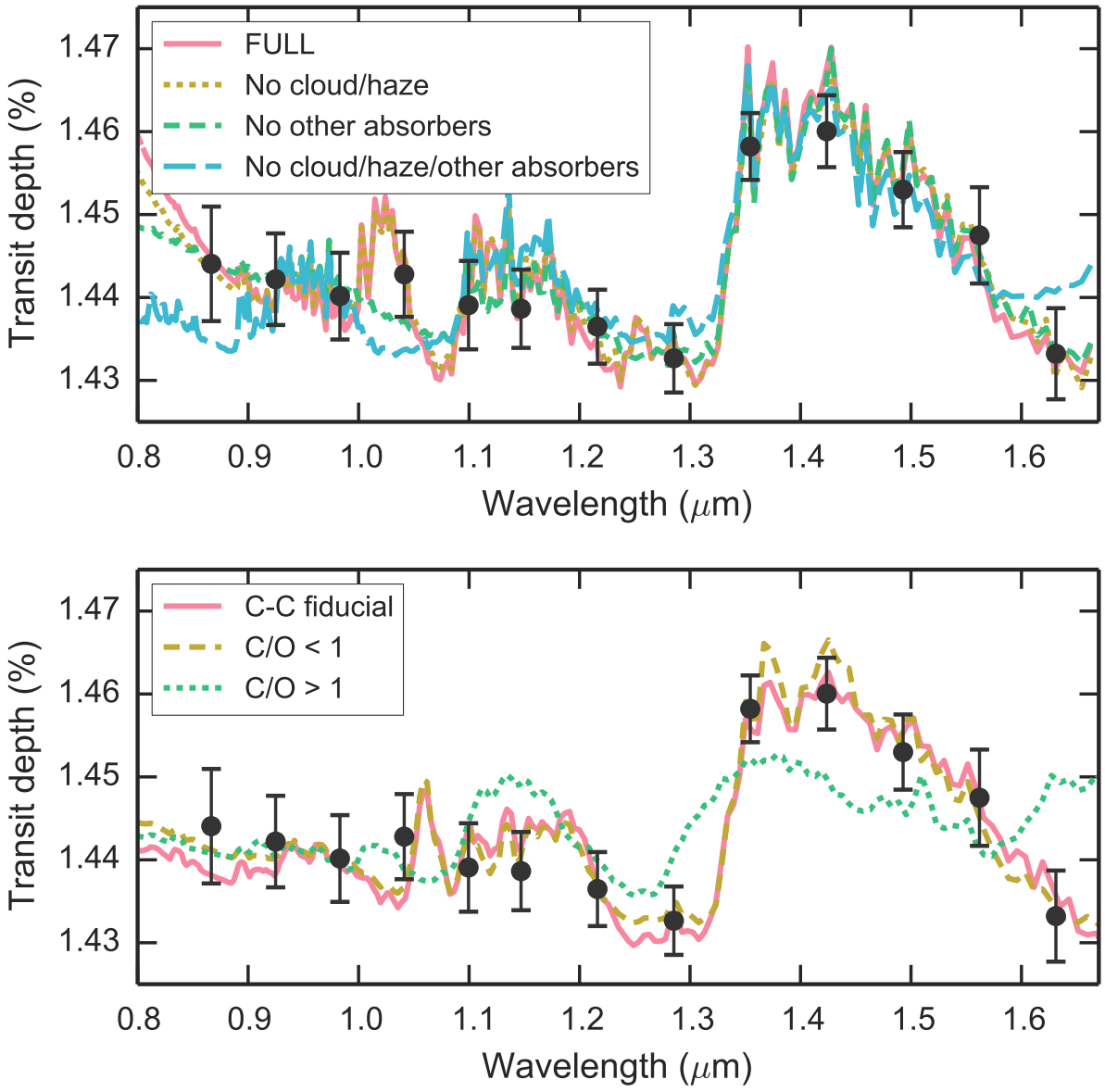

Best fits for different assumed models (lines) compared to the WFC3 transmission spectrum (points). Models are binned to a wavelength resolution of 0.01 μm. Results from the FREE and C-C parameterizations are shown in the top and bottom panels, respectively.

Figure 4.11: Pairs Plot for Retrieved Atmospheric Parameters

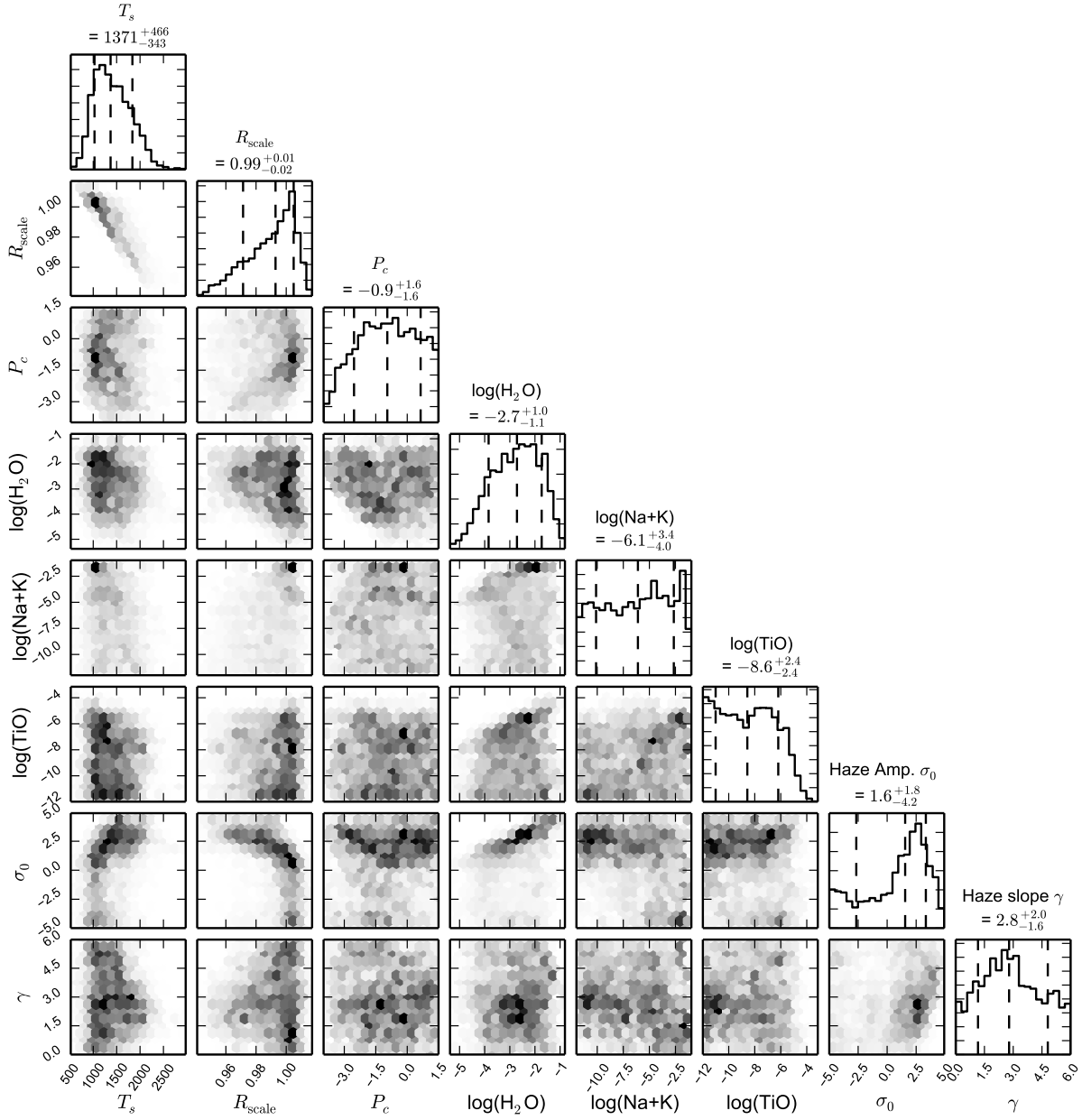

A pairs plot of the distribution of parameters retrieved with CHIMERA for the FULL model. The parameters are the scale height temperature T_s (in Kelvin), the planet radius scale factor $R_{\rm scale}$, the cloud-top pressure P_c (in log bars), the logarithm (base 10) of the molecular abundances, and the haze scattering amplitude σ_0 and slope γ. The off-diagonal plots show marginalized posterior probability density for pairs of parameters (darker shading corresponds to higher probability). The diagonal plots show marginalized posterior probability distributions for individual parameters, with the median and 68% credible interval marked with dashed lines.

Figure 4.12: Constraints on C/O, Metallicity, and Thermal Profile

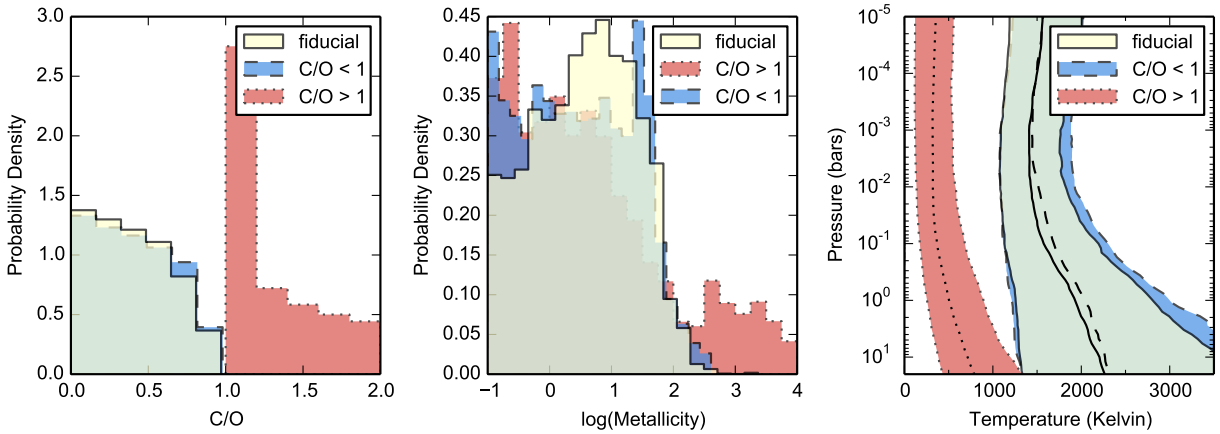

Retrieval results from the C-C parameterization. The left and middle panels show the marginalized distribution for C/O and metallicity. The right panel shows the median (black lines) and $1\,\sigma$ range (shaded regions) of 1000 randomly sampled temperature-pressure profiles for each scenario. Yellow, blue, and red shading correspond to constraints from the fiducial scenario (an uninformative prior on C/O), the oxygen-rich scenario (C/O < 1), and a carbon-rich scenario (C/O > 1). The distribution of C/O values for the carbon-rich model is normalized to have a probability mass of unity over the plotted range; however, the distribution has an extended tail toward higher C/O values that is not shown.

Figure 4.13: Retrieved Water Abundance Compared to Chemical Equilibrium Predictions

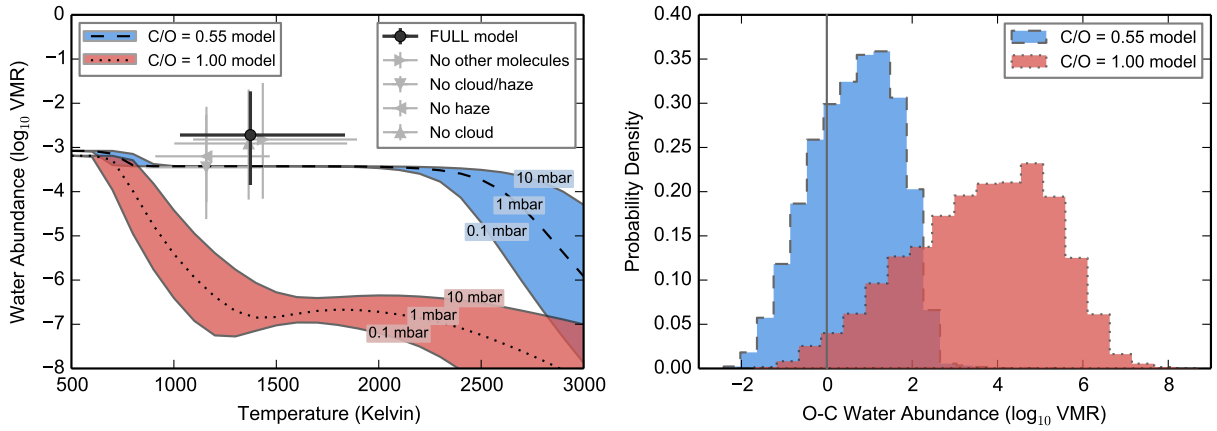

Left: Measurement of the water abundance and scale height temperature for WASP-12b (points) compared to equilibrium chemistry predictions of the water content for different atmospheric compositions (lines and shading). The black point indicates the water abundance and temperature measurements from the FULL model from the CHIMERA fit to the WFC3 spectrum. Results from other nested models are shown in gray. The black dashed line and blue shading correspond to water abundance predictions for a solar C/O composition, and the black dotted line and red shading correspond to C/O = 1. Both models have solar metallicity. For each model composition, the shading shows the span of predicted water abundances over pressures ranging from 0.1 - 10 mbar. The black lines correspond to 1 mbar, which is the typical pressure level probed by our observations. **Right:** Histogram of observed minus calculated water abundances for the FULL retrieval results relative to different model compositions. The red histogram (dotted line) shows the comparison with a carbon-rich model, and the blue histogram (dashed line) shows results for the oxygen-rich model. The gray vertical line marks zero, where the observations are an exact match to the model predictions.

Figure 4.14: Pressure Levels Sensed by the Transmission Spectrum

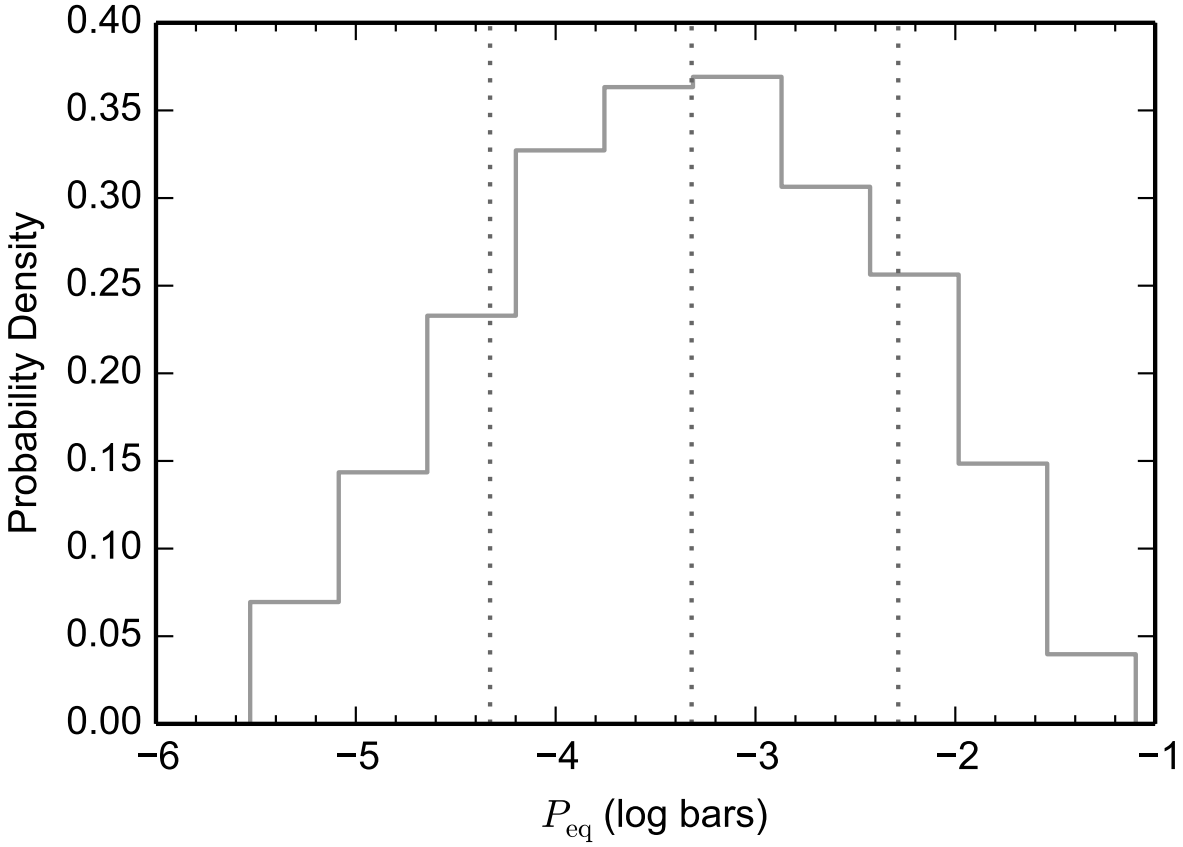

Histogram of equivalent pressures corresponding to an optical depth of 0.56 at 1.4 μm for each step in the MCMC chain for the FULL retrieval. The dotted lines indicate the median and surrounding 68% confidence interval.

CHAPTER 5

BATMAN: BASIC TRANSIT MODEL CALCULATION IN PYTHON

In this chapter, I introduce `batman`, a Python package for modeling exoplanet transit and eclipse light curves. The `batman` package supports calculation of light curves for any radially symmetric stellar limb darkening law, using a new integration algorithm for models that cannot be quickly calculated analytically. The code uses C extension modules to speed up model calculation and is parallelized with OpenMP. For a typical light curve with 100 data points in transit, `batman` can calculate one million quadratic limb-darkened models in 30 seconds with a single 1.7 GHz Intel Core i5 processor. The same calculation takes seven minutes using the four-parameter nonlinear limb darkening model (computed to 1 ppm accuracy). Maximum truncation error for integrated models is an input parameter that can be set as low as 0.001 ppm, ensuring that the community is prepared for the precise transit light curves we anticipate measuring with upcoming facilities. The `batman` package is open source and publicly available at https://github.com/lkreidberg/batman.

5.1 Introduction

The transit technique has revolutionized the study of exoplanetary systems. Thanks largely to the *Kepler* mission, thousands of planets have been discovered with this method (Rowe et al., 2015). These discoveries have yielded transformative constraints on planet occurrence rates over a wide range of planet sizes, orbital periods, and host star properties (Borucki et al., 2011; Youdin, 2011; Howard et al., 2012; Fressin et al., 2013; Dong & Zhu, 2013; Morton & Swift, 2014). They have also enabled the first estimates of the occurrence of habitable planets (Traub, 2012; Dressing & Charbonneau, 2013; Petigura et al., 2013; Kopparapu, 2013; Foreman-Mackey et al., 2014; Dressing & Charbonneau, 2015). Transit light curves can even reveal planets' atmospheric temperature structure and composition (e.g. Seager &

Sasselov, 2000; Charbonneau et al., 2002; Lecavelier Des Etangs et al., 2008; Sing et al., 2011; Deming et al., 2013; Knutson et al., 2014a; Fraine et al., 2014; Kreidberg et al., 2015). A number of current and planned observational facilities – including *K2*, *TESS*, *CHEOPS*, *JWST*, and *PLATO* – will measure precise transit light curves for thousands of exoplanets that will further advance our understanding of planet formation, evolution, and habitability.

Light curve models are a fundamental tool for transiting exoplanet science, but they are not trivial to compute quickly and accurately. Accurate calculation is challenging because the model must account for the planet's size and position on the sky, as well as stellar limb darkening, which causes the apparent brightness of the stellar disk to decrease from center to edge. The stellar intensity profile can be fit with several functional forms, including a linear limb darkening law (Schwarzschild & Villiger, 1906), quadratic (Kopal, 1950), square-root (Diaz-Cordoves & Gimenez, 1992), logarithmic (Klinglesmith & Sobieski, 1970), exponential (Claret & Hauschildt, 2003), and four-parameter nonlinear (Claret, 2000). For some of these profiles, model transit light curves can be calculated analytically (Mandel & Agol, 2002; Giménez, 2006; Abubekerov & Gostev, 2013). Other profiles do not have analytic solutions, and models must be calculated by numeric integration of the stellar intensity over the disk of the planet. In addition, speed is an important consideration because a large number of models must typically be calculated to make a robust estimation of transit parameters and their uncertainties.

A number of codes are available to calculate transit light curves. Mandel & Agol (2002) provide Fortran and IDL routines to compute models for quadratic and nonlinear limb darkening laws. The software packages `TAP` (Gazak et al., 2012) and `EXOFAST` (Eastman et al., 2013) include IDL implementations of the Mandel & Agol (2002) algorithm for quadratic limb darkening. `JKTEBOP` calculates models in Fortran for a broad range of limb darkening laws (Southworth et al., 2004). Kjurkchieva et al. (2013) introduce the pure Python code `TAC-maker`, which performs numeric integration for arbitrary limb darkening profiles. There are also routines available to model simultaneous transits by one or more bodies (Kipping,

2011; Pál, 2012). Most recently, Parviainen (2015) released the Python package `PyTransit`, which implements analytic models from Mandel & Agol (2002) and Giménez (2006).

In this paper, I introduce the open source Python package `batman`. This package is based on code that was used to model high-precision light curves obtained for atmosphere characterization (Kreidberg et al., 2014a,b, 2015; Stevenson et al., 2014a,b,c,d). The `batman` package enables fast computation of transit light curves for any radially symmetric limb darkening law, and currently supports uniform, linear, quadratic, logarithmic, exponential, and nonlinear limb darkening. Light curves for the first three of these are calculated analytically based on the formalism from Mandel & Agol (2002). Models for the remaining cases are computed with an efficient new integration scheme, described in § 5.2. The package also supports secondary eclipse modeling. I discuss `batman`'s features and performance in § 5.3 and conclude in § 5.4.

5.2 Algorithm

To calculate the fraction δ of stellar flux blocked by a transiting planet, one must integrate the sky-projected intensity of the star (I) over the area obscured by the disk of the planet (S):

$$\delta = \iint_S I \mathrm{d}S \tag{5.1}$$

where I is normalized such that the integrated intensity over the stellar disk is unity. This expression is valid for any general stellar surface brightness map; however, it is slow to evaluate numerically because the differential area elements must be small ($\lesssim 10^{-6}$) in order to achieve better than one part per million (ppm) accuracy.

On the other hand, if the stellar intensity profile is radially symmetric, the two-dimensional calculation in Equation 5.1 can be reduced to one dimension and sped up greatly

with the following algorithm:

$$\delta = \sum_{i=1}^{n} I\left(\frac{x_i + x_{i-1}}{2}\right)\left[A(x_i, r_p, d) - A(x_{i-1}, r_p, d)\right] \tag{5.2}$$

where x is the normalized radial coordinate $0 < x < 1$, $I(x)$ is the 1D stellar intensity profile, r_p is the planetary radius (in units of stellar radii), d is the separation of centers between the star and the planet (in stellar radii), and $A(x, r_p, d)$ is the area of intersection between two circles of radii x and r_p, separated by a distance d. The sum is carried out over the range $x_0 = \mathrm{MAX}(d - r_p, 0)$ to $x_n = \mathrm{MIN}(d + r_p, 1)$. The intersecting area is given by:

$$A(x, r_p, d) = \begin{cases} x^2 \cos^{-1} u + r_p^2 \cos^{-1} v - 0.5\sqrt{w}, & r_p - d < x < r_p + d \\ \pi x^2, & x \leq r_p - d \\ \pi r_p^2 & x \geq r_p + d \end{cases} \tag{5.3}$$

where

$$u = (d^2 + x^2 - r_p^2)/(2dx) \tag{5.4}$$

$$v = (d^2 + r_p^2 - x^2)/(2dr_p) \tag{5.5}$$

$$w = (-d + x + r_p)(d + x - r_p)(d - x + r_p)(d + x + r_p). \tag{5.6}$$

See Figure 5.1 for a schematic illustrating the geometry of the integration. The advantage of this integration scheme is that the only error introduced is due to approximating the stellar intensity as constant over the differential area element $\Delta A = A(x_i, r_p, d) - A(x_{i-1}, r_p, d)$. Computation of ΔA is expensive, but it needs to be calculated relatively few times ($<< 10^6$ for sub-ppm accuracy). This makes the integration faster than a scheme with a simpler area element (e.g., $\Delta A = \Delta x \Delta y$), that requires a much smaller step size to achieve the same accuracy.

The integration can be further optimized by using a nonuniform step size. Typical stellar

intensity profiles have larger gradients near the limb of the star than at the center (e.g. Claret, 2000), so smaller steps are required at larger x values to achieve the same accuracy. I adopt the following step-size scaling:

$$x_i - x_{i-1} = f \cos^{-1}(x_{i-1})$$

where f is a constant scale factor. This prescription is fast to compute and well-behaved at the limits $x = 0$ and $x = 1$.

5.3 The `batman` package

The Python package `batman` implements the algorithm described in § 5.2 and several analytic models to calculate transit light curves. `batman` is an open source project and is being developed on GitHub. Full documentation is available at https://github.com/lkreidberg/batman. I summarize the main capabilities of the package here.

5.3.1 Limb Darkening Models

`batman` supports calculation of exoplanet transit light curves for uniform, linear, quadratic, square-root, logarithmic, exponential, and four-parameter nonlinear stellar intensity profiles:

$$I(\mu) = I_0 \quad \text{(uniform)} \tag{5.7}$$

$$I(\mu) = I_0[1 - c_1(1-\mu)] \quad \text{(linear)} \tag{5.8}$$

$$I(\mu) = I_0[1 - c_1(1-\mu) - c_2(1-\mu)^2] \quad \text{(quadratic)} \tag{5.9}$$

$$I(\mu) = I_0[1 - c_1(1-\mu) - c_2(1-\sqrt{\mu})] \quad \text{(square-root)} \tag{5.10}$$

$$I(\mu) = I_0[1 - c_1(1-\mu) - c_2\mu\ln\mu] \quad \text{(logarithmic)} \tag{5.11}$$

$$I(\mu) = I_0\left[1 - c_1(1-\mu) - c_2/(1-\exp\mu)\right] \quad \text{(exponential)} \tag{5.12}$$

$$I(\mu) = I_0[1 - c_1(1-\mu^{1/2}) - c_2(1-\mu) - c_3(1-\mu^{3/2}) - c_4(1-\mu^2)] \quad \text{(nonlinear)} \tag{5.13}$$

Figure 5.1: Schematic Illustration of Integration Scheme

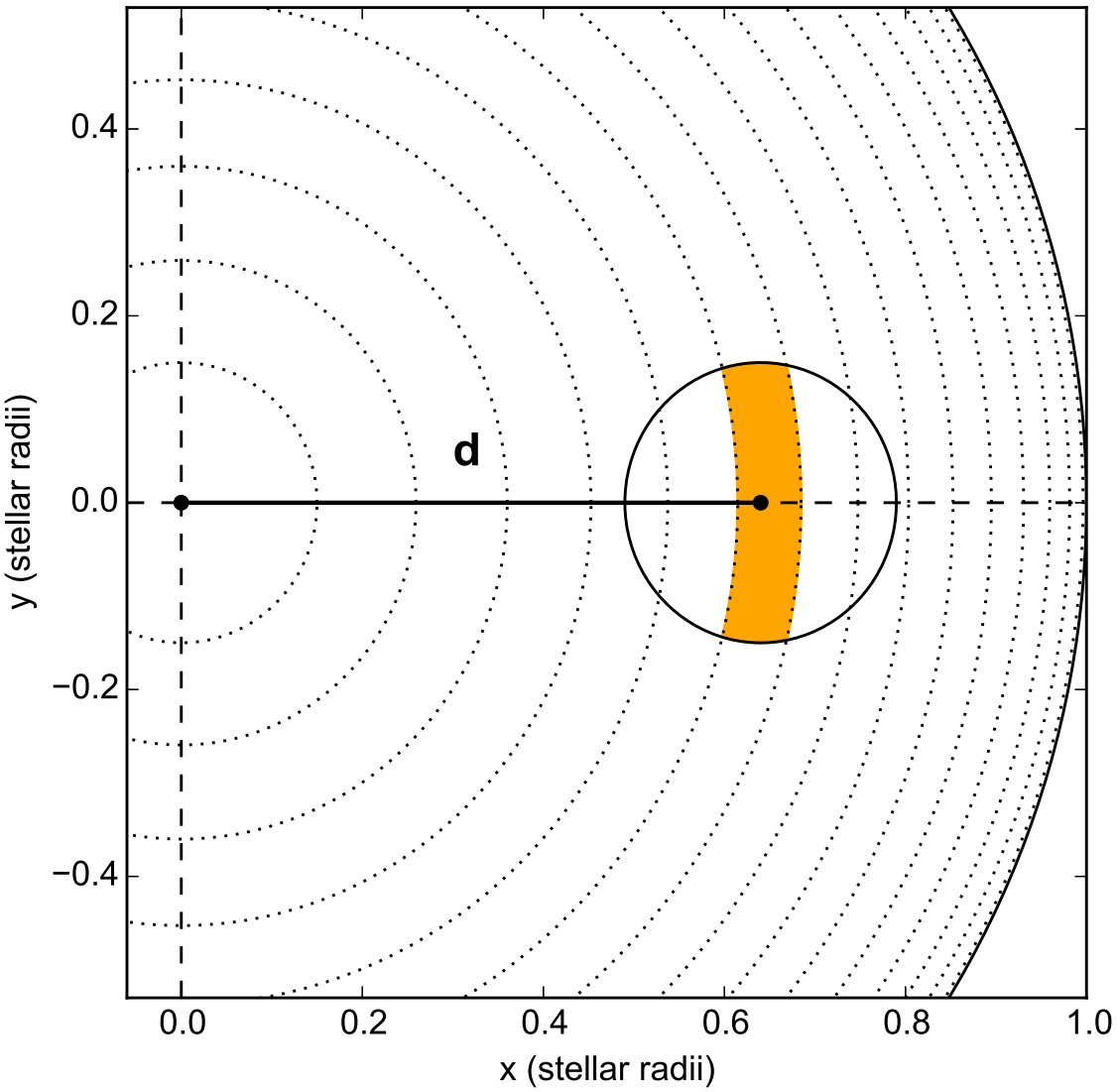

Schematic illustration of the integration scheme. The star (large black circle; partially visible) has a radius of 1 and is centered in the plane of the sky at $(x, y) = (0, 0)$. The planet (smaller black circle) is separated from the center of the stellar disk by a distance d (marked by the solid black line). The star is partitioned into concentric circles (dotted lines) in order to calculate the integral over the planet disk. A single integration element ΔA is shaded in orange. The integration step size illustrated here is larger than for a typical calculation for visual clarity. Note that because the stellar intensity profile is radially symmetric, the coordinate system can be chosen such that the planet lies on the x-axis, as shown.

where $\mu = \sqrt{1 - x^2}$ and $c_1, ..., c_n$ are limb darkening coefficients. The `batman` source distribution also includes a template for the creation of a custom profile for any radially symmetric function.

The square-root, logarithmic, exponential, nonlinear, and custom models are computed with the numeric integration scheme from § 5.2. The uniform, linear, and quadratic models are calculated analytically, with code based on the Fortran routines `occultquad.f` and `occultuniform.f` provided by Mandel & Agol (2002). For the analytic models, I follow Eastman et al. (2013) and use the algorithm from Bulirsch (1965) to improve calculation speed and accuracy for elliptic integrals of the third kind.

5.3.2 Secondary Eclipse Model

`batman` can also model secondary eclipses. Eclipse light curves are generated with

$$f = 1 + f_p(1 - \alpha)$$

where f is normalized flux, f_p is the planet-to-star flux ratio, and α is the fraction of the planet disk that is occulted by the star. The model is normalized such that the stellar flux is unity. For a separation d, the occultation fraction $\alpha(d) = \alpha_t(d)/r_p^2$, where $1 - \alpha_t(d)$ is the transit light curve with uniform limb darkening. Note that this model assumes the planet flux is constant for all orbital phases.

5.3.3 Utilities

`batman` includes a utility function to calculate the separation of centers d between the star and the planet based on orbital parameters of the system. The input parameters are the planet semi-major axis a, inclination i, eccentricity e, longitude of periastron ω, period P,

and time of inferior conjunction t_0. The separation of centers is given by:

$$d = \frac{a(1-e^2)}{1+e\cos f}\sqrt{1-\sin^2(\omega+f)\sin^2 i}$$

where f is the true anomaly. The true anomaly is calculated with the algorithm provided by Murray & Correia in Chapter 1 of Seager (2010). For circular orbits, we adopt the convention $f = \pi/2$.

`batman` provides utilities to calculate the time of periastron, time of inferior conjunction, and the secondary eclipse time from the other transit parameters, using the method described in §3.1 of Eastman et al. (2013). Note however that `batman` does not correct for the effects of light travel time.

An additional utility is light curve supersampling, which allows the user to calculate the average value of the light curve over a specified number of evenly spaced points during an exposure.

5.3.4 Accuracy

Recent transit observations have yielded signal-to-noise greater than 1000 per exposure (e.g. Kreidberg et al., 2014b; Knutson et al., 2014c). Accurate transit light curve calculation is essential for modeling such high precision measurements and will be increasingly important for data obtained with next-generation facilities. `batman` therefore enables the user to specify the maximum allowable truncation error for numeric integration. Figure 5.2 shows an example transit light curve and its truncation error.

To ensure that the truncation error is below the specified threshold, the integration step size is tuned during model initialization. Truncation error is measured relative to a model calculated with a very small step size ($f = 5\times10^{-4}$). For typical limb darkening profiles, this method is reliable for truncation errors down to $\sim 10^{-3}$ ppm. However, tuning the step size is a slow operation because it requires computing several light curve models (~ 10). As an

alternative, methods are available to set the step size directly and calculate the corresponding truncation error.

I tested the accuracy of the analytic model for quadratic limb darkening by comparing it to a numerically integrated model with an error tolerance of 0.001 ppm. The analytic model is accurate to 0.03 ppm for a test case with $r_p = 0.1$, $(c_1, c_2) = (0.1, 0.3)$, sampled at 10^6 evenly spaced points over the interval $0 < d < 1$. The accuracy is somewhat worse than machine epsilon because of error tolerance in the computation of special functions.

I also tested the accuracy of the widely-used Mandel & Agol (2002) code that uses Numerical Recipes functions to calculate elliptic integrals (Press et al., 1992). The accuracy was better than 0.005 ppm for most input values; however, for the case $r_p - d < \epsilon$, the error in the light curve exceeded 2 ppm. By contrast, the Bulirsch (1965) algorithm for elliptic integrals is well-behaved for this case and also faster.

5.3.5 Performance

Computationally intensive sections of code (including all of the transit model calculation) are written as C extension modules with the Python/C API, which improves the performance by a factor of 30 over a pure Python implementation for quadratic limb darkening. `batman` also includes the option to parallelize at the C level with OpenMP, which further speeds up the calculation. The number of processors is specified by the user. `batman` will raise an exception if the user attempts to parallelize a calculation on a system where OpenMP is not supported.

I tested `batman`'s performance over a range of typical use cases with a 1.7 GHz Intel Core i5 processor. In Figure 5.3, I show the truncation error versus execution time for a single transit light curve calculation using a nonlinear intensity profile, compared to the execution time for a quadratic model computed analytically. The test case consists of 100 points evenly sampled in time during the planet's transit. I used physical parameters for the transiting planet GJ 1214b (Kreidberg et al., 2014b). The stellar intensity profile is the

Figure 5.2: Example Transit Light Curve and Truncation Error

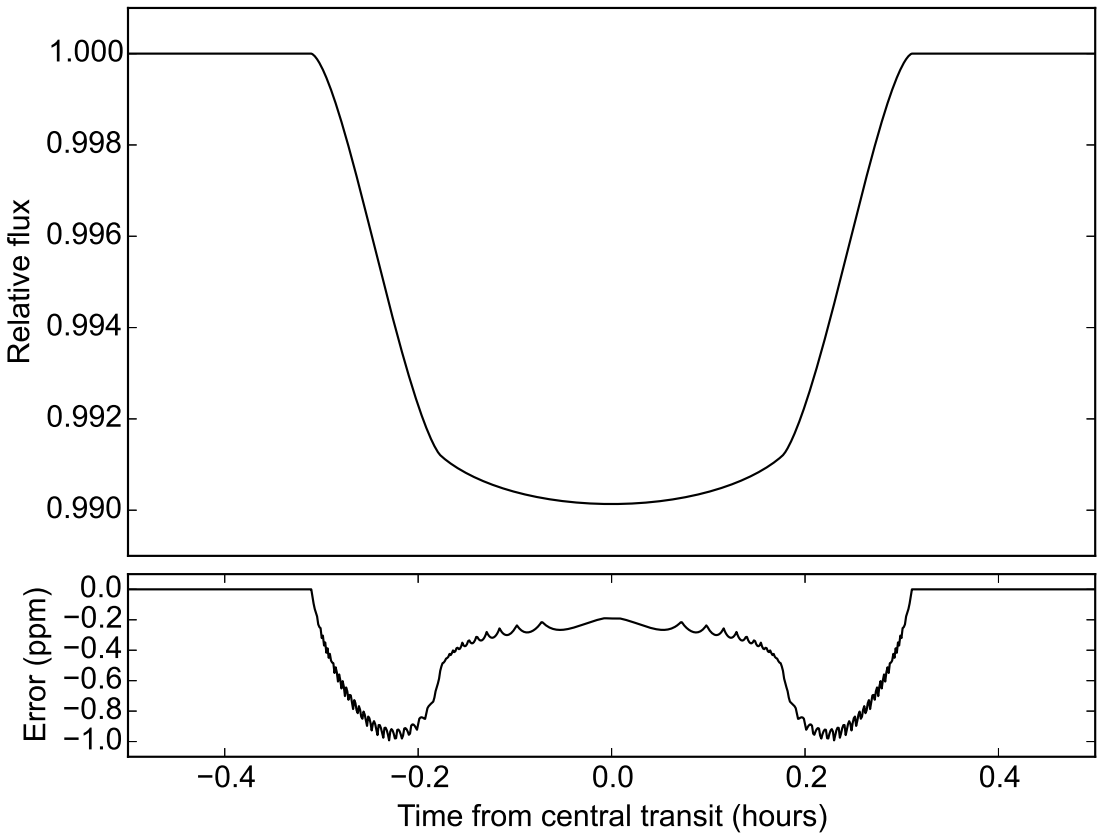

An example transit light curve for a nonlinear stellar intensity profile (top panel) and truncation error for the calculation (bottom panel). The error tolerance parameter was set to 1.0 ppm. The truncation error increases with distance from the center of the star up to around ± 0.2 hours from the time of mid-transit, because the stellar intensity gradient is larger at larger radii. The error decreases again during ingress and egress as the planet eclipses a smaller fraction of the stellar disk.

Figure 5.3: Performance for Numeric Integration Versus Analytic Model

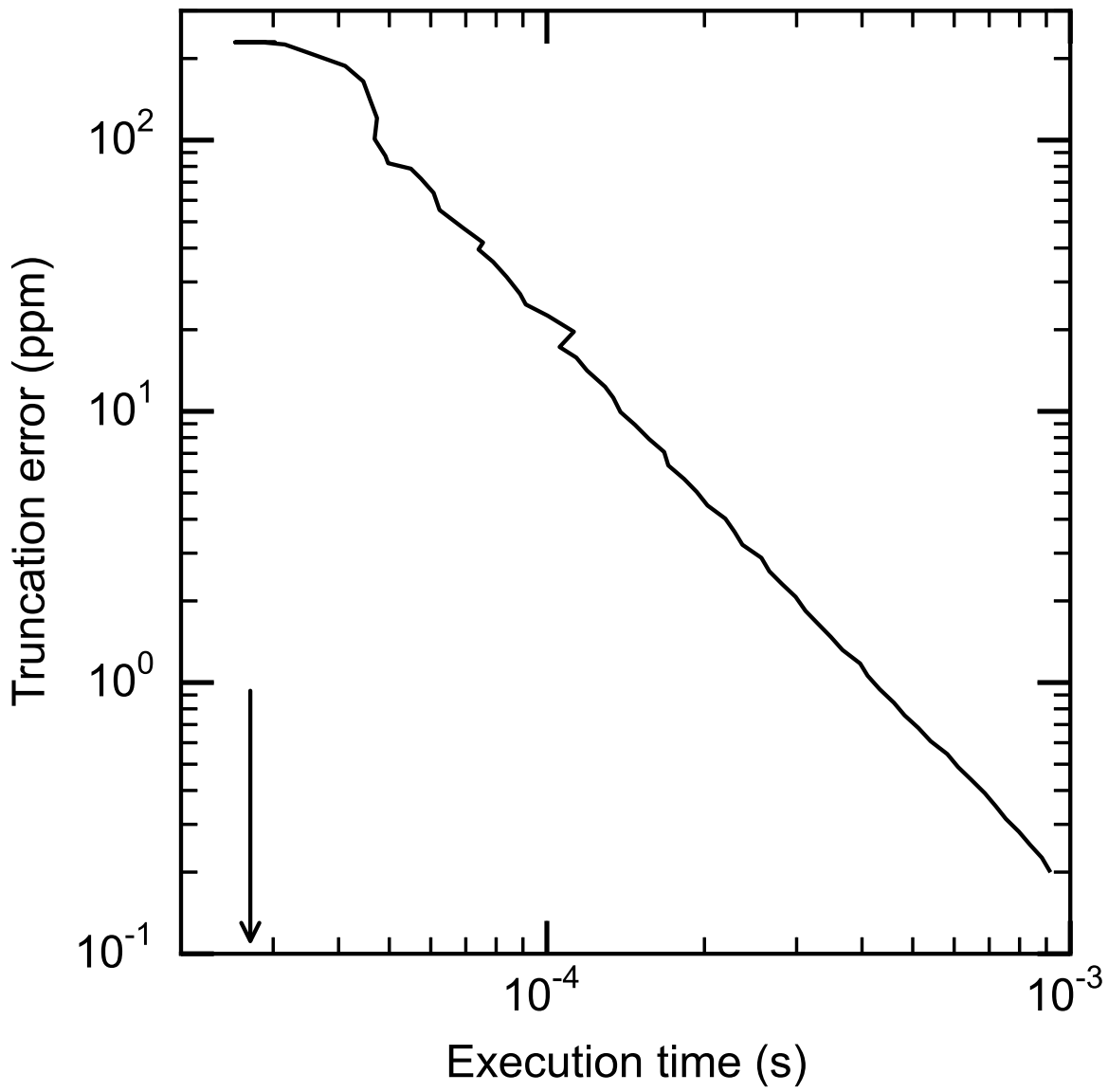

Truncation error as a function of execution time for a light curve modeled with the nonlinear limb darkening law (black line). The execution time for a quadratic model (computed analytically to better than 0.05 ppm accuracy) is indicated by the arrow. Calculations were made with a 1.7 GHz Intel Core i5 processor.

same for the nonlinear and quadratic models: the nonlinear limb darkening coefficients are $(0.0, 0.7, 0.0, -0.3)$ and the quadratic coefficients are $(0.1, 0.3)$. Decreasing the truncation error by a factor of 10 increases the computation time by a factor of three.

5.3.6 Comparison with Analytic Models for Nonlinear Limb Darkening

I explored using an analytic model to calculate transit light curves for the four-parameter nonlinear limb darkening profile. The analytic solution for nonlinear limb darkening was presented in Mandel & Agol (2002), but it is not used in any published software packages. The original code provided by Mandel & Agol (2002) uses a numeric integration scheme that is 20 times slower than the algorithm presented in § 5.2 (for an error tolerance of 1 ppm).

The analytic solution is challenging to compute because it uses the Appell F1 hypergeometric function. This function is only convergent for certain regions of parameter space and must be calculated with analytic continuation for other cases. Colavecchia & Gasaneo (2004) provide a Fortran library for computing Appell F1. I used this library to implement the analytic model for nonlinear limb darkening. However, the returned Appell F1 values are not accurate for all input parameters, based on a comparison with `Mathematica` and the pure Python library `mpmath`. Even for cases where F1 is correct, the computation is over an order of magnitude slower than numeric integration (for an error tolerance of 0.1 ppm). I concluded that integration is a faster and easier solution than analytic models for the four-parameter nonlinear limb darkening law.

5.4 Summary

I introduced a new algorithm for computing transit light curves for any radially symmetric stellar limb darkening law. I also described the open-source Python package `batman`, a versatile code to generate model transit and eclipse light curves. Uniform, linear, quadratic, logarithmic, exponential, and four-parameter nonlinear limb darkening laws are

currently supported. `batman` uses C extension modules to compute light curves and is parallelized with OpenMP to optimize performance. Light curves can be calculated with accuracy better than 0.001 ppm, ensuring that the community is prepared to model the extraordinarily precise data we anticipate from upcoming facilities. `batman` is available at `https://github.com/lkreidberg/batman` and is also hosted on the Python Package Index under the name `batman-package`.

CHAPTER 6

A SPECTROSCOPIC PHASE CURVE FOR THE HOT JUPITER WASP-103b

In this chapter, I describe preliminary results for the phase-resolved thermal emission spectrum of the hot Jupiter WASP-103b. This work is based on data from *Spitzer* Program 11099 (PI: L. Kreidberg).

6.1 Introduction

Thermal phase curves measurements are a direct probe of exoplanet climate. The phase curve technique uses time-series observations of a planet's thermal emission over an entire revolution on its spin axis. As the planet's orbital phase changes, different regions of the atmosphere are observable, enabling measurements of the variation in temperature with longitude (Cowan & Agol, 2008). Figure 1.2 illustrates the geometry of phase curve observations.

Short-period planets are ideal candidates for phase curves. They are expected to be tidally locked, so their rotation periods are known. Moreover, tidally-locked planets should have large temperature gradients with longitude, because they have one face continuously blasted by intense stellar radiation (the dayside), and the other in perpetual darkness (the nightside). Accordingly, the first thermal phase curve observations were measured for hot Jupiters with *Spitzer*/IRAC (e.g., Harrington et al., 2006; Knutson et al., 2007b; Cowan et al., 2007). These measurements have revealed climates vastly different from those in the Solar System. For example, the hottest planets have poor heat redistribution, leading to temperature contrasts between day- and nightside in excess of 1000 Kelvin (e.g., Cowan et al., 2012). Hot Jupiters have also been shown to have high wind speeds (> 1 km/s), based on comparisons between the observed phase variation and atmospheric circulation models (Showman et al., 2009).

Recently, Stevenson et al. (2014d) made the first *spectroscopic* phase curve observation. They targeted the hot Jupiter WASP-43b with *HST*/WFC3 and measured its phase-resolved thermal emission spectrum from $1.1 - 1.7\,\mu$m. Spectroscopy is an important advance over previous photometric observations with *Spitzer*: with photometry alone, we cannot distinguish between phase variations caused by changes in temperature at a given altitude, versus changes in opacity that result in sensing a different altitude. Spectroscopic observations break this degeneracy between composition and thermal structure by unambiguously resolving spectral features. A further advantage of WFC3 observations is that they cover the wavelength region near the peak of the planet's spectral energy distribution, enabling a robust accounting of its energy budget. Using spectroscopic phase curve measurements, Stevenson et al. (2014d) retrieved WASP-43b's temperature-pressure profile at 15 distinct orbital phases. The best fit models have temperature decreasing with altitude at all phases, which is consistent with expectations from 3D circulation models (Kataria et al., 2014a). They also found that WASP-43b has poor heat redistribution, a low Bond albedo, and an altitude-dependent hot spot.

Here we make spectroscopic phase curve observations for a second planet, the newly discovered hot Jupiter WASP-103b (Gillon et al., 2014). WASP-103b orbits an F8 star every 22 hours, making it one of the most highly irradiated transiting planets known ($T_{\rm eq} = 2500$ K). It is an ideal candidate for comparative planetology with WASP-43b, because it has a similar orbital period and surface gravity but much higher equilibrium temperature. It is so hot that the atmosphere may be partially ionized and coupled to the planet's magnetic field, resulting in qualitatively different dynamics (e.g., Batygin et al., 2013). The measurements presented here are the first study of WASP-103b's atmosphere.

6.2 Observations and Data Reduction

We observed four complete phase curves in total for WASP-103b: two with *HST*/WFC3 and one each with *Spitzer*/IRAC 3.6 and 4.5 μm channels.

6.2.1 HST/*WFC3*

The *HST* observations consisted of two visits on 26-27 February and 2-3 August 2015. Each visit was 15 orbits in duration and spanned 23 hours. We took a direct image of the star with the F126N filter at the beginning of each orbit to determine the wavelength solution. The remainder of the orbit consisted of time-series spectroscopy with the G141 grism and the 256 x 256 pixel subarray. We used the SPARS10/NSAMP = 15 read-out mode, which has an exposure time of 103 seconds. The exposures were taken with the spatial scan observing mode with a scan rate of 0.03"/s, alternating between forward and backward scanning on the detector to diminish overhead time. The scan height was 25 pixels and the peak counts were 30k photoelectrons per pixel. We collected a total of 18 spatial scan exposures per orbit. Our analysis also uses secondary eclipse observations of WASP-103b from *HST* program 13660 (PI: M. Zhao), which obtained time series spectroscopy with the G141 grism using a similar setup. Further description of the observational design for this program is given in Star Cartier (in prep).

We reduced the data from both programs using a custom pipeline that has been developed for past analyses of WFC3 data (for details see Kreidberg et al., 2014b,a, 2015). The raw data exhibit time-dependent systematic trends typically seen in WFC3 light curves, which we correct using a systematics model of the form:

$$F_{\rm sys}(t) = (c\,S(t) + v_1\,t_{\rm v} + v_2\,t_{\rm v})(1 - \exp(-a\,t_{\rm orb} - b)) \tag{6.1}$$

where $t_{\rm v}$ is time elapsed since the first exposure in a visit and $t_{\rm orb}$ is time since the first exposure in an orbit. $S(t)$ is a scale factor equal to 1 for exposures with spatial scanning in the forward direction and s for reverse scans. In the fit, c, v_1, v_2, a, b, and s are free parameters. The first orbit in each visit shows larger systematic trends than subsequent orbits, so we exclude these data in our final analysis (a common practice; see e.g. Kreidberg et al., 2014b).

We fit the systematics model simultaneously with the physical parameters for the system. The complete model is

$$F(t) = F_{\rm sys}(t)\,[T(t) + (E(t) - 1)(1 + A\cos(2\pi(t - \theta)/P))] \tag{6.2}$$

where $T(t)$ is a transit model, $E(t)$ is an eclipse model, P is the planet orbital period, and A and θ are free parameters to fit the amplitude and offset for the thermal phase variation. The free parameters for the transit and eclipse model are the planet-to-star radius ratio r_p/r_s, the planet-to-star flux ratio f_p/f_s, and a linear limb darkening parameter. The eclipse model is normalized such that the flux during eclipse is 1 and out of eclipse is f_p/f_s, and the transit model is normalized to unity out of transit. The planet's orbital parameters are poorly constrained by the WFC3 light curve due to incomplete phase coverage, so we fix the inclination to $i = 84.54°$, the semi-major axis to stellar radius $a/R_s = 2.925$, based on the best fit to the *Spitzer* Channel 2 light curve (described below). We use the orbital period $P = 0.925545613$ day, and time of inferior conjunction $t_0 = 2456836.2964455$ from Southworth et al. (2015). All free parameters were assumed to have a common value for both *HST* visits, with the exception of c, v_1 and v_2, which were allowed to vary between visits. We explored adding an additional cosine term to model the thermal phase variation, but the additional degrees of freedom are not justified according to the Bayesian Information Criterion (BIC). The transit and eclipse models were calculated with the `batman` package (Kreidberg, 2015). Figure 6.1 shows the fitted broadband phase curve.

6.2.2 Spitzer*/IRAC*

The *Spitzer* observations had the following setup. Each phase curve observation consisted of 30 hours of time series photometry, which covered a full orbital revolution of the planet. The observations were timed to contain two eclipses with three hours of baseline on either side. We used 12 s exposures to maximize the duty cycle without saturating the detector. The

Figure 6.1: Band-Integrated WFC3 Phase Curve for WASP-103b

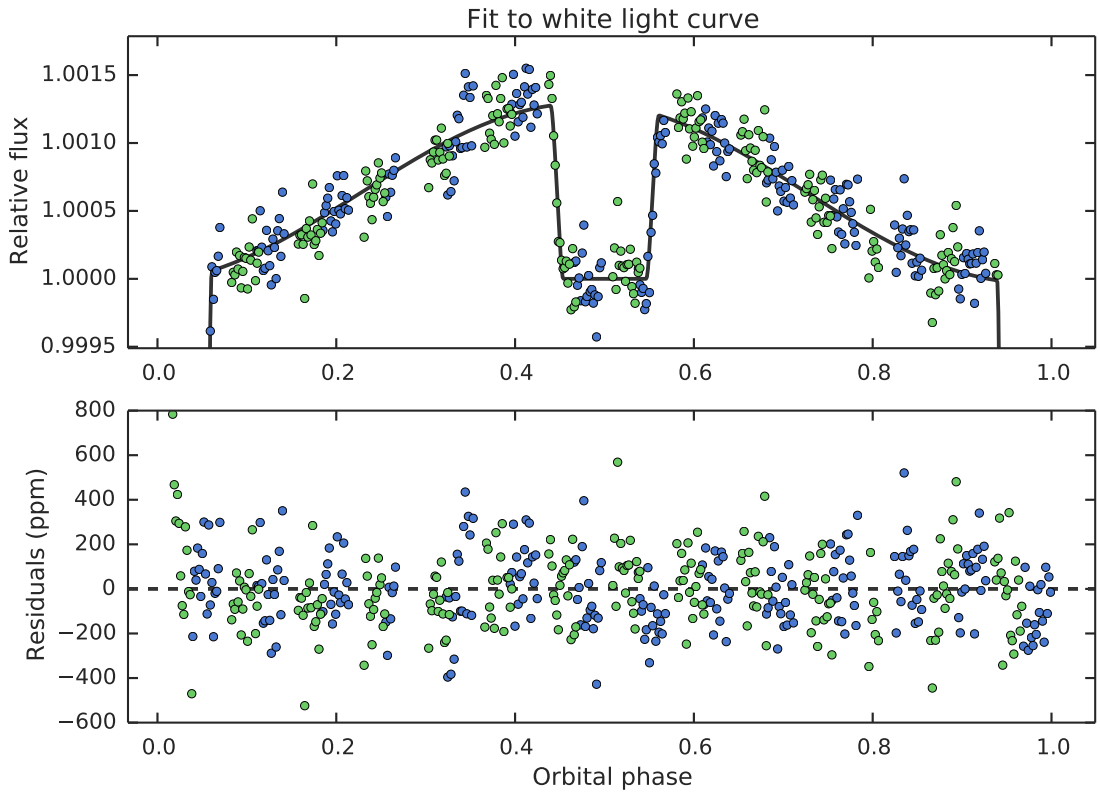

The WASP-103b phase curve from *HST*/WFC3 compared to the best-fit model (top) and the residuals from the fit (bottom). This is the "white" light curve, with flux integrated over the entire wavelength region covered by the spectrum. Blue and green points correspond to visits 1 and 2, respectively. The secondary eclipse occurs at phase 0.5 and the thermal phase variation is clearly apparent with an amplitude of about 1000 parts per million.

dominant systematic in high-precision Spitzer time series is the intrapixel effect (variations in flux caused by imprecise pointing). To minimize this effect, we used PCRS peak-up to improve the pointing accuracy. We began each observations with a 30-minute position settling period, followed by three Astronomical Observation Requests (AORs) of equal duration. At the beginning of each AOR, the telescope was repointed to position the target in the "sweet spot" of the detector.

We reduced the data using the POET pipeline and fit the systematics with the BLISS mapping technique (Stevenson et al., 2012). This technique creates a map of the intrapixel sensitivity while simultaneously fitting for other systematics and the physical parameters of the system. In addition to the intrapixel sensitivity map, we fit the data for a linear trend in time and used the same transit, eclipse, and phase variation model as in Equation 6.2.

We tested the light curve fits for time-correlated noise by calculating the root mean square (rms) of the fit for a range of bin sizes. For white noise, the rms should decrease as the square root of the number of points in the bin. The 4.5 μm phase curve data follow this trend; however, the 3.6 μm data have larger than expected rms at large bin sizes. The time-correlated noise is also noticeable in the residuals to the light curve fit (Figure 6.2). To account for additional uncertainty due to the correlated noise in this channel, we use the wavelet technique of Carter & Winn (2009).

6.2.3 Spitzer/*IRAC*

Companion Star Characterization

WASP-103b has a faint companion at an orbital separation of 0.2" (Wöllert & Brandner, 2015). We obtained high contrast AO imaging of the system with Keck/NIRC2 on 2016 Jan 25. We reduced the data with the pipeline of Ngo et al. (2015) and measured a primary to secondary flux ratio of 9.348 ± 0.255, 7.702 ± 0.070, and 6.109 ± 0.106, in J, H, and K_s, respectively.

Figure 6.2: Spitzer Phase Curves for WASP-103b

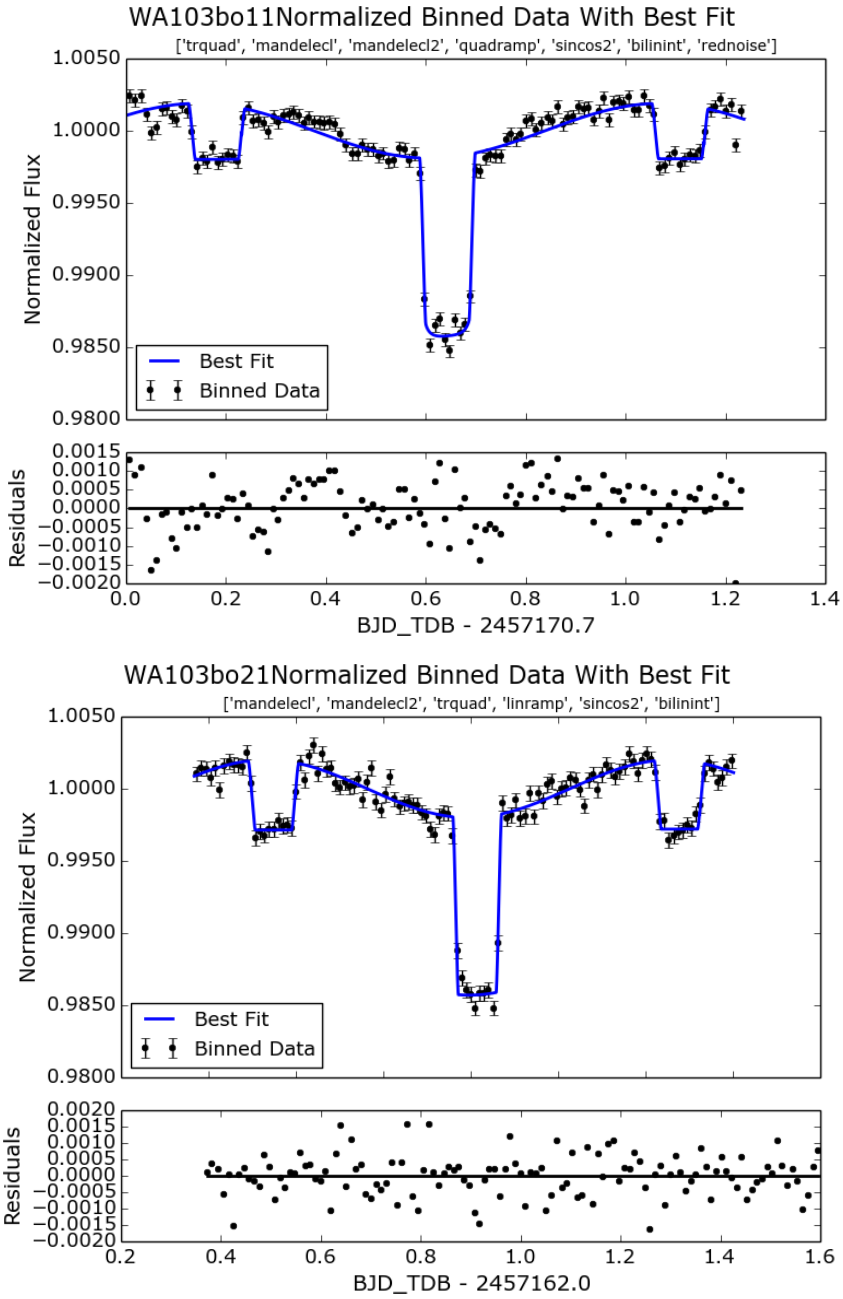

Spitzer phase curves for WASP-103b at 3.6 and 4.5 μm (top and bottom panels). The data are binned in intervals of 10 minutes for display purposes only. The phase curves show are qualitatively similar to the *HST* phase curve, with poor heat redistribution from day to night side and peak brightness occuring near secondary eclipse.

Figure 6.3: WASP-103b Companion

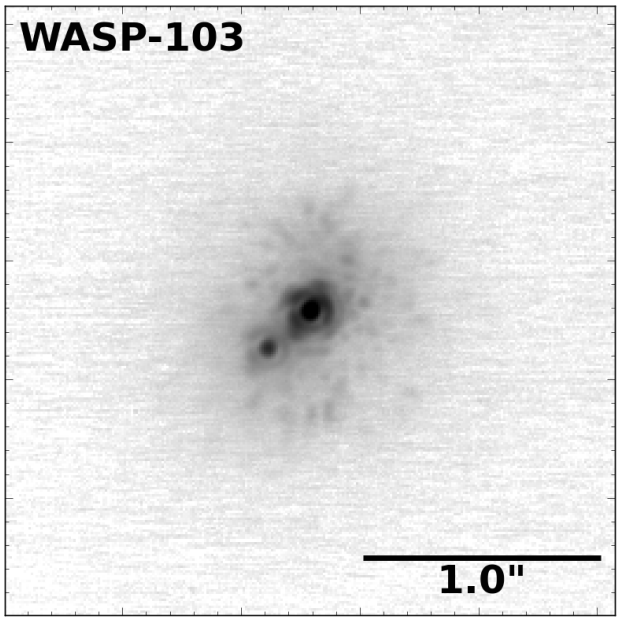

A K_s band image of the WASP-103 system from Keck/NIRC2.

We characterized the properties of the companion by fitting a model to the primary to secondary flux ratios of the form:

$$\frac{F_1}{F_2} = \frac{f \times \int \phi(\lambda) I(\lambda, T_1)}{\int \phi(\lambda) I(\lambda, T_2)} \tag{6.3}$$

where F_1/F_2 is the flux ratio, $I(\lambda, T)$ is the blackbody intensity, $\phi(\lambda)$ is the filter throughput, and f is a scale factor to account for the unknown distance and size of the companion. We assume a stellar temperature $T_1 = 6110\,\mathrm{K}$ based on Gillon et al. (2014). The best fit companion temperature is $T_2 = 3600 \pm 90$ and the scale factor is 2.25 ± 0.15. Assuming the primary and secondary are equidistant, which is reasonable given their small projected separation, this scale factor implies a ratio of areas $R_1^2/R_2^2 = 2.25$. The radius of WASP-103 is $1.7\,R_\odot$, giving a companion radius $R_2 = 1.1\,R_\odot$ – an unphysically large value for a star with temperature $T_2 = 3600$. However, we obtain a physically plausible solution assuming WASP-103 is a triple system with two low-temperature companions each with radius of

about half that of the Sun.

We correct the transit depths for the presence of these companions according to $\delta' = (1 + \alpha)\delta$, where δ is the uncorrected depth and α is the ratio F_2/F_1 based on Equation 6.3. Similarly, the planet-to-star flux ratio is corrected by $(f_p/f_s)' = (1 + \alpha)(f_p/f_s)$.

6.3 Preliminary Results

Using the reduced data from the previous section, we created phase-resolved emission spectra for WASP-103b based on model fits to the spectroscopic phase curves. At each wavelength bin, we ran an MCMC to explore the range of model parameters that provide a good fit to the data. We then took the mean and 68% credible interval for the planet-to-star flux at a selection of orbital phases (0.15, 0.3, 0.45, 0.6, 0.75, and 0.9). The phase-resolved emission spectra are shown in Figure 6.4 (WFC3 data only).

We note that the uncertainties for the phase-resolved spectra may not be robust. We initially chose to compute uncertainties based on the model fits because this approach can account for correlations with other model parameters and the presence of red noise. However, the model can be evaluated at an arbitrarily large number of orbital phases, so the phase-resolved spectra created with this technique are not statistically independent. We are exploring alternative approached to determining errors for the spectra and stress that the measurements presented here are preliminary.

Nevertheless, the spectra show some qualitative trends that are worth discussing. The most noteworthy feature is the sharp increase in planet-to-star flux near phase 0.5. The nightside flux is nearly 0, which suggests poor heat redistribution, in agreement with other results for the shortest period hot Jupiters (Komacek & Showman, 2016). The spectra to do not exhibit noticeable features corresponding to any of the expected absorbing species (e.g. water, carbon monoxide, carbon dioxide, or methane).

We investigate the atmospheric composition in detail with the thermal emission spectrum. We measured the dayside planet-to-star flux with a total of four eclipse observations

(shown in Figure 6.5). The error bars correspond to the 68% credible intervals on f_p/f_s from an MCMC fit to the full phase curve, which we consider a reliable estimate of the uncertainty. The dayside spectrum is surprising because it does not exhibit the strong water absorption feature predicted for a solar composition model atmosphere; rather, the spectrum is consistent with expectations for a blackbody with temperature $T = 2700$ K.

We considered three possible explanations for the lack of features in the dayside spectrum. One is that the atmosphere has a carbon-rich composition (with a ratio of carbon to oxygen C/O = 1). This composition results in a depleted water abundance because most of the oxygen atoms are bound in CO and CO_2. We also considered a metal-poor composition, with [Fe/H] $= -2$. The third possibility is that the dayside hemispherically averaged temperature-pressure profile has a weak gradient, so we calculated the best fit model with an isothermal dayside.

All three of these models provide an adequate fit to the data; however, we consider the third option to be the most plausible. Studies of other hot Jupiters have shown that high C/O ratios and metal-poor compositions are unlikely (Line et al., 2014; Sing et al., 2016). On the other hand, 3D models of atmospheric circulation have shown that the dayside temperature profile should have a weaker gradient than is predicted from simpler 1D models (Fortney et al., 2006). However, this result is qualitatively different from the spectrscopic phase curve we measured for WASP-43b, which showed decreasing temperature with pressure at all orbital phases (Stevenson et al., 2014d). We will further explore the difference between WASP-103b and WASP-43b with the next steps for this analysis, outlined below.

6.4 Future Work

Future plans for this analysis are to:

- Develop a robust method for determining uncertainties for the phase-resolved emission spectra.

- Perform a complete retrieval analysis with the CHIMERA Bayesian Retrieval suite (Line et al., 2013b; Line & Yung, 2013b; Line et al., 2014, 2013a) to determine the range of atmospheric compositions and thermal structure allowed by the data.

- Compute the planet's Bond albedo and heat redistribution efficiency and compare with results for other hot Jupiters.

- Compare the atmospheric thermal structure to predictions from 3D general circulation models (e.g. Kataria et al., 2014b) to constrain the atmospheric dynamics and assess whether a weak dayside temperature gradient is a natural outcome.

These results will serve as a benchmark for interpreting the dayside spectra of other hot Jupiters, a test case for a 3D models of atmospheric circulation, and a preview of the high precision results we expect from future observations with *JWST*.

Figure 6.4: Phase Resolved Emission Spectra for WASP-103b

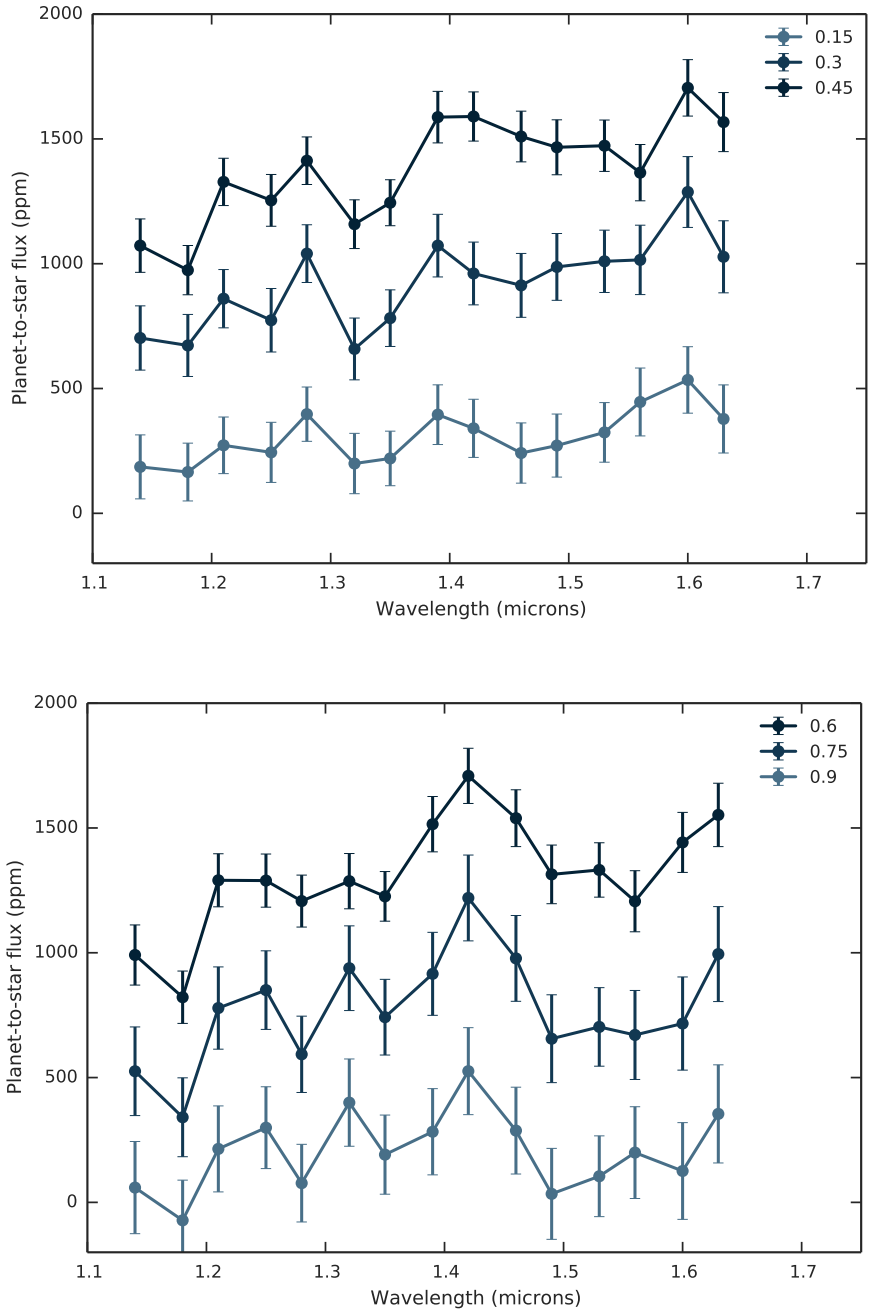

Emission spectra for WASP-103b at six distinct orbital phases. The top panel shows phases 0.15, 0.3, and 0.45; the bottom shows 0.6, 0.75, and 0.9. The planet-to-star increases toward phase 0.5, where the planet experiences peak insolation.

Figure 6.5: WASP-103b Dayside Emission Spectrum

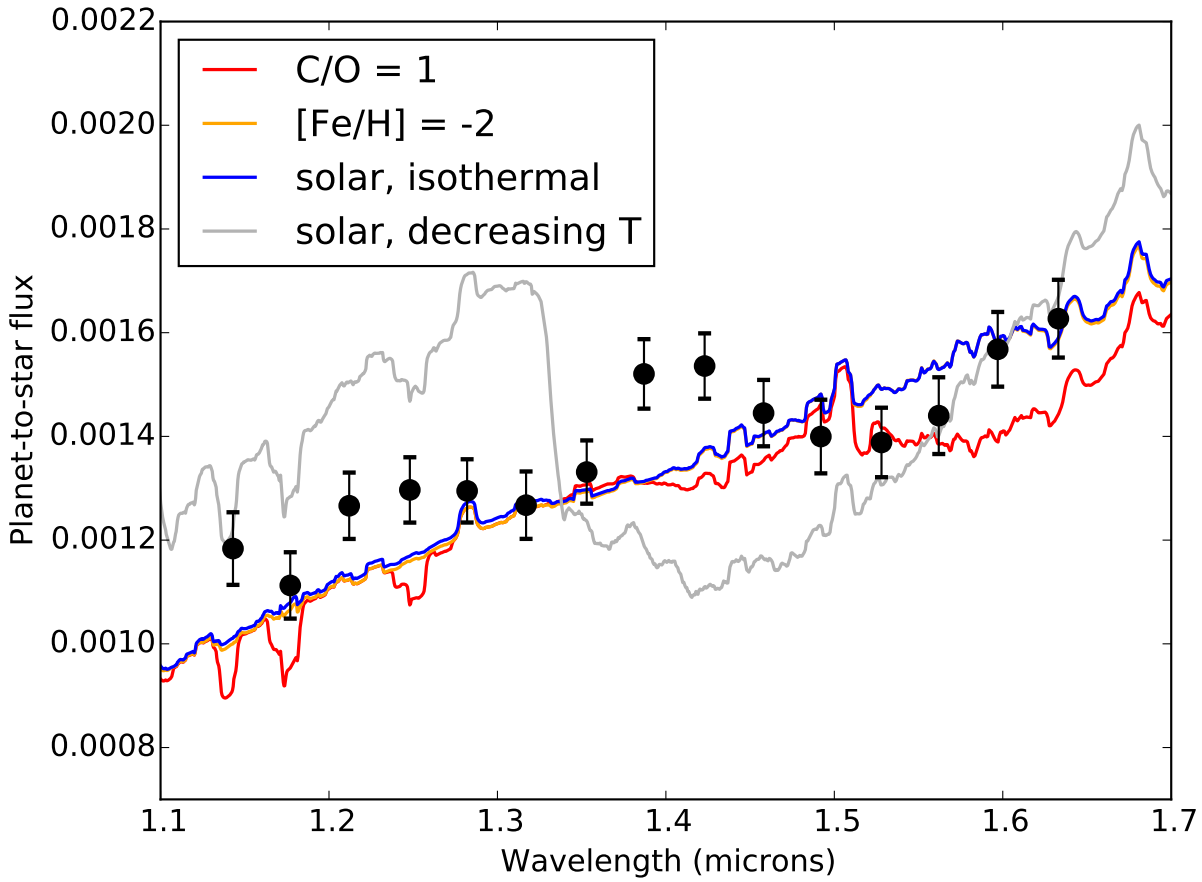

The dayside thermal emission spectrum of WASP-103b based on four eclipse observations with *HST*/WFC3 (black points). The data are compared to the best fit models for four different scenarios: (1) a carbon-rich atmosphere composition with C/O = 1 (red line), (2) a low metallicity composition (0.01x solar, orange line), (3) a solar composition atmosphere with an isothermal dayside temperature (blue line), and (4) a nominal model with solar composition and decreasing temperature with altitude (gray line).

CHAPTER 7

CONCLUSIONS & FUTURE PROSPECTS

7.1 Conclusions

In this thesis, I have presented work to characterize the atmospheres of four extrasolar planets to reveal their composition, climate, and cloud properties. There are several take-away points from these investigations that are worth emphasizing:

- The more data the better. All the results presented here rely on repeated observations of the target – as many as 15, in the case of GJ 1214b (Kreidberg et al., 2014b). This approach breaks degeneracies between instrument systematics (which change with every visit) and the astrophysical signal (which remains constant), enabling photon-limited measurement precision. Stacking observations can therefore successfully reveal tiny spectral features (or lack thereof) – down to ~ 100 ppm in amplitude. For GJ 1214, this strategy yielded a measurement precise enough to detect an Earth-like atmospheric composition for the first time, which bodes well for similarly intensive study of small planets with *JWST*.

- Spectral features from planetary atmospheres may be smaller than expected. For example, we saw for GJ 1214b that high altitude clouds or haze must be present in the atmosphere, obscuring high altitude layers and truncating features in the transmission spectrum. Clouds have been seen for other planets as well, and are fairly common over a range of temperatures and surface gravities (Sing et al., 2016). Based on these results, it is worth keeping in mind that cloud-free atmosphere models may not be realistic. For future observations we will either need to acquire higher precision data, to see features above the cloud deck (as we did for WASP-12b), or focus instead on emission spectroscopy or reflected light spectra, which are less affected by clouds (Fortney, 2005; Morley et al., 2015).

- Observing a planet from more than one angle – either by combining transit and eclipse measurements or obtaining a full orbit phase curve – can provide stronger constraints on the nature of the atmosphere than any one of these techniques alone. As one example, Kreidberg et al. (2014a) made independent water abundance measurements for WASP-43b using both the transmission spectrum *and* emission spectrum. The combination of these data sets showed that the abundance measurement was robust (they agreed), and also improved the precision to a level that is on par with the constraints for the Solar System planets. Similarly, phase curve observations can uniquely constrain a planet's energy budget, climate, and even wind speeds – even at a distance of hundreds of parsecs! (Stevenson et al., 2014d, Kreidberg et al., in prep).

- Spectroscopy beats photometry. As Burrows (2014) wrote, the interpretation of photometry suffers from the problem of "too few data points in pursuit of too many quantities". This challenge is apparent in the case of WASP-12b, where we obtained spectroscopy (Kreidberg et al., 2015) that disagrees with past inferrence of the atmospheric composition driven by photometry (Madhusudhan et al., 2011c; Stevenson et al., 2014c). Further work is needed to reconcile the measurements, but the spectroscopy is much easier to interpret because it uniquely identifies the dominant absorbing species (water).

Together, these results show that intensive study of a small number of benchmark objects is a powerful strategy to reveal the nature of exoplanet atmospheres. Planets are complicated objects – especially tidally locked worlds with large temperature gradients from day- to nightside – and obtaining robust constraints on their chemistry and physics will require high-precision, spectroscopic observations of thermal emission and transmission. In the next sections, I discuss future plans and prospects for making these kinds of measurements.

7.2 Near Future Prospects

There are two upcoming missions that bear heavily on the future of exoplanet atmosphere characterization. The first is NASA's *TESS* mission, which is designed to search for transiting planets around the brightest stars in the sky. The predicted yield for *TESS* is roughly 1700 planets, including 130 that are smaller than $2\,R_\oplus$ transiting stars with K magnitude brighter than 9 (Sullivan et al., 2015). These detections will open the door to atmosphere characterization for Neptune and smaller planets, which has so far been limited by the number of observable targets.

The second upcoming mission is of course *JWST*, which will enable stunningly precise spectroscopy from the optical to the infrared. *JWST* has a number of major advantages over the current exoplanet atmosphere studies with *HST* and *Spitzer*. In addition to an order of magnitude improvement in sensitivity, *JWST* will also provide higher resolution spectral coverage over a much wider wavelength range (from optical to infrared). Furthermore, *JWST* has continuous coverage and a stabilized thermal environment, in contrast to *HST*'s low Earth orbit. With a single *JWST* transit or eclipse observation of a hot Jupiter, we expect to measure the carbon-to-oxygen ratio to better than 0.2 dex (Greene et al., 2016).

With the combination of *TESS* and *JWST*, it will also be possible to begin studying the atmospheres of Earth-like, potentially habitable planets. The nearest transiting, terrestrial planet in the habitable zone of a small star is predicted to be within 10 parsecs (Dressing & Charbonneau, 2015), and such a planet will be detected by *TESS*. To illustrate the potential for studying its atmosphere, Figure 7.1 shows model spectra for an Earth-size, Earth temperature planet compared to what we measured for GJ 1214b. Detecting water in the atmosphere will require an improvement in measurement precision of a factor of three, which is within reach of an intensive observing program on *JWST*.

Figure 7.1: The Road to Earth 2.0

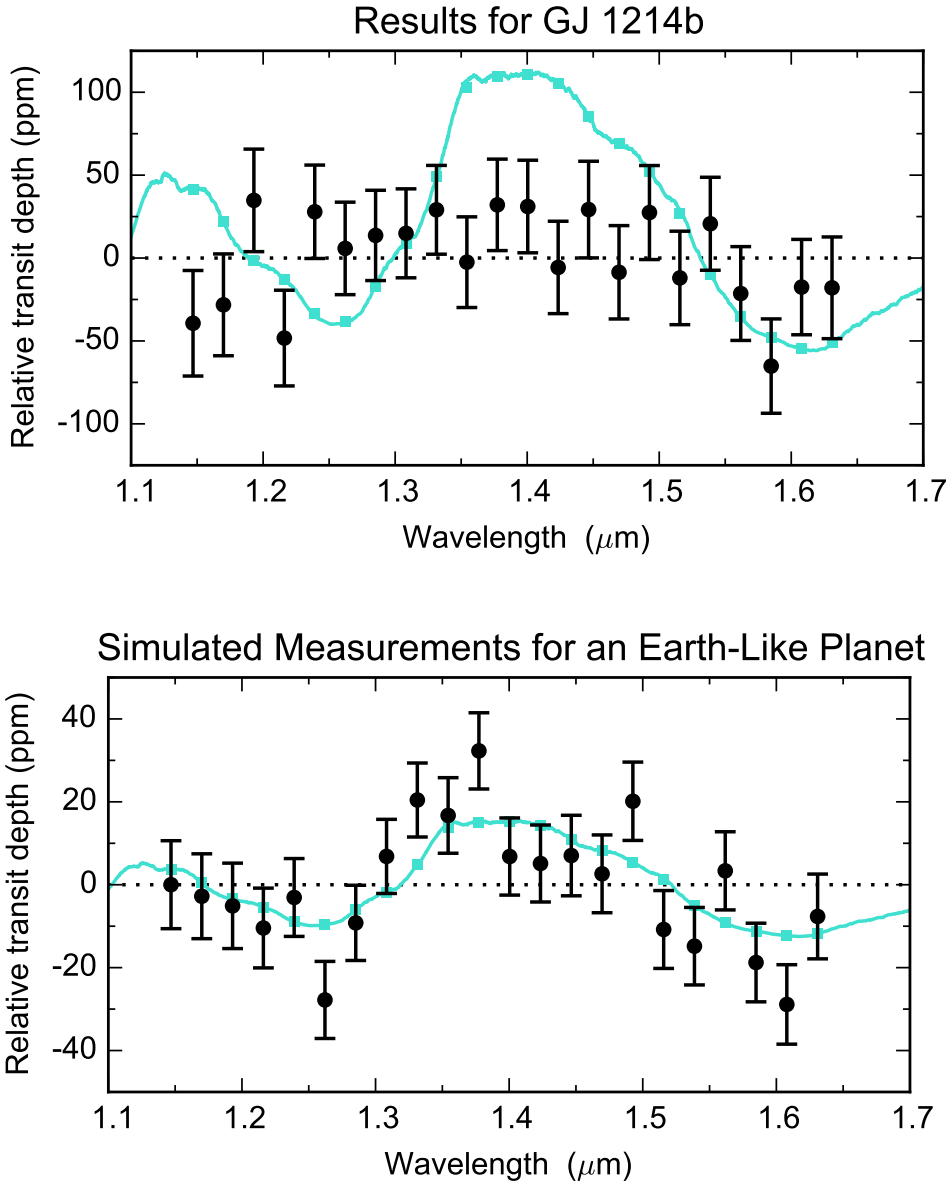

Model transmission spectra for GJ 1214b (top) and Earth 2.0 (bottom). The models assume an Earth-like atmosphere composition: nitrogen-rich with trace amounts of water. Earth 2.0 has an Earth-like temperature and surface gravity, but orbits a star the size of GJ 1214. The top panel shows the measured spectrum for GJ 1214b from (Kreidberg et al., 2014b), and the bottom panel shows a simulated spectrum with measurement precision improved by a factor of three. Such a measurement is sufficient to detect spectral features from water and will be possible with an intensive *JWST* observational campaign.

7.3 Far Future Prospects

This chapter has focused on the benefits of detailed characterization for individual objects, and *JWST* will make revolutionary measurements in this regard. However, the biggest advantage of studying exoplanets is that it gives us the chance to study a vast number of systems, and *JWST* time is too limited to fully realize this potential.

There are two missions currently being designed that will each enable the study of hundreds of planetary atmospheres. The first is a dedicated exoplanet atmosphere survey mission (either *FINESSE* or *ECHO*, Swain, 2012; Tinetti et al., 2015), designed to measure the composition and climate for planets with a wide range of sizes, orbital periods, and host star spectral type. The goal of this mission is to provide a large enough sample to carry out statistical analyses of planet formation and evolutionary histories.

The second mission is focused on Earth analogs and the search for life. Although *JWST* will make the first studies of Earth-like atmospheres, it will only be possible for a few of the best candidate planets (with the nearest and smallest host stars). Even if we detected potential biosignature gases in the atmosphere of one planet, which would be a monumental achievement, it will not necessarily constitute iron-clad evidence that the planet is inhabited. There are many potential false positive biosignatures, especially abiotic production of molecular oxygen (e.g., Tian et al., 2014; Schwieterman et al., 2016).

Our best chance of detecting life outside the Solar System is therefore to characterize the atmospheres of large number of Earth analogs, to study their properties in a range of contexts and search for patterns. This is the goal of the proposed High-Definition Space Telescope (*HDST*), a 12 m class observatory capable of directly imaging dozens of Earths (Dalcanton et al., 2015). *HDST* is designed to be a flagship mission to succeed *JWST* in the 2030s, and will serve the general astrophysics community in addition to its exoplanet mission.

Both of these missions are big steps into the unknown, and are certain to deliver many surprises, if the history of exoplanet science is any indication. What is better known, however,

is the Earth-bound challenge of making these telescopes a reality, especially one as ambitious as *HDST*. It will require great feats of engineering – directly imaging reflected light from an Earth analog requires a contrast ratio of 10^{-10}. But these missions will also require tremendous cooperation and perseverance in the astronomical community, which may be the greater challenge. Let's make it happen.

APPENDIX A

SUPPLEMENTARY INFORMATION FOR GJ 1214b RESULTS

This appendix contains supplementary information describing the observations, data reduction, systematics correction, and light curve fitting for transit observations of the super-Earth GJ 1214b.

A.1 Observations

We observed 15 transits of the super-Earth exoplanet GJ 1214b with the Wide Field Camera 3 (WFC3) instrument on the Hubble Space Telescope (HST) between UT 27 September 2012 and 20 August 2013. Each transit observation (or visit) consisted of four 96-minute HST orbits of time series spectroscopy, with 45-minute gaps in data collection in each orbit due to Earth occultation. We employed the G141 grism, which covers the wavelength range 1.1 to 1.7 μm. The spectra were binned at resolution $R \equiv \lambda/\Delta\lambda \sim 70$. To optimize the efficiency of the observations, we used spatial scan mode, which moves the spectrum perpendicular to the dispersion direction during the exposure. Spatial scanning enables longer exposures for bright targets that would otherwise saturate, such as GJ 1214. We used a 0.12"/second scan rate for all exposures, which yielded peak per pixel counts near 23,000 electrons (30% of saturation). An example raw data frame is shown in Figure A.1.

The observations had the following design. At the beginning of each orbit, we took a direct image with the F130N narrowband filter to establish a wavelength zero-point. For the remainder of each orbit, we took spatially scanned exposures with the G141 grism. Each observation used the 256 × 256 subarray. During the first five transit observations, we took 88.4 s exposures with the SPARS10, NSAMP=13 readout mode and scanned in the forward direction only. Each exposure contains NSAMP non-destructive reads. For transit observations 6 – 15, we modified our approach to reduce overhead time: we increased the exposure time to 103.1 s using the mode SPARS10, NSAMP=15, and scanned successively

Figure A.1: A Sample Raw Data Frame

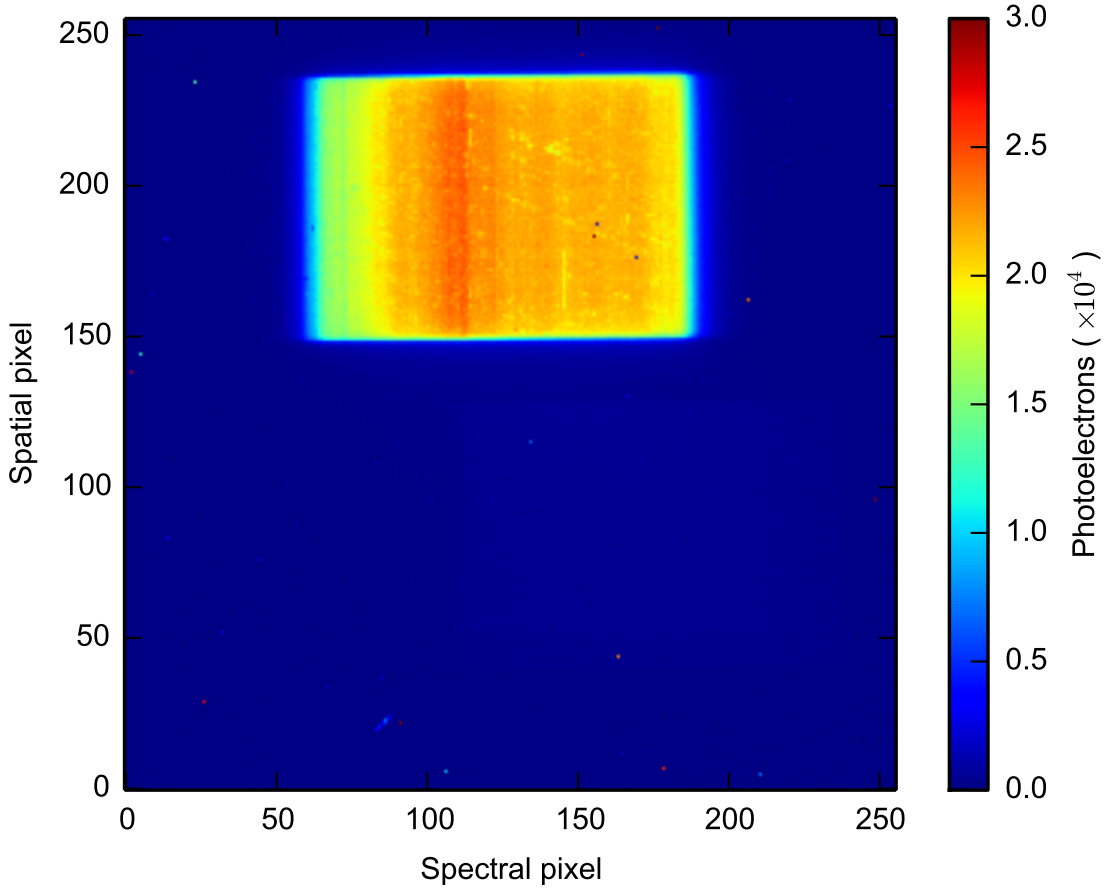

An example spatially scanned raw data frame. The exposure time was 88.4 s.

forward and backward. These approaches yielded 67 and 75 spectra per visit with duty cycles of 58% and 76%, respectively. One transit observation (UT 12 April 2013) was unsuccessful because the Fine Guidance Sensors failed to acquire the guide stars. We do not use data from this observation in our analysis. We also exclude data from the transit observations on UT 4 August 2013 and UT 12 August 2013, which showed evidence for a starspot crossing. Our final analysis therefore used 12 transit observations.

A.2 Data reduction

Our data reduction process begins with the "`ima`" data product from the WFC3 calibration pipeline, `calwf3`. These files are bias- and dark current-subtracted and flagged for bad pixels. For spatially scanned data, each pixel is illuminated by the stellar spectrum for only a small fraction of the exposure; the remainder of time it collects background. To aid in removing the background, we form subexposures of each image by subtracting consecutive non-destructive reads. A subexposure thus contains photoelectrons gathered during the 7.4 s between two reads. We reduce each subexposure independently, as follows. First we apply a wavelength-dependent flat field correction. Next we mask bad pixels that have been flagged data quality DQ = 4, 32, or 512 by `calwf3`. To estimate the background collected during the subexposure, we draw conservative masks around all stellar spectra, measure the background from the median of the unmasked pixels, and subtract it. We compute a variance for the spectrum accounting for photon shot noise, detector read noise, and uncertainty in the background estimation.

We next correct for the wavelength dependence of the spectrum on detector position. The grism dispersion varies along the spatial direction of the detector, so we calculate the dispersion solution for each row in the subexposure and interpolate the photoelectron counts in that row to the wavelength scale corresponding to the direct image position. This interpolation also corrects bad pixels. We then create a 40-pixel tall extraction box centered on the middle of the spatial scan and extract the spectrum with an optimal extraction routine. Because each row has been interpolated to a common wavelength scale, the final spectrum is constructed by summing by column the spectra from all the subexposures. The unit of time sampling in the light curve is thus a single exposure, which is the sum of 12 subexposures. See Figure A.2 for an example extracted spectrum.

Finally, we account for dispersion-direction drift of the spectra during each visit and between visits. Using the first exposure of the first visit as a template, we determine a shift in wavelength-space that minimizes the difference between each subsequent spectrum and

Figure A.2: GJ 1214b Extracted Spectrum

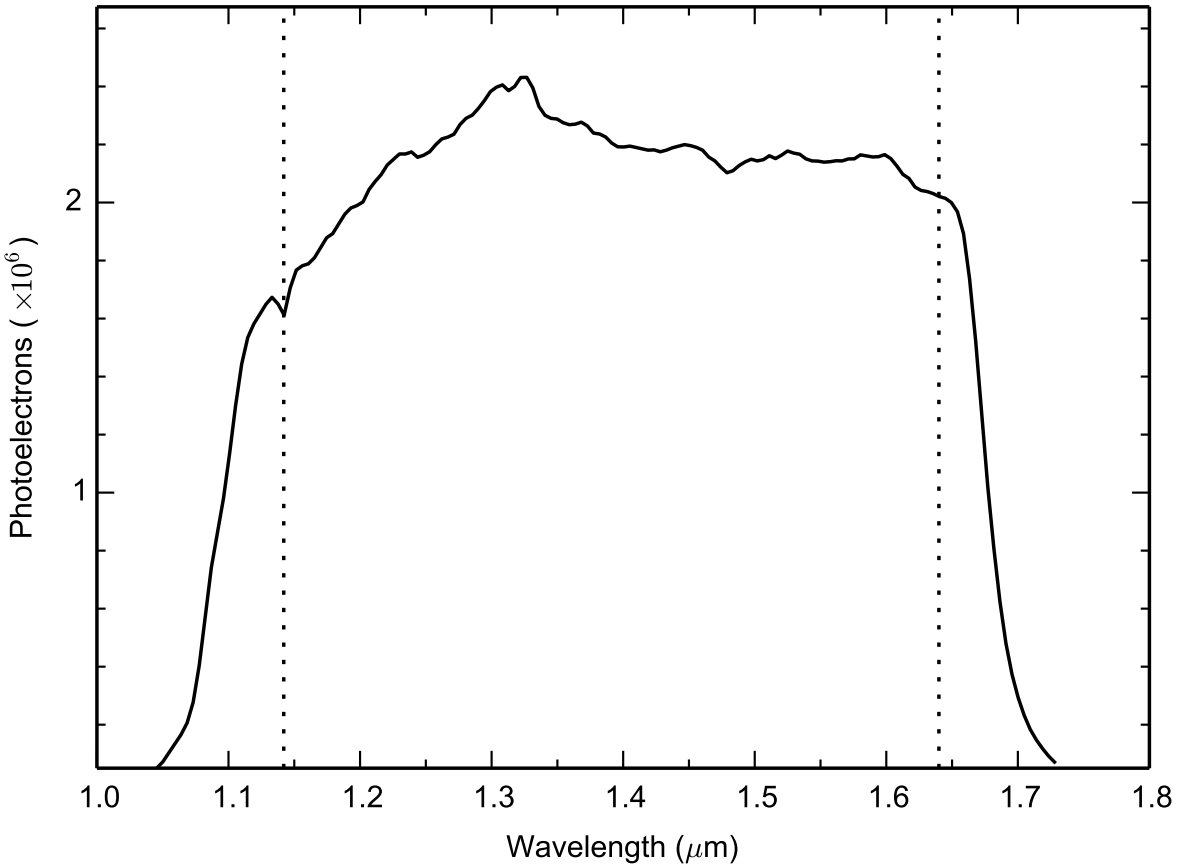

An example extracted spectrum for an 88.4 s exposure. The dotted lines indicate the wavelength range over which we measure the transmission spectrum.

the template. The best-fit shift values are less than 0.1 pixel, both within each visit and between visits. We interpolate each spectrum to an average wavelength scale, offset from the template by the mean of the estimated wavelength shifts. This step does not have a significant effect on our results. We bin the spectra in 5-pixel-wide channels, obtaining 29 spectroscopic light curves covering the wavelength range 1.05 – 1.70 μm. The data near the edges of the grism response curve exhibit more pronounced systematics, so we restrict our analysis to 22 spectroscopic channels between 1.15 and 1.63 μm. The limits are shown in Figure A.2.

A.3 Systematics correction

The light curves exhibit a ramp-like systematic similar to that seen in other WFC3 transit spectroscopy data[10,18,19]. The ramp has a larger amplitude and a different shape in the first orbit compared to subsequent orbits, so we exclude data from the first orbit in our light curve fits, following standard practice. We correct for systematics in orbits 2 – 4 using two methods:

Method 1: `model-ramp`

This method fits an analytic model to the light curve[10]. The model has the form:

$$M(\mathbf{t}) = M_{0,\lambda}(\mathbf{t})[C_{\lambda es} + V_{\lambda e}\mathbf{t_v}][1 - R_{\lambda eo}e^{-\mathbf{t_b}/\tau_\lambda}] \tag{A.1}$$

where $M_{0,\lambda}(\mathbf{t})$ is the model for the systematics-free transit light curve, $\mathbf{t}$ is a vector of observation times, $\mathbf{t_v}$ is a vector with elements $t_{v,i}$ equal to the time elapsed since the first exposure in the visit corresponding to time t_i, $\mathbf{t_b}$ is a vector with elements $t_{b,i}$ equal to the time elapsed since the first exposure in the orbit corresponding to time t_i, $C_{\lambda es}$ is a normalization, $V_{\lambda e}$ is a visit-long slope, $R_{\lambda eo}$ is a ramp amplitude, and τ_λ is a ramp timescale. The subscripts λ, e, s, and o denote whether a parameter is a function of wavelength, transit epoch, scan direction, and/or orbit number, respectively.

Method 2: `divide-white`

The second method assumes the systematics are wavelength-independent and can be modeled with a scaled time series vector of white light curve systematics, denoted $Z(\mathbf{t})$[18,20]. We fit the white light curve $W(\mathbf{t})$ with the `model-ramp` technique to determine $Z(\mathbf{t})$:

$$Z(\mathbf{t}) = W(\mathbf{t})/M_0(\mathbf{t}), \tag{A.2}$$

where $M_0(\mathbf{t})$ is the best-fit model to the white light curve. An example white light curve fit,

including the Z vector, is shown in Figure A.3.

Figure A.3: White Light Curve, Raw and Systematics-Corrected

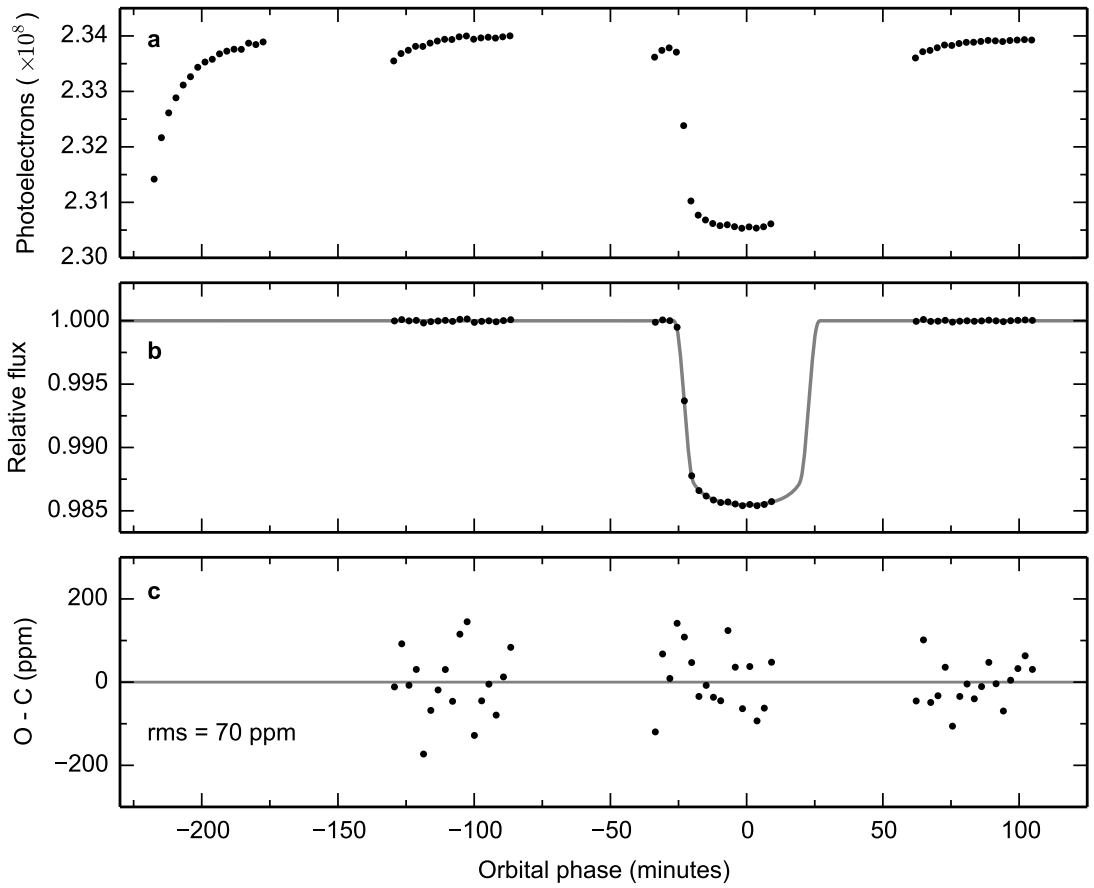

a, The broadband light curve from the first transit observation. **b**, The broadband light curve corrected for systematics using the `model-ramp` technique (points) and the best-fit model (line). **c**, Residuals from the white light curve fit. **d**, The vector of systematics Z used in the `divide-white` technique.

The spectroscopic light curves $S_\lambda(\mathbf{t})$ are modeled as

$$S_\lambda(\mathbf{t}) = C_{\lambda es} \cdot Z(\mathbf{t}) \cdot S_{0,\lambda}(\mathbf{t}) \tag{A.3}$$

where $S_{0,\lambda}(\mathbf{t})$ is the systematics-free transit light curve model for a given wavelength channel and $C_{\lambda es}$ is a normalization constant. We observe that the systematics have similar ampli-

tude and form across the wavelength range of our observations, hence the viability of the `divide-white` technique. The dominant systematics in our data are related to persistence, which depends on the peak per pixel fluence[19], but as can be seen in Figure A.2 , the product of the stellar spectrum and the G141 grism response is nearly uniform over the 1.1 – 1.7 μm range.

A.4 Light curve fits

We fit the spectroscopic light-curves with both the `divide-white` and `model-ramp` methods and determined the best-fit parameters and errors with a Markov chain Monte Carlo (MCMC) algorithm. We divided the light curves into 19 data sets (12 visits, with 2 data sets for 7 of the visits), separated by transit epoch and spatial scan direction, to account for a normalization offset between the forward-scanned and reverse-scanned light curves. We fit the data sets in each spectral channel with five 10^5 step MCMC chains, with 2.5×10^4 burn-in steps removed from each chain. We tested for convergence using the Gelman-Rubin diagnostic. The results reported are from the five chains combined.

We analyzed each spectral channel independently. The free parameters for the `divide-white` fit are a normalization constant $C_{\lambda es}$, a linear limb darkening parameter u_λ, and the planet-to-star radius ratio $R_p/R_{s,\lambda,e}$. The `model-ramp` fit had these same free parameters, plus an additional visit-long slope parameter $V_{\lambda e}$, ramp amplitudes $R_{\lambda eo}$, and a ramp timescale τ_λ. We constrained the ramp amplitudes for orbits 3 and 4 to be equal within each data set. For both methods, we held the following orbital parameters fixed at the best-fit values for the white light curve: inclination $i = 89.1°$, the ratio of the semi-major axis to the stellar radius $a/R_s = 15.23$, the orbital period $P = 1.58040464894$ days, and the time of central transit $T_c = 2454966.52488$ $\mathrm{BJD_{TDB}}$. We assume a circular orbit. There were a total of 32 and 67 free parameters per channel for the `divide-white` and `model-ramp` fits, respectively. The priors for each free parameter were uniform. We checked that the light curves are sufficiently precise to fit for all the free parameters by visually inspecting pairs

plots for the fit parameters. As an example, we show the posterior distributions of the parameters for the `divide-white` fit of the 1.40 μm channel in Figure A.4, and note that there is little correlation between parameters.

Figure A.4: Pairs Plot for Light Curve Fit Parameters

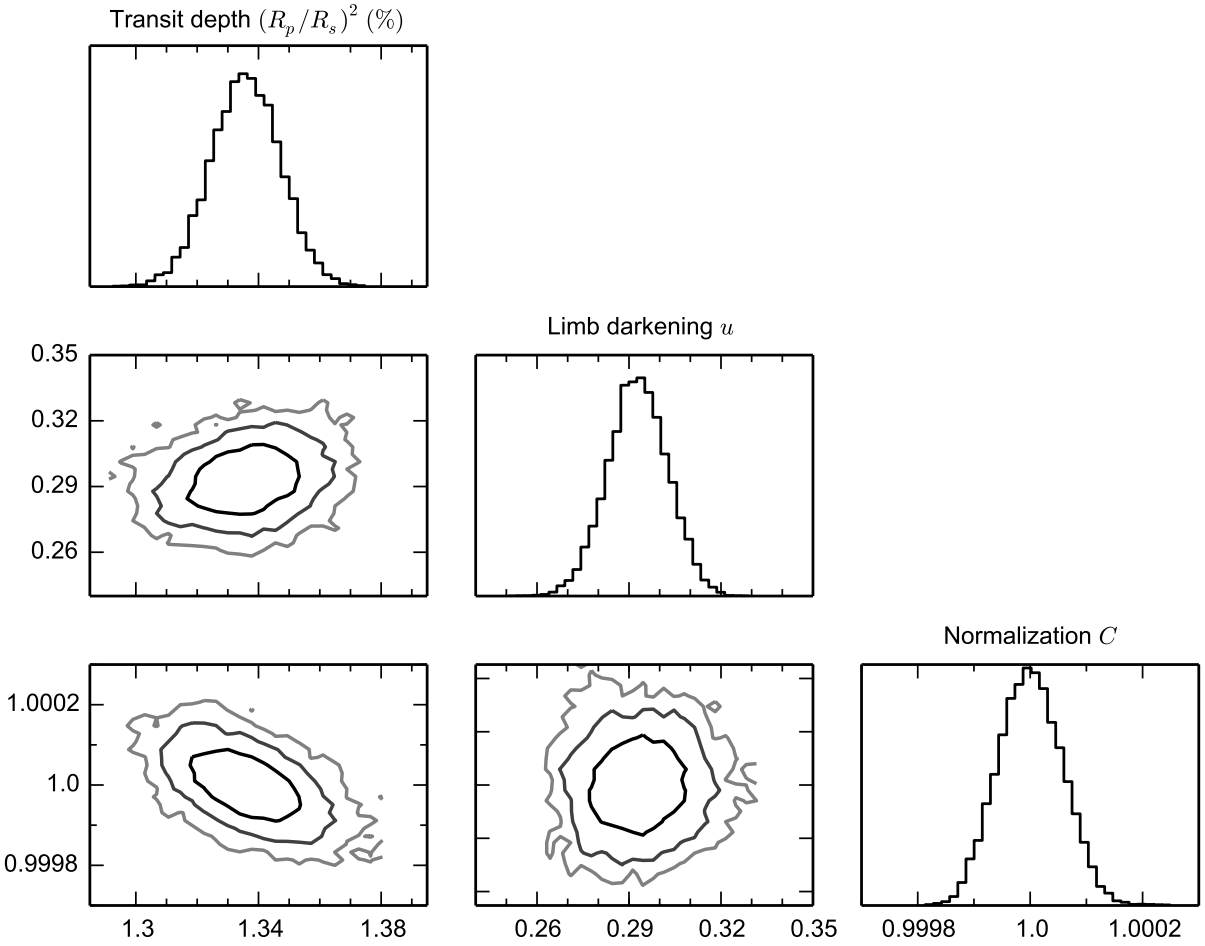

The posterior distributions for the `divide-white` fit parameters for the 1.40 μm channel from the first transit observation. The diagonal panels show histograms of the Markov chains for each parameter. The off-diagonal panels show contour plots for pairs of parameters, with lines indicating the 1, 2, and 3 σ confidence intervals for the distribution. The normalization constant is divided by its mean.

We report the measured transit depths, limb darkening parameters, and χ^2_ν values for both the `divide-white` and `model-ramp` methods in Table A.1. The transit depths given are the weighted averages over all epochs, minus the mean transit depth over all channels

Table A.1: Derived Parameters for the Light Curve Fits for the `divide-white` (`d-w`) and `model-ramp` (`m-r`) Techniques

Wavelength (μm)	Transit Depth (ppm)		Limb Darkening		χ^2_ν	
	`d-w`	`m-r`	`d-w`	`m-r`	`d-w`	`m-r`
$1.135 - 1.158$	-39 ± 31	6 ± 33	0.27 ± 0.01	0.28 ± 0.01	1.12	1.20
$1.158 - 1.181$	-28 ± 30	12 ± 32	0.26 ± 0.01	0.27 ± 0.01	1.01	1.24
$1.181 - 1.204$	34 ± 30	29 ± 30	0.25 ± 0.01	0.26 ± 0.01	1.04	1.44
$1.205 - 1.228$	-48 ± 28	-32 ± 29	0.26 ± 0.01	0.28 ± 0.01	0.90	1.22
$1.228 - 1.251$	27 ± 28	25 ± 29	0.26 ± 0.01	0.28 ± 0.01	0.85	1.29
$1.251 - 1.274$	5 ± 27	-6 ± 29	0.26 ± 0.01	0.26 ± 0.01	0.97	1.29
$1.274 - 1.297$	13 ± 27	12 ± 27	0.23 ± 0.01	0.23 ± 0.01	1.00	1.50
$1.297 - 1.320$	14 ± 26	0 ± 27	0.23 ± 0.01	0.25 ± 0.01	0.96	1.38
$1.320 - 1.343$	29 ± 26	2 ± 28	0.26 ± 0.01	0.27 ± 0.01	1.08	1.52
$1.343 - 1.366$	-2 ± 27	-15 ± 28	0.30 ± 0.01	0.32 ± 0.01	0.99	1.44
$1.366 - 1.389$	32 ± 27	35 ± 26	0.28 ± 0.01	0.29 ± 0.01	0.97	1.42
$1.389 - 1.412$	31 ± 27	33 ± 28	0.28 ± 0.01	0.29 ± 0.01	0.96	1.39
$1.412 - 1.435$	-5 ± 27	-33 ± 28	0.29 ± 0.01	0.31 ± 0.01	1.15	1.51
$1.435 - 1.458$	29 ± 29	17 ± 28	0.29 ± 0.01	0.30 ± 0.01	1.01	1.39
$1.458 - 1.481$	-8 ± 28	1 ± 29	0.32 ± 0.01	0.33 ± 0.01	1.01	1.33
$1.481 - 1.504$	27 ± 28	28 ± 28	0.28 ± 0.01	0.29 ± 0.01	0.94	1.37
$1.504 - 1.527$	-11 ± 28	-23 ± 29	0.27 ± 0.01	0.29 ± 0.01	1.15	1.58
$1.527 - 1.550$	20 ± 28	1 ± 29	0.27 ± 0.01	0.29 ± 0.01	1.17	1.56
$1.550 - 1.573$	-21 ± 28	0 ± 28	0.28 ± 0.01	0.29 ± 0.01	1.20	1.62
$1.573 - 1.596$	-65 ± 28	-62 ± 30	0.26 ± 0.01	0.28 ± 0.01	1.08	1.46
$1.596 - 1.619$	-17 ± 28	-6 ± 29	0.26 ± 0.01	0.27 ± 0.01	1.34	1.69
$1.619 - 1.642$	-17 ± 30	-26 ± 30	0.22 ± 0.01	0.24 ± 0.01	1.16	1.59

(0.013490 for `divide-white` and 0.013489 for `model-ramp`). For the results given in the main text, we use the `divide-white` spectrum because the light curve fits from this method have fewer free parameters and lower χ^2_ν values.

We performed several consistency checks as part of our analysis, enumerated below.

1. We verified that the transmission spectra obtained with the `divide-white` and `model-ramp` methods are consistent within $1\,\sigma$, and that the main conclusions of the paper are not affected by which method we chose.

2. We confirmed that the measured transit depths are consistent from epoch to epoch, as shown in Figure A.5. As a test, we fit separate transit depths to the forward- and

reverse-scanned data, and found that the transit depths are consistent for the two scan directions.

3. We tested the effects of using an inaccurate white light curve model (M_0) for the `divide-white` method and found that the results are robust to changes in M_0. For example, changing the model transit depth by $5\,\sigma$ from the best-fit white light curve value affects the relative spectroscopic transit depths by less than 1 ppm.

4. We compare our results to the previously published WFC3 transmission spectrum for GJ 1214b[10]. Our relative transit depths are within $1\,\sigma$ for 18 wavelength channels and within $2\,\sigma$ for the other four channels. The $2\,\sigma$ differences are not clustered in wavelength.

We also considered the effects of stellar activity on the transmission spectrum and found that it does not impact our results. The measured transit depths are consistent over all epochs in the white light curve and the spectroscopic light curves, which suggests that the influence of stellar activity on the spectrum is minimal. To confirm this, we simulated the effect of star spots (Désert et al., 2011) assuming they are 300 K cooler than the 3250 K stellar photosphere[22], and find that their influence is below our measurement precision. We also considered the possibility that the star spots have excess water due to their cooler temperature. This could introduce a water feature in the transmission spectrum, but it would not cancel out water features from the planet's atmosphere. Given that we do not see evidence for water absorption in the spectrum, any contribution from water in unocculted star spots must be below the level of precision in our data. As a check, we computed the transmission spectrum from three transits occurring over a timespan of just two weeks, during which time the spot coverage should be roughly constant. Even with just these three transits, we rule out a pure H_2O atmosphere at $> 5\,\sigma$ confidence, which confirms that any noise introduced by unocculted spots does not change our conclusion.

The derived limb darkening coeffients are shown in Figure A.6. We fit a single limb

Figure A.5: Transit Depths for Individual Visits

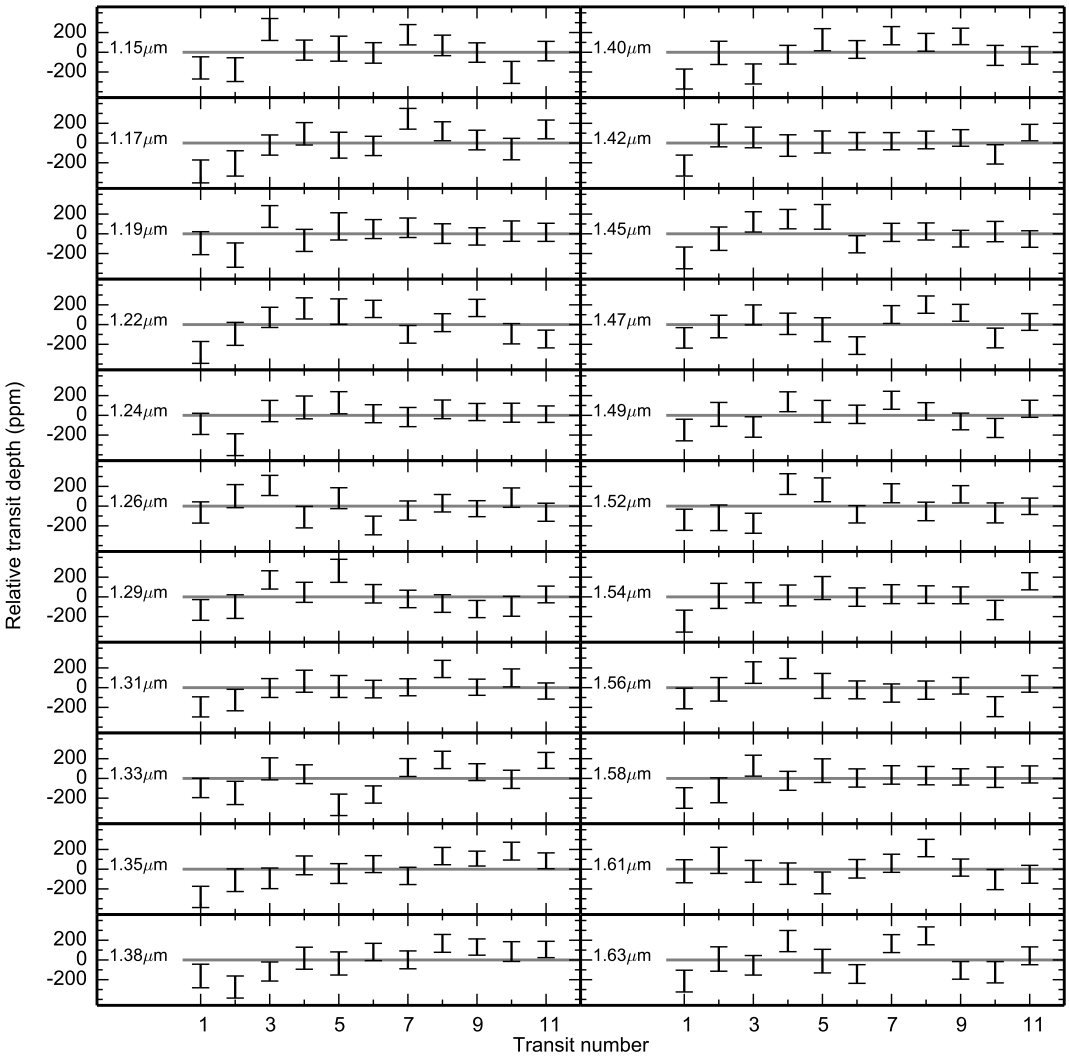

Transit depths relative to the mean in 22 spectroscopic channels, for the 12 transits analyzed. The black error bars indicate the $1\,\sigma$ uncertainties determined by MCMC.

darkening coefficient to each channel and constrained the value to be the same for all the transits. Our limb darkening fits illustrate the importance of careful treatment of limb darkening for cool stars. There is a peak in the coefficients near $1.45\,\mu$m that is due to the presence of water in the star. As a result of this, fixing the limb darkening coefficients to a

constant value in all spectral channels introduces a spurious water feature in the transmission spectrum. However, we can fit the limb darkening precisely with our data and it is non-degenerate with the transit depth. The uncertainty in our limb darkening fits introduces an uncertainty in the transit depth of less then 1 ppm. To confirm that fitting a linear limb darkening parameter is appropriate for our data, we simulated a data set using a model water vapor atmosphere, quadratic limb darkening coefficents from a 3250 K stellar model, and the residuals and systematics from the real data. We analyze this mock data set in the same way we treat the real data and find that we fully recover the water vapor transmission spectrum with a single limb darkening parameter.

Figure A.6: Fitted Limb Darkening Coefficients Compared to Models

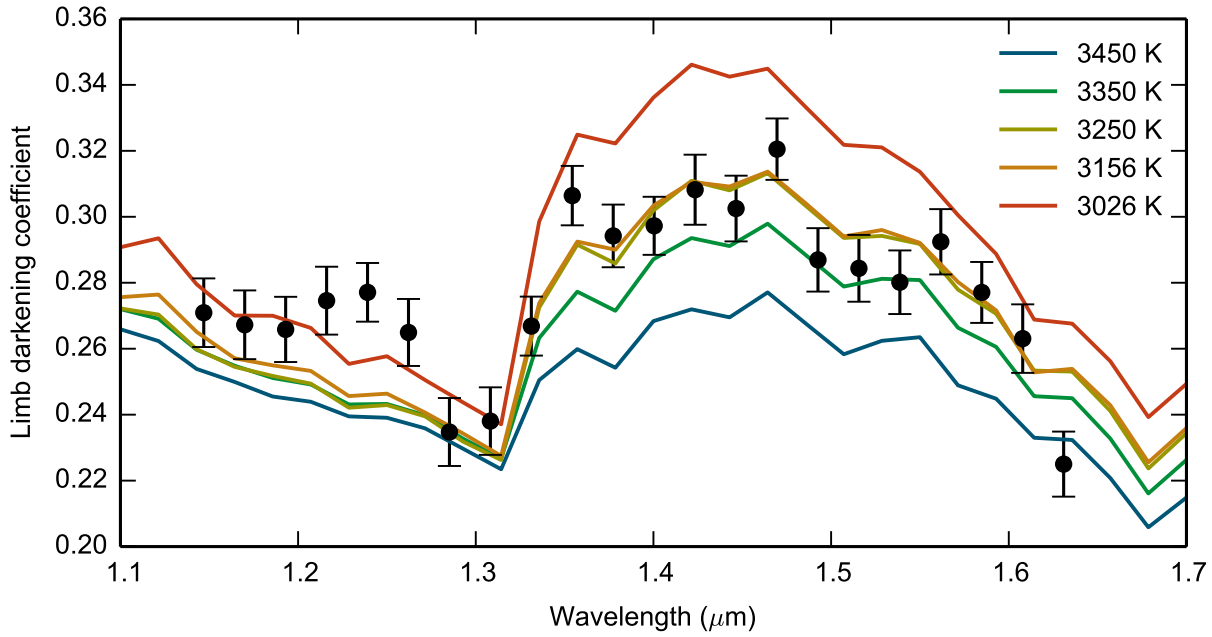

Fitted limb darkening coefficients as a function of wavelength (black points) and theoretical predictions for stellar atmospheres with a range of temperatures (lines). The uncertainties are $1\,\sigma$ confidence intervals from an MCMC. The temperature of GJ 1214 is estimated to be 3250 K (Anglada-Escudé et al., 2013).

REFERENCES

Abubekerov, M. K., & Gostev, N. Y. 2013, MNRAS, 432, 2216

Adams, E. R., Seager, S., & Elkins-Tanton, L. 2008, Astrophys. J., 673, 1160

Ali-Dib, M., Mousis, O., Petit, J.-M., & Lunine, J. I. 2014, ApJ, 785, 125

Anglada-Escudé, G., Rojas-Ayala, B., Boss, A. P., Weinberger, A. J., & Lloyd, J. P. 2013, Astron. Astrophys., 551, A48

Asplund, M., Grevesse, N., Sauval, A. J., & Scott, P. 2009, ARAA, 47, 481

Atreya, S. K., Mahaffy, P. R., Niemann, H. B., Wong, M. H., & Owen, T. C. 2003, Planet. Space Sci., 51, 105

Atreya, S. K., Wong, M. H., Owen, T. C., et al. 1999, Planet. Space Sci., 47, 1243

Bakos, G. Á., Noyes, R. W., Kovács, G., et al. 2007, ApJ, 656, 552

Barstow, J. K., Aigrain, S., Irwin, P. G. J., Fletcher, L. N., & Lee, J.-M. 2013, MNRAS, 434, 2616

Barstow, J. K., Aigrain, S., Irwin, P. G. J., et al. 2014, ApJ, 786, 154

Batygin, K., Bodenheimer, P. H., & Laughlin, G. P. 2015, ArXiv e-prints, arXiv:1511.09157

Batygin, K., Stanley, S., & Stevenson, D. J. 2013, ApJ, 776, 53

Bean, J. L., Miller-Ricci Kempton, E., & Homeier, D. 2010, Nature, 468, 669

Bean, J. L., Désert, J.-M., Kabath, P., et al. 2011, Astrophys. J. , 743, 92

Bechter, E. B., Crepp, J. R., Ngo, H., et al. 2014, ApJ, 788, 2

Benneke, B., & Seager, S. 2012, Astrophys. J., 753, 100

—. 2013, ArXiv e-prints, arXiv:1306.6325

Bergfors, C., Brandner, W., Daemgen, S., et al. 2013, MNRAS, 428, 182

Berta, Z. K., Charbonneau, D., Bean, J., et al. 2011, ApJ, 736, 12

Berta, Z. K., Charbonneau, D., Désert, J.-M., et al. 2012, ApJ, 747, 35

Birkby, J. L., de Kok, R. J., Brogi, M., et al. 2013, Mon. Not. R. Astron. Soc., 436, L35

Blecic, J., Harrington, J., Madhusudhan, N., et al. 2014, Astrophys. J., 781, 116

Borucki, W. J., Koch, D., Basri, G., et al. 2010, Science, 327, 977

Borucki, W. J., Koch, D. G., Basri, G., et al. 2011, ApJ, 736, 19

Brogi, M., de Kok, R. J., Birkby, J. L., Schwarz, H., & Snellen, I. A. G. 2014, A&A, 565, A124

Bulirsch, R. 1965, Numerische Mathematik, 7, 353

Burrows, A., & Sharp, C. M. 1999, ApJ, 512, 843

Burrows, A. S. 2014, Proceedings of the National Academy of Science, 111, 12601

Burton, J. R., Watson, C. A., Rodríguez-Gil, P., et al. 2015, MNRAS, 446, 1071

Campo, C. J., Harrington, J., Hardy, R. A., et al. 2011, ApJ, 727, 125

Carter, J. A., & Winn, J. N. 2009, ApJ, 704, 51

Cassan, A., Kubas, D., Beaulieu, J.-P., et al. 2012, Nature, 481, 167

Castelli, F., & Kurucz, R. L. 2004, ArXiv Astrophysics e-prints, astro-ph/0405087

Charbonneau, D., Brown, T. M., Noyes, R. W., & Gilliland, R. L. 2002, ApJ, 568, 377

Charbonneau, D., Berta, Z. K., Irwin, J., et al. 2009, Nature, 462, 891

Chatterjee, S., & Tan, J. C. 2014, ApJ, 780, 53

Chiang, E., & Laughlin, G. 2013, MNRAS, 431, 3444

Claret, A. 2000, A&A, 363, 1081

Claret, A., & Hauschildt, P. H. 2003, A&A, 412, 241

Colavecchia, F. D., & Gasaneo, G. 2004, Computer Physics Communications, 157, 32

Copperwheat, C. M., Wheatley, P. J., Southworth, J., et al. 2013, MNRAS, 434, 661

Cornish, N. J., & Littenberg, T. B. 2007, Phys. Rev. D, 76, 083006

Cowan, N. B., & Agol, E. 2008, ApJL, 678, L129

Cowan, N. B., Agol, E., & Charbonneau, D. 2007, MNRAS, 379, 641

Cowan, N. B., Machalek, P., Croll, B., et al. 2012, ApJ, 747, 82

Croll, B., Lafreniere, D., Albert, L., et al. 2011, AJ, 141, 30

Croll, B., Albert, L., Jayawardhana, R., et al. 2015, ApJ, 802, 28

Crossfield, I. J. M., Barman, T., Hansen, B. M. S., Tanaka, I., & Kodama, T. 2012, ApJ, 760, 140

Dalcanton, J., Seager, S., Aigrain, S., et al. 2015, ArXiv e-prints, arXiv:1507.04779

Dawson, R. I. 2014, ApJL, 790, L31

Dawson, R. I., Lee, E. J., & Chiang, E. 2016, ApJ, 822, 54

Deming, D., Wilkins, A., McCullough, P., et al. 2013, ApJ, 774, 95

Désert, J.-M., Sing, D., Vidal-Madjar, A., et al. 2011, A&A, 526, A12

Diamond-Lowe, H., Stevenson, K. B., Bean, J. L., Line, M. R., & Fortney, J. J. 2014, ApJ, 796, 66

Diaz-Cordoves, J., & Gimenez, A. 1992, A&A, 259, 227

Dodson-Robinson, S. E., Willacy, K., Bodenheimer, P., Turner, N. J., & Beichman, C. A. 2009, Icarus, 200, 672

Dong, S., & Zhu, Z. 2013, ApJ, 778, 53

Doyle, L. R., Carter, J. A., Fabrycky, D. C., et al. 2011, Science, 333, 1602

Dressing, C. D., & Charbonneau, D. 2013, ApJ, 767, 95

—. 2015, ApJ, 807, 45

Dressing, C. D., Charbonneau, D., Dumusque, X., et al. 2015, ApJ, 800, 135

Eastman, J., Gaudi, B. S., & Agol, E. 2013, PASP, 125, 83

Fletcher, L. N., Orton, G. S., Teanby, N. A., Irwin, P. G. J., & Bjoraker, G. L. 2009, Icarus, 199, 351

Föhring, D., Dhillon, V. S., Madhusudhan, N., et al. 2013, MNRAS, 435, 2268

Foreman-Mackey, D., Hogg, D. W., Lang, D., & Goodman, J. 2013, PASP, 125, 306

Foreman-Mackey, D., Hogg, D. W., & Morton, T. D. 2014, ApJ, 795, 64

Fortney, J. J. 2005, Mon. Not. R. Astron. Soc., 364, 649

Fortney, J. J., Cooper, C. S., Showman, A. P., Marley, M. S., & Freedman, R. S. 2006, ApJ, 652, 746

Fortney, J. J., Lodders, K., Marley, M. S., & Freedman, R. S. 2008, ApJ, 678, 1419

Fortney, J. J., Mordasini, C., Nettelmann, N., et al. 2013, ApJ, 775, 80

Fortney, J. J., Shabram, M., Showman, A. P., et al. 2010, ApJ, 709, 1396

Fossati, L., Haswell, C. A., Froning, C. S., et al. 2010, ApJL, 714, L222

Fraine, J., Deming, D., Benneke, B., et al. 2014, Nature, 513, 526

Fraine, J. D., Deming, D., Gillon, M., et al. 2013, Astrophys. J. , 765, 127

Fressin, F., Torres, G., Charbonneau, D., et al. 2013, ApJ, 766, 81

Gautier, D., Hersant, F., Mousis, O., & Lunine, J. I. 2001, ApJL, 550, L227

Gazak, J. Z., Johnson, J. A., Tonry, J., et al. 2012, Advances in Astronomy, 2012, 30

Gibson, N. P., Pont, F., & Aigrain, S. 2011, MNRAS, 411, 2199

Gillon, M., Triaud, A. H. M. J., Fortney, J. J., et al. 2012, Astron. & Astrophys., 542, A4

Gillon, M., Anderson, D. R., Collier-Cameron, A., et al. 2014, A&A, 562, L3

Gillon, M., Jehin, E., Lederer, S. M., et al. 2016, Nature, 533, 221

Giménez, A. 2006, A&A, 450, 1231

Greene, T. P., Line, M. R., Montero, C., et al. 2016, ApJ, 817, 17

Grillmair, C. J., Burrows, A., Charbonneau, D., et al. 2008, Nature, 456, 767

Guillot, T. 2010, A&A, 520, A27

Guillot, T., & Gautier, D. 2014, ArXiv e-prints, arXiv:1405.3752

Han, E., Wang, S. X., Wright, J. T., et al. 2014, PASP, 126, 827

Hansen, B. M. S., & Murray, N. 2013, ApJ, 775, 53

Harrington, J., Hansen, B. M., Luszcz, S. H., et al. 2006, Science, 314, 623

Haswell, C. A., Fossati, L., Ayres, T., et al. 2012, ApJ, 760, 79

Hauschildt, P. H., Allard, F., & Baron, E. 1999, ApJ, 512, 377

Hebb, L., Collier-Cameron, A., Loeillet, B., et al. 2009, ApJ, 693, 1920

Helled, R., & Lunine, J. 2014, ArXiv e-prints, arXiv:1403.2891

Heng, K., Hayek, W., Pont, F., & Sing, D. K. 2012, MNRAS, 420, 20

Hersant, F., Gautier, D., & Lunine, J. I. 2004, Planet. Space Sci., 52, 623

Howard, A. W., Marcy, G. W., Bryson, S. T., et al. 2012, ApJS, 201, 15

Howard, A. W., Sanchis-Ojeda, R., Marcy, G. W., et al. 2013, Nature, 503, 381

Howe, A. R., & Burrows, A. S. 2012, Astrophys. J., 756, 176

Irwin, P. G. J., Teanby, N. A., de Kok, R., et al. 2008, J. Quant. Spec. Radiat. Transf., 109, 1136

Jeffreys, H. 1998, The Theory of Probability (OUP Oxford)

Johnson, T. V., Mousis, O., Lunine, J. I., & Madhusudhan, N. 2012, ApJ, 757, 192

Karkoschka, E., & Tomasko, M. G. 2011, Icarus, 211, 780

Kass, R. E., & Raftery, A. E. 1995, Journal of the american statistical association, 90, 773

Kataria, T., Showman, A. P., Fortney, J. J., Marley, M. S., & Freedman, R. S. 2014a, ApJ, 785, 92

Kataria, T., Showman, A. P., Fortney, J. J., et al. 2014b, ArXiv e-prints, arXiv:1410.2382

Kipping, D. M. 2011, MNRAS, 416, 689

Kjurkchieva, D., Dimitrov, D., Vladev, A., & Yotov, V. 2013, MNRAS, 431, 3654

Klinglesmith, D. A., & Sobieski, S. 1970, AJ, 75, 175

Knutson, H. A., Benneke, B., Deming, D., & Homeier, D. 2014a, Nature, 505, 66

Knutson, H. A., Charbonneau, D., Deming, D., & Richardson, L. J. 2007a, Pub. Astron. Soc. Pacific, 119, 616

Knutson, H. A., Charbonneau, D., Allen, L. E., et al. 2007b, Nature, 447, 183

Knutson, H. A., Dragomir, D., Kreidberg, L., et al. 2014b, ArXiv e-prints, arXiv:1403.4602

—. 2014c, ApJ, 794, 155

Komacek, T. D., & Showman, A. P. 2016, ApJ, 821, 16

Konopacky, Q. M., Barman, T. S., Macintosh, B. A., & Marois, C. 2013, Science, 339, 1398

Kopal, Z. 1950, Harvard College Observatory Circular, 454, 1

Kopparapu, R. K. 2013, ApJL, 767, L8

Kopparapu, R. k., Kasting, J. F., & Zahnle, K. J. 2012, ApJ, 745, 77

Kreidberg, L. 2015, PASP, 127, 1161

Kreidberg, L., Bean, J. L., Désert, J.-M., et al. 2014a, ApJL, 793, L27

—. 2014b, Nature, 505, 69

Kreidberg, L., Line, M. R., Bean, J. L., et al. 2015, ApJ, 814, 66

Lecavelier Des Etangs, A., Pont, F., Vidal-Madjar, A., & Sing, D. 2008, A&A, 481, L83

Lee, E. J., & Chiang, E. 2016, ApJ, 817, 90

Lee, J.-M., Heng, K., & Irwin, P. G. J. 2013, ApJ, 778, 97

Line, M. R., Knutson, H., Deming, D., Wilkins, A., & Desert, J.-M. 2013a, ApJ, 778, 183

Line, M. R., Knutson, H., Wolf, A. S., & Yung, Y. L. 2014, Astrophys. J., 783, 70

Line, M. R., Vasisht, G., Chen, P., Angerhausen, D., & Yung, Y. L. 2011, ApJ, 738, 32

Line, M. R., & Yung, Y. L. 2013a, Astrophys. J., 779, 3

—. 2013b, ApJ, 779, 3

Line, M. R., Wolf, A. S., Zhang, X., et al. 2013b, ApJ, 775, 137

Lodders, K. 2004, ApJ, 611, 587

López-Morales, M., Coughlin, J. L., Sing, D. K., et al. 2010, ApJL, 716, L36

Macintosh, B., Graham, J. R., Barman, T., et al. 2015, Science, 350, 64

Madhusudhan, N. 2012, ApJ, 758, 36

Madhusudhan, N., Amin, M. A., & Kennedy, G. M. 2014a, ApJL, 794, L12

Madhusudhan, N., Crouzet, N., McCullough, P. R., Deming, D., & Hedges, C. 2014b, ArXiv e-prints, arXiv:1407.6054

—. 2014c, ApJL, 791, L9

Madhusudhan, N., Mousis, O., Johnson, T. V., & Lunine, J. I. 2011a, ApJ, 743, 191

—. 2011b, ApJ, 743, 191

Madhusudhan, N., & Seager, S. 2009, ApJ, 707, 24

Madhusudhan, N., Harrington, J., Stevenson, K. B., et al. 2011c, Nature, 469, 64

Mandel, K., & Agol, E. 2002, ApJL, 580, L171

Mandell, A. M., Haynes, K., Sinukoff, E., et al. 2013, ApJ, 779, 128

Marboeuf, U., Mousis, O., Ehrenreich, D., et al. 2008, ApJ, 681, 1624

Marboeuf, U., Thiabaud, A., Alibert, Y., Cabral, N., & Benz, W. 2014, ArXiv e-prints, arXiv:1407.7282

Matousek, S. 2007, Acta Astronautica, 61, 932

Mayor, M., & Queloz, D. 1995, Nature, 378, 355

McBride, B. J., & Gordon, S. 1996, Computer Program for Calculation of Complex Chemical Equilibrium Compositions and Applications II. User's Manual and Program Description, Tech. rep., NASA

McCullough, P., & MacKenty, J. 2012, Considerations for using Spatial Scans with WFC3, Tech. rep.

McCullough, P. R., Crouzet, N., Deming, D., & Madhusudhan, N. 2014, ApJ, 791, 55

Miller-Ricci, E., & Fortney, J. J. 2010, Astrophys. J., 716, L74

Miller-Ricci, E., Seager, S., & Sasselov, D. 2009a, Astrophys. J., 690, 1056

—. 2009b, Astrophys. J., 690, 1056

Miller-Ricci Kempton, E., Zahnle, K., & Fortney, J. J. 2012, Astrophys. J., 745, 3

Morley, C. V., Fortney, J. J., Kempton, E. M.-R., et al. 2013, Astrophys. J., 775, 33

Morley, C. V., Fortney, J. J., Marley, M. S., et al. 2015, ApJ, 815, 110

Morton, T. D., & Swift, J. 2014, ApJ, 791, 10

Moses, J. I., Madhusudhan, N., Visscher, C., & Freedman, R. S. 2013, ApJ, 763, 25

Moses, J. I., Visscher, C., Fortney, J. J., et al. 2011, ApJ, 737, 15

Mousis, O., Lunine, J. I., Madhusudhan, N., & Johnson, T. V. 2012, Astrophys. J., 751, L7

Mousis, O., Lunine, J. I., Tinetti, G., et al. 2009, A&A, 507, 1671

Nettelmann, N., Fortney, J. J., Kramm, U., & Redmer, R. 2011, Astrophys. J., 733, 2

Ngo, H., Knutson, H. A., Hinkley, S., et al. 2015, ApJ, 800, 138

Nichols, J. D., Wynn, G. A., Goad, M., et al. 2015, ArXiv e-prints, arXiv:1502.07489

Öberg, K. I., Murray-Clay, R., & Bergin, E. A. 2011, ApJL, 743, L16

Owen, T., Mahaffy, P., Niemann, H. B., et al. 1999, Nature, 402, 269

Pál, A. 2012, MNRAS, 420, 1630

Parmentier, V., & Guillot, T. 2014, Astron. & Astrophys., 562, A133

Parviainen, H. 2015, MNRAS, 450, 3233

Pepe, F., Cameron, A. C., Latham, D. W., et al. 2013, Nature, 503, 377

Pepper, J., Pogge, R. W., DePoy, D. L., et al. 2007, PASP, 119, 923

Petigura, E. A., Howard, A. W., & Marcy, G. W. 2013, Proceedings of the National Academy of Science, 110, 19273

Pierrehumbert, R. T. 2010, Principles of Planetary Climate

Pollacco, D. L., Skillen, I., Collier Cameron, A., et al. 2006, PASP, 118, 1407

Pollack, J. B., Hubickyj, O., Bodenheimer, P., et al. 1996, Icarus, 124, 62

Pont, F., Knutson, H., Gilliland, R. L., Moutou, C., & Charbonneau, D. 2008, Mon. Not. R. Astron. Soc., 385, 109

Press, W. H., Teukolsky, S. A., Vetterling, W. T., & Flannery, B. P. 1992, Numerical recipes in FORTRAN. The art of scientific computing

Robinson, T. D., & Catling, D. C. 2012, ApJ, 757, 104

Rogers, L. A., & Seager, S. 2010a, Astrophys. J. , 712, 974

—. 2010b, Astrophys. J. , 716, 1208

Rowe, J. F., Coughlin, J. L., Antoci, V., et al. 2015, ApJS, 217, 16

Sanchis-Ojeda, R., Rappaport, S., Winn, J. N., et al. 2014, ApJ, 787, 47

Santos, N. C., Bouchy, F., Mayor, M., et al. 2004, A&A, 426, L19

Schlichting, H. E. 2014, ApJL, 795, L15

Schwarzschild, K., & Villiger, W. 1906, ApJ, 23, 284

Schwieterman, E. W., Meadows, V. S., Domagal-Goldman, S. D., et al. 2016, ApJL, 819, L13

Seager, S. 2010, Exoplanets

Seager, S., & Sasselov, D. D. 2000, ApJ, 537, 916

Sellke, T., Bayarri, M. J., & Berger, J. O. 2001, The American Statistician, 55, pp. 62

Sharp, C. M., & Burrows, A. 2007, ApJS, 168, 140

Showman, A. P., Fortney, J. J., Lian, Y., et al. 2009, ApJ, 699, 564

Showman, A. P., & Ingersoll, A. P. 1998, Icarus, 132, 205

Sing, D. K., Pont, F., Aigrain, S., et al. 2011, MNRAS, 416, 1443

Sing, D. K., Lecavelier des Etangs, A., Fortney, J. J., et al. 2013, MNRAS, 436, 2956

Sing, D. K., Fortney, J. J., Nikolov, N., et al. 2016, Nature, 529, 59

Southworth, J., Maxted, P. F. L., & Smalley, B. 2004, MNRAS, 351, 1277

Southworth, J., Mancini, L., Ciceri, S., et al. 2015, MNRAS, 447, 711

Sromovsky, L. A., Fry, P. M., & Kim, J. H. 2011, Icarus, 215, 292

Stevenson, K. B., Bean, J. L., Fabrycky, D., & Kreidberg, L. 2014a, ApJ, 796, 32

Stevenson, K. B., Bean, J. L., Madhusudhan, N., & Harrington, J. 2014b, ArXiv e-prints, arXiv:1406.7567

Stevenson, K. B., Bean, J. L., Seifahrt, A., et al. 2013, ArXiv e-prints, arXiv:1305.1670

—. 2014c, AJ, 147, 161

Stevenson, K. B., Harrington, J., Fortney, J. J., et al. 2012, ApJ, 754, 136

Stevenson, K. B., Désert, J.-M., Line, M. R., et al. 2014d, Science, 346, 838

Sullivan, P. W., Winn, J. N., Berta-Thompson, Z. K., et al. 2015, ApJ, 809, 77

Swain, M., Deroo, P., Tinetti, G., et al. 2013, Icarus, 225, 432

Swain, M. R. 2012, in American Astronomical Society Meeting Abstracts, Vol. 220, American Astronomical Society Meeting Abstracts #220, 505.05

Swain, M. R., Line, M. R., & Deroo, P. 2014, ApJ, 784, 133

Swain, M. R., Vasisht, G., Tinetti, G., et al. 2009, ApJL, 690, L114

Teske, J. K., Cunha, K., Smith, V. V., Schuler, S. C., & Griffith, C. A. 2014, ApJ, 788, 39

Teske, J. K., Schuler, S. C., Cunha, K., Smith, V. V., & Griffith, C. A. 2013, ApJL, 768, L12

Tian, F., France, K., Linsky, J. L., Mauas, P. J. D., & Vieytes, M. C. 2014, Earth and Planetary Science Letters, 385, 22

Tinetti, G., Drossart, P., Eccleston, P., et al. 2015, Experimental Astronomy, 40, 329

Traub, W. A. 2012, ApJ, 745, 20

Trotta, R. 2008, Contemporary Physics, 49, 71

Vanderburg, A., Johnson, J. A., Rappaport, S., et al. 2015, Nature, 526, 546

Venot, O., Hébrard, E., Agúndez, M., Decin, L., & Bounaceur, R. 2015, ArXiv e-prints, arXiv:1502.03567

Wakeford, H. R., Sing, D. K., Evans, T., Deming, D., & Mandell, A. 2016, ApJ, 819, 10

Weinberg, M. D. 2012, Bayesian Anal., 7, 737

Wilkins, A. N., Deming, D., Madhusudhan, N., et al. 2014, ApJ, 783, 113

Wöllert, M., & Brandner, W. 2015, A&A, 579, A129

Wong, M. H., Mahaffy, P. R., Atreya, S. K., Niemann, H. B., & Owen, T. C. 2004, Icarus, 171, 153

Youdin, A. N. 2011, ApJ, 742, 38

Zhao, M., Monnier, J. D., Swain, M. R., Barman, T., & Hinkley, S. 2012, ApJ, 744, 122